Interfacing an ion funnel into laser ablation time of flight mass spectrometry

Lorenzo Querci

LORENZO QUERCI

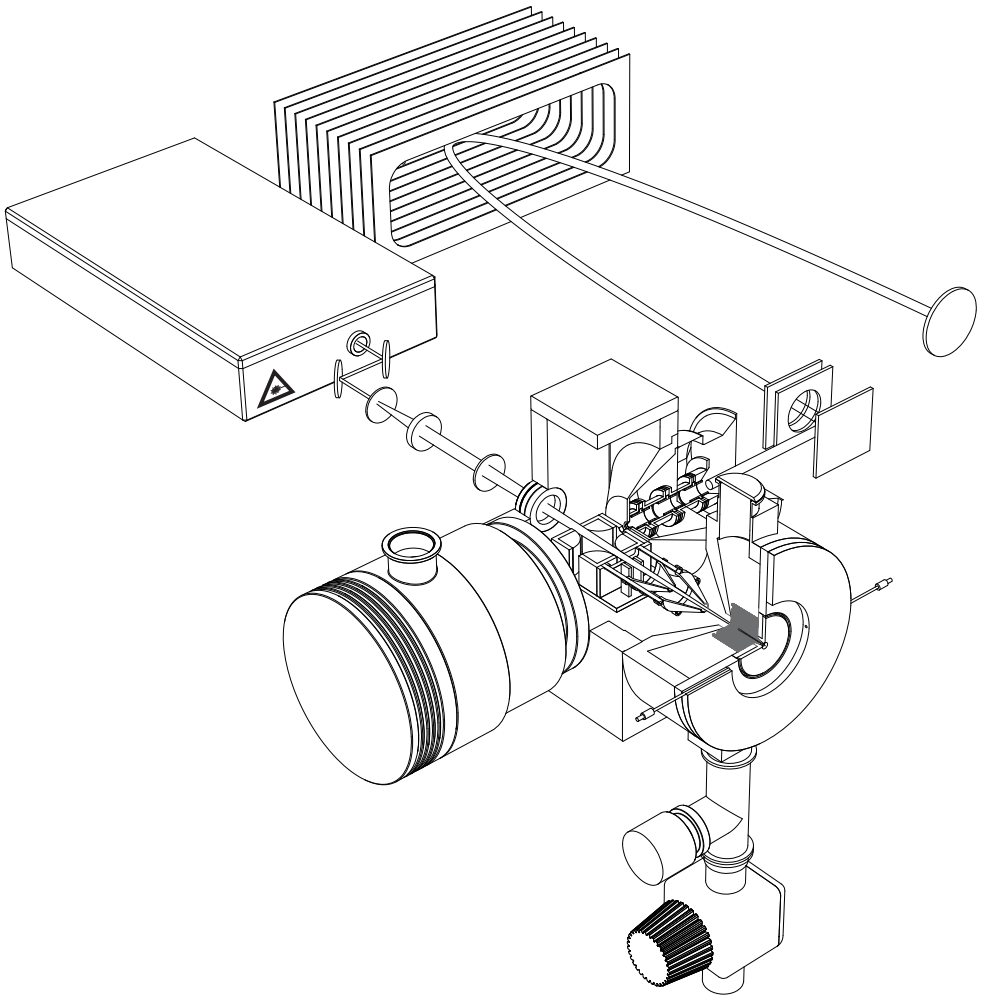# INTERFACING AN ION FUNNEL INTO LASER ABLATION TIME OF FLIGHT MASS SPECTROMETRY

INTERFACING AN ION FUNNEL INTO LASER ABLATION TIME OF FLIGHT MASS SPECTROMETRY

A dissertation submitted to attain the degree of

DOCTOR OF SCIENCES of ETH ZURICH

(Dr. sc. ETH Zurich)

presented by

LORENZO QUERCI

MSc. Chemistry ETH Zurich

born on 27 November 1989
citizen of Switzerland and Italy

accepted on the recommendation of

Prof. Dr. Detlef Günther, examiner
Prof. Dr. Hans-Arno Synal, co-examiner
Dr. Bodo Hattendorf, co-examiner

2019

"Nam has quidem gallina scripsit"

plauto *Pseudolo*

ABSTRACT

In the present work the development and characterization of a novel laser ablation ion source for element mass spectrometry is presented. The concept of Laser Ablation Mass Spectrometry (LAMS) was introduced in the 60s by Honig and Woolston. The at that time presented method showed a strong matrix dependence of the ion yields which made the use of LAMS for quantitative analyses challenging. A major reason for this can be attributed to the nanosecond (ns) lasers pulses used for ablation in high vacuum. In this work, a novel strategy is presented, using laser ablation at elevated pressure in combination with differential pumping via a convergent divergent (CD) nozzle and an RF only ion funnel to transfer the ions to the mass spectrometer. The CD- nozzle and RF only ion funnel achieve an efficient collisional cooling of laser generated ions and their separation from the buffer gas. This configuration ensures a sufficient pressure difference between ion source (up to 100 mbar) and the mass spectrometer (10^{-6} mbar) while allowing for multiple collisions. In the first stage of the project a 3 ns, frequency doubled Nd:YAG ($\lambda = 532$ nm) laser was employed to evaluate the influence of buffer gas pressure and transmission properties of the ion funnel. It was shown for the first time that use of the CD nozzle-ion funnel combination can improve the ion detection compared to the ablation in high vacuum. Ion signals were increased by up to a factor of 200 and the effective cooling of the ions resulted in longer transient profiles of ions generated from a single laser pulse. The ion signals were found to increase for all detected species when the pressure in the ablation region was elevated. This was mostly attributed to the initial compression of the ion cloud within the ablation chamber. The ions' arrival times at the TOFMS were found to be strongly influenced by the gas dynamics in the setup. The operating condition of the ion funnel were investigated with respect to the ion transmission and its mass dependence. The RF amplitude and frequencies for optimal ion transmission were generally in accordance to the predictions for an ion funnel configuration: Lower amplitude or higher frequency yielded better ion transmission for lower mass to charge ratios (m/Q) and vice versa. Space charge effects were observed, in particular when a high amount of the heavy isotopes (Pb and Bi) was present. Brass samples were investigated and it was observed that relative sensitivity coefficients of different elements differed substantially from unity. Values of

several thousands for Pb and Bi were obtained, making quantitative analyses a challenge. It was then studied how much femtosecond laser ablation would improve the quantification capabilities of the source. A 150 femtosecond (fs), frequency doubled Ti:Sapphire (λ= 400 nm) laser was used for the analysis of metals and glass. Employing the fs laser, the sample distance relative to the nozzle was increased and the effective pressure in the ablation chamber was lowered for optimal ion detection. A broader range of m/Q transmission was found when an RF Frequency of 5 MHz and 20 V_{pp} were used with a new RF amplifier. The investigation of a brass sample revealed that the mean mass discrimination was relatively uniform across the m/Q range with sub-% difference in isotope transmission per m/Q. The repeatability of the isotope ratio measurements was about 1% for experiments using 2000 laser pulses per analysis. The brass sample was quantitatively analyzed by fs-LAMS and LA-ICPMS using a matrix matched calibration. It was found that the deviation of the results depends significantly on the laser fluence that was varied in fs-LAMS. The detection efficiencies were evaluated by comparing ions detected with atoms removed from the surface during the experiment. Depending on laser energy and the isotope investigated, detection efficiencies varying from 10^{-12} to 10^{-8} were obtained. It was found that a significant fraction of ions was lost at the transition between Einzel lens and the first extraction lens of the TOF. The depth profiling capabilities of the fs-LAFU source were also investigated by analyzing a commercial computer hard disk as sample and a Cr-Ni multi-layer standard reference material (SRM) as reference. In the SRM all individual 57 nm Cr and 56 nm Ni layers could be resolved. The analyses of the hard disk revealed that differences in composition of different layers can be identified. The ablation of glass SRMs was investigated and it was found that those require a substantially higher fluence of 36 J/cm^2 when compared to metal samples. In most cases the sensitivities that were obtained from the ablation of different glasses were relatively similar and reached 10 cps/ppm in the best case. For both laser sources, molecular ions and clusters were observed at varying abundances. Their abundances relative to the corresponding parent ions was found to be affected strongly by the gas dynamics. In summary, limited ion transmission, sample positioning and molecular ion formation were found to be main limitations of the presented setup. To overcome this limitations, a new ion optic in combination with new sample introduction assembly has been developed. Simulations were performed to design the new ion optic

arrangement based on a parabolic electric field which is supposed to be implemented in the near future.

ZUSAMMENFASSUNG

In der vorliegenden Arbeit wird die Entwicklung und Charakterisierung einer neuartigen Laserablations-Ionenquelle für die Elementmassenspektrometrie vorgestellt. Das Konzept von LAMS wurde erstmalig in den 60er Jahren von Honig und Woolston eingeführt. Die zu dieser Zeit vorgestellte Methode wies eine starke Matrixabhängigkeit der Ionenausbeute auf, was den Einsatz von LAMS für quantitative Analysen erschwerte. Ein wesentlicher Grund dafür waren die Nanosekunden-(ns)-Laserpulse, die zur Ablation im Hochvakuum eingesetzt wurden. In dieser Arbeit wird eine neuartige Strategie vorgestellt, bei der die Laserablation bei erhöhtem Druck ausgeführt wird und die Ionen mittels differentiellem Pumpen über eine Expansionsdüse und einen reinen Radiofrequenz-Ionentrichter in das Massenspektrometer überführt werden. Die Kombination aus Expansionsdüse und Ionentrichter ermöglicht eine effiziente Kühlung der lasergenerierten Ionen und deren Trennung vom Buffergas. Dieser Aufbau ermöglicht die notwendige Druckdifferenz zwischen Ionenquelle (bis zu 100 mbar) und Massenspektrometer (10^{-6} mbar) und erreicht gleichzeitig eine ausreichende Anzahl von Kollisionen. In der ersten Phase des Projekts wurde ein 3 ns, frequenzverdoppelter Nd:YAG ($\lambda = 532$ nm) Laser eingesetzt, um den Einfluss von Kollisionsgasdruck und die Transmissionseigenschaften des Ionentrichters zu untersuchen. Erstmals konnte hierbei gezeigt werden, dass die Signalintensitäten der untersuchten Isotope durch diese Kombination gegenüber der Ablation im Hochvakuum erhöht werden können. Die gemessenen Ionensignale wurden um bis zu einem Faktor von 200 erhöht und die transienten Ionenprofile nach dem Laserpuls deutlich verlängert. Für alle detektierten Ionenspezies führte ein Druckanstieg im Ablationsraum zu höheren Ionensignalen. Dies wird auf die zunehmende Kompression der Ionenwolke zurückgeführt. Es wurde gezeigt, dass die Ankunftszeiten der Ionen im Flugzeitmassenspektrometer stark von der Gasdynamik beeinflusst werden. Die Betriebsbedingungen des Ionentrichters wurden hinsichtlich der Ionentransmission und ihrer Massenabhängigkeit untersucht. Die Abhängigkeiten von Ionentransmission von Radiofrequenz-Amplitude und Frequenz entsprachen im Allgemeinen den Vorhersagen für eine Ionentrichterkonfiguration: Niedrigere Amplitude oder höhere Frequenz ergaben eine bessere Ionentransmission für niedrigere Masse-Ladung-Verhältnisse (m/Q) und umgekehrt. Raum-

ladungseffekte wurden festgestellt, insbesondere wenn die Signalintensitäten schwerer Isotope (Pb und Bi) sehr hoch waren. Bei der Analyse von Messingproben wurden allerdings stark unterschiedliche relative Empfindlichkeitskoeffizienten für verschiedene Elemente erhalten. Werte von mehreren tausend für Pb und Bi wurden erhalten, wodurch eine quantitative Analyse problematisch ist. Es wurde dann untersucht, inwieweit Laserablation mittels Femtosekunden-Laser die Quantifizierung verbessern kann. Ein 150 Femtosekunden (fs), frequenzverdoppelter Ti:Saphir (λ= 400 nm) Laser wurde für die Analyse von Metallen und Gläsern verwendet. Beim Einsatz des fs-Lasers wurde ausserdem der Abstand zwischen Probenoberfläche und Düse vergrößert und der effektive Druck in der Ablationskammer gesenkt, um die Ionentransmission zu optimieren. Die Verwendung einer Radiofrequenz von 5 MHz und Amplitude von 20 $_{pp}$ führte zu einem breiteren m/Q-Bereich der simultan transmittiert werden konnte, wenn ein modifizierter HF-Verstärker eingesetzt wurde. Untersuchungen einer Messingprobe ergaben, dass die mittlere Massendiskriminierung über den m/Q-Bereich relativ einheitlich war, mit einer Differenz von sub-% in der Isotopentransmission pro m/Q. Die Wiederholgenauigkeit der Isotopenverhältnismessungen betrug bei Experimenten mit 2000 Laserpulsen pro Analyse etwa 1%, was vergleichbar mit Ergebnissen aus LA-ICPMS Messungen ist. Die Messingprobe wurde mit fs-LAMS und LA-ICPMS mittels einer matrixangepassten Kalibrierung quantitativ analysiert. Es wurde festgestellt, dass die Abweichung der erhaltenen Konzentrationen von den Referenzwerten im Wesentlichen von der Laserfluenz abhängt, die bei fs-LAMS Messungen variiert wurde. Die Detektionseffizienzen wurden durch den Vergleich der detektierten Ionen mit den während des Experiments von der Oberfläche entfernten Atomen abgeschätzt. Abhängig von der Laserenergie und dem untersuchten Isotop wurden Detektionseffizienzen von 10^{-12} bis 10^{-8} erreicht. Es wurde allerdings festgestellt, dass ein signifikanter Anteil der Ionen durch einen nicht optimalen Übergang zwischen der Ionenoptik und dem Massenspektrometer verloren wurde. Die Leistungsfähigkeit bezüglich Tiefenprofilanalyse der fs-LAFU-Quelle wurde durch die Analyse einer handelsüblichen Computerfestplatte als Testprobe und eines Mehrlagen-Cr-Ni-Standardreferenzmaterials (SRM) untersucht. Mit den Analysen der Festplatte konnten die erheblichen Unterschiede in der Zusammensetzung der verschiedenen Schichten ermittelt werden. Im SRM konnten alle einzelnen 57 nm Cr- und 56 nm Ni-Schichten identifiziert werden. Die Ablation von Glas-SRMs erforderte eine wesentlich höhere Fluenz von 36 J/cm^2 im Vergleich zu 1 - 3 J/cm^2, die bei den

untersuchten Metallen verwendet wurden. Die Empfindlichkeiten, die bei der Ablation von Gläsern erzielt wurden, waren für unterschiedliche Proben vergleichbar. Im besten Fall konnten jedoch nur Werte von 10 cps/ppm erreicht werden. Für beide Laserquellen wurden molekulare Ionen und Cluster in unterschiedlichen Häufigkeiten beobachtet. Die begrenzte Ionentransmission, die Positionierung der Probe und die molekulare Ionenbildung stellen zur Zeit die grössten Einschränkungen des Aufbaus dar. . Es wurden Simulationen durchgeführt, um die neue ionenoptische Anordnung auf Basis eines parabolischen elektrischen Feldes zu entwerfen, das in naher Zukunft implementiert werden soll.

RIASSUNTO

Nel presente lavoro viene presentato lo sviluppo e la caratterizzazione di una nuova sorgente ionica di ablazione laser per la spettrometria elementare di massa. Il concetto di spettrometria di massa con ablazione laser (LAMS) è stato introdotto negli anni '60 da Honig. Il metodo presentato a quel tempo dimostrò una forte dipendenza dei rendimenti degli ioni dalla matrice che rese l'uso di LAMS per analisi quantitative impraticabile. La ragione principale di questo può essere attribuita all'utilizzo di impulsi laser dalla durata di alcuni nanosecondi (ns) e dall'ablazione ottenuta in vuoto spinto. In questo lavoro, viene presentata una nuova strategia che utilizza l'ablazione laser ad alta pressione in combinazione con un pompaggio differenziale tramite un ugello divergente convergente (CD) e un imbuto ionico alimentato con tensione alternata nelle radiofrequenze per l'analisi elementare nei solidi. La sorgente ionica di ablazione laser impiega un ugello CD-ugello in combinazione con un imbuto ionico per il raffreddamento collisionale degli ioni generati dal laser e la loro separazione dal gas impiegato. Questa configurazione risulta in una caduta di pressione tra la sorgente ionica (fino a 100 mbar) e lo spettrometro di massa (10^{-6} mbar), consentendo al contempo multiple collisioni. Nella prima fase del progetto è stato impiegato un laser Nd:YAG ($\lambda = 532$ nm) a 3 ns, frequenza raddoppiata per la valutazione della pressione del gas e la caratterizzazione delle proprietà di trasmissione dell'imbuto ionico. E' stato dimostrato per la prima volta che l'uso della combinazione CD ugello-imbuto ionico durante l'ablazione ha migliorato la rilevazione degli ioni rispetto all'ablazione in alto vuoto. I segnali ottenuti dagli ioni sono stati aumentati fino a un fattore 200 e l'efficace raffreddamento degli ioni ha portato a profili transienti più lunghi. I segnali ionici sono risultati aumentati per tutte le specie rilevate quando la pressione nella regione di ablazione è stata elevata. Questo è stato attribuito alla compressione iniziale della nube di ioni. I tempi di arrivo degli ioni al spettrometro di massa sono risultati fortemente influenzati dalla dinamica del gas presente nella configurazione esaminata. Le condizioni operative dell'imbuto ionico sono state studiate, cosi come sono state caratterizzate la trasmissione ionica e la sua dipendenza dalla massa. Le ampiezze RF e le frequenze RF per una trasmissione ionica ottimale si sono rivelate essere conformi alle previsioni per la configurazione dell'imbuto ionico: Un'ampiezza più bassa o una frequenza più alta han-

no prodotto una migliore trasmissione ionica per rapporti massa/carica (m/Q) più bassi e viceversa. Sono stati osservati effetti di carica spaziale, in particolare quando era presente un'elevata quantità di elementi pesanti (Pb e Bi). Sono stati studiati campioni di ottone ed è stato osservato che i coefficienti di sensibilità relativa (RSC) dei diversi elementi differiscono sostanzialmente dall'unità. Sono stati ottenuti valori di diverse migliaia per Pb e Bi, rendendo impossibile l'analisi quantificativa. È stato inoltre studiato se l'ablazione utilizzando laser con impulsi dalla durata di femtosecondi (fs) avrebbe migliorato le capacità di quantificazione della sorgente LAFU. Per l'analisi dei metalli e degli isolanti è stato utilizzato un laser Ti:Sapphire (λ= 400 nm) a 150 fs, a frequenza raddoppiata. Utilizzando il laser fs, la distanza del campione rispetto all'ugello è stata aumentata e la pressione effettiva nella camera di ablazione è stata ridotta per un rilevamento ottimale degli ioni. Un ampio intervallo di trasmissione m/Q è stato trovato quando una frequenza RF di 5 MHz e 20 V_{pp} e 20 V_{pp} sono stati utilizzati con un nuovo amplificatore RF. L'indagine di un campione di ottone ha rivelato che la discriminazione di massa media era relativamente uniforme nell'intervallo m/Q con una differenza di trasmissione isotopica per m/Q inferiore al %. La ripetibilità delle misure del rapporto isotopico era di circa 1% per gli esperimenti con 2000 impulsi laser per analisi, che si confronta ragionevolmente bene con i risultati di LA-ICPMS. Il campione di ottone è stato analizzato quantitativamente da fs-LAMS e LA-ICPMS utilizzando una calibrazione con uno standard con matrice corrispondente. È stato riscontrato che la deviazione dei risultati dipende in modo significativo dalla fluenza del laser che è stata variata in fs-LAMS. Le efficienze di rilevamento sono state valutate confrontando gli ioni misurati con gli atomi rimossi dalla superficie durante l'esperimento. A seconda dell'energia laser e dell'isotopo indagato, sono state ottenute efficienze di rivelazione variabili da 10 $^{-12}$ a 10^{-8}. È stato riscontrato che una frazione significativa di ioni va perduta nella transizione tra la lente di Einzel e la prima lente di estrazione del TOF. Le capacità di profilazione della sorgente fs-LAFU sono state studiate analizzando un disco rigido di un computer come campione e un materiale di riferimento standard multistrato Cr-Ni (SRM). Le analisi del disco rigido hanno rivelato differenze sostanziali nella composizione dei diversi strati. Nell'SRM sono stati identificati tutti i singoli strati da 57 nm di Cr e da 56 nm di Ni. L'ablazione del vetro SRMs è stata studiata e si è riscontrato che richiede una fluenza sostanzialmente superiore di 36 J/cm^2 rispetto ai campioni precedentemente menzionati. Nella maggior parte dei casi le sensibilità che sono state ottenute dall'ablazione del vetro

erano relativamente simili, ma ancora circa 100 volte inferiori, rispetto a quanto visto generalmente con LA-ICPMS. Per i laser utilizzati, sono stati osservati ioni molecolari e cluster con abbondanze variabili. La loro abbondanza rispetto agli ioni progenitori corrispondenti è risultata fortemente influenzata dalla dinamica dei gas.

Per concludere, la limitata trasmissione ionica, il posizionamento del campione e la formazione di ioni molecolari sono risultati essere i principali limiti della configurazione presentata. Per superare queste limitazioni, è stata sviluppata una nuova ottica ionica in combinazione con un nuovo metodo di introduzione del campione. Sono state effettuate simulazioni per progettare la nuova disposizione ottica ionica basata su un campo elettrico parabolico che dovrebbe essere implementato nel prossimo futuro.

ACKNOWLEDGEMENTS

CONTENTS

1

INTRODUCTION

Already in 1963, at the dawn of laser technology, Honig and Woolston [1] focused a laser on the surface of a solid and observed that ions, electrons and neutral species were released in the gas phase. In the following years, the scientific community showed more interest and studies on mass spectrometry with lasers as ionization source were published [2–7]. During the following decade, the Laser Microprobe Mass Analyzer (LAMMA) was developed by Hillenkamp and Kaufmann [8] and later on commercialized by Leybold Heraeus in Cologne. It was the first commercial time of flight instrument implementing a reflectron and employing a laser as ionization source. [9] Using this instrument for the spatial characterization of Ca ions in an embedded thin section of heart muscle cells, Hillenkamp and his collaborators noticed a recurring pattern in the the spectra [10]. Several systematic experiments later and for the first time in 1985 the term Matrix Assisted Laser Desorption ionization (MALDI) appeared in the literature [11]. Since then MALDI has made a significant contribution in the identification of molecules in the field of organic chemistry and of bioanalytical chemistry [12, 13]. However, when scientist tried to exploit laser generated ions for quantitative element analysis, technical difficulties, like a poor reproducibility of the experiments, deviations between the expected composition of the analyzed material and calculated mass fraction were found [14, 15]. These difficulties were the reason why in the field of elemental mass spectrometry Laser Ablation Mass Spectrometry (LAMS) was never becoming an accepted technique. Nonetheless, laser sampling presents various advantages for the analytical chemist, among these one may highlight:

- the possibility to sample practically any solid without the necessity of an elaborate chemical pretreatment,

- solvent waste reduction,

- very simple sample handling together with the reduction of contamination sources,

- the possibility of high sample throughput.

Laser sampling also can exhibit high spatial resolution (depth and lateral) which opens the possibility of precise elemental imaging.

The separation of sampling and ion generation has been one strength of Laser Ablation Inductively Coupled Plasma Mass-Spectroscopy (LA-ICPMS), since it allows to individually optimize both steps [16]. For this reason LA-ICPMS has become an established, analytical technique widely used for the detection of element- and isotope composition for example in geochemistry [17–20], materials sciences [21], cell biology [22–24], archaeometry [25–27] and forensics [28–30]. However, the need of a separate ion source in addition to laser ablation sampling also presents major drawbacks: spectroscopically, due to intense signals of the plasma background ions and economically, because of the substantial running cost of an Argon-based ICP. Nonetheless, LA-ICPMS has become widely distributed in different analytical laboratories and applied when compared to other direct techniques for the analysis of solids such as Secondary Ion Mass Spectrometry (SIMS) [31], X-ray fluorescence (XRF) [32, 33] or Laser Induced Breakdown Spectroscopy (LIBS) [34] due to availability, sensitivity or relatively simple operation. In contrast, laser ablation mass spectrometry, is conceptually much simpler and cheaper in operation. However, moderate figures of merit, mostly with respect to quantification accuracy and sensitivity have always been the major limitation. Matrix effects have been frequently observed, causing relative sensitivities of the elements in different sample materials to differ by more than one order of magnitude [35].

1.1   RENAISSANCE OF LASER ABLATION MASS SPECTROMETRY (LAMS)

In the last decade, the LAMS technique has regained substantial attention as analytical tool for element analysis (Tab. 1.1). Many parameters including laser wavelength, laser pulse duration, laser pulse energy, ambient pressure and sample material amongst others influence ion formation [36] and their properties (see laser ablation, section 1.6), making mass spectrometric analyses with laser generated ions not straightforward. Different research groups [37–40] have developed new strategies for the compensation of energy spread of the ions and new laser sources have been employed to achieve better representation of the ion beam's stoichiometry compared to the sample.
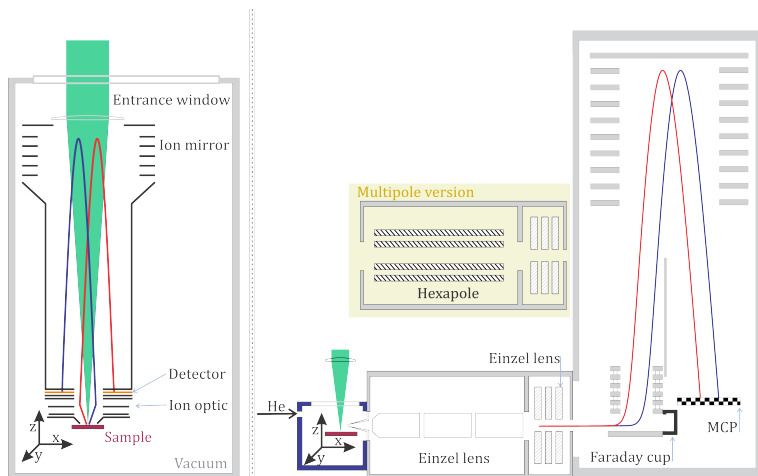
FIGURE 1.1: *Left :* Laser-ionization time-of-flight mass spectrometer with axially symmetric ion-beam set up used in [40, 41]. *Right:* Orthogonal time-of-flight mass spectrometer which utilized He as buffer gas to cool the ions [37]. Schematics not to scale.

One approach to reduce the wide kinetic energy distributions of the ions is a process called collisional cooling [42, 43]. If a buffer gas is utilized, the energy spread can be reduced by thermalization of the species through collisions (see collisional thermalization, section 1.7). The group of Huang has exploited this strategy for LAMS and developed an orthogonal time-of-flight mass spectrometer which utilized He as buffer gas to cool the ions (Fig. 1.1) [37]. The ions were extracted from the ablation region using a noz-

zle and transported by means a radio-frequency only (RF-only) hexapole ion guide to an orthogonal Time of Flight Mass-Spectrometer (TOFMS). To reduce mass to charge (m/Q) dependent transmission produced by the hexapole system [44] a set of cylindrical Einzel lenses was later replacing the ion guide [45]. At the same time, the sampling nozzle was placed orthogonally to the laser plume to sample ions with smaller kinetic energy distributions [46]. However, these collisions also led to ion scattering, whose magnitude was largely depending on the mass of the analyte. Lighter ions were thus less efficiently sampled through the orifice leading to unwanted sensitivity loss and increased mass bias. To extract the ions from a buffer gas more efficiently and less mass dependent an approach based on a so-called ion funnel was proposed by Johnson et al. [38]. This strategy can also be found in the instrument presented by Cui et al. [47]. An ion funnel is used for the extraction of the ions before the high vacuum region of the TOFMS, however both reports did not specify if and how the ion funnel was actually operated. Work of Sovevy is mainly focused on the development of new ion optic system aiming time focusing using a "wedge-shaped" reflecting mirror which is simultaneously used as integrated part of ion analyzer [48–50]. The idea behind this method is to compensate for the ion energy aberrations with specular aberrations produced in the analyzer, merging an electric sector with a reflectron. The group of Wurz has developed a miniaturized reflectron-type TOFMS mass spectrometer which was designed for in situ measurements on planetary objects [39, 40] (Fig.1.1). The ablation takes place in high vacuum circa 1 mm away from the entrance of the flight tube. Only positively charged species can enter the ion optical system where the ions are focused and accelerated towards a cylindrical reflectron. The ions hit a multi-channel plates and the generated current is then digitalized with two high speed analog digital converter (ADC) cards.

Initially LAMS was showing limited reproducibility of the relative sensitivities for different elements across various matrices, making quantitative analyses difficult. It was therefore tried to normalize the physical and chemical properties of the sample (e.g. matrix effects, ionization potential, melting point of the trace element, dissociation energy of analyzed compounds) and of the laser ion source parameters for different measurements using the Relative Sensitivity Coefficient (RSC) defined as:

$$RSC = \frac{I_x/c_{IS}}{c_x/I_{IS}} \tag{1.1}$$

where I_{IS} and I_x are signal intensities, c_{IS} and c_x are the mass fraction of an internal standard (IS) and for the analyte of interest (x) respectively. If the RSC is unity, the ratio of the signals generated is directly proportional to the ratio of the mass fractions present in the sample.

The use of ultrashort laser pulses (tens of femtoseconds) in particular, has improved the measurement accuracy [51]. By using infra-red (IR) femtosecond ablation and ionization, Riedo et al [51] were able to show that the highly similar relative sensitivity factors of metallic and non-metallic elements could be achieved (i.e. relative sensitivity coefficients (RSC) between 0.9 and 1.16 for C, Si, P, S and V relative to Cr). The previously used ultraviolet (UV) or IR nanosecond lasers used showed RSCs varying by 3 to 4 orders of magnitude [51]. Also Zhang et al. [52] showed that IR femtosecond LAMS can produce RSFs near unity for most elements in different materials. Only elements with ionization energies > 10 eV were found to reproducibly be ionized at a lower degree. The differences between fs and ns laser for depth profiling have been investigated by Huang et al. [53]. In their work, a laser ionization orthogonal time-of-flight mass spectrometer (LI-O-TOFMS) was operated using a ns laser ($\lambda = 1064$ nm, $\tau = 5$ ns, 2 Hz, 9.0 and 32×10^9 W/cm^2) or fs laser ($\lambda = 1030$ nm, $\tau = 500$ fs, 2 Hz, 4.4 and 14×10^{12} W/cm^2) for the profiling of samples with various thicknesses with conductive (Rh (160 nm) / Au(20 nm) / Pd (1100 nm) layers on Cu) and nonconductive (Cr (1500 nm)/ Ni (200 nm)/ Cu (7000 nm) layers on Acrylonitrile butadiene styrene) substrates. It was found that the average ablation rate (AAR), defined as the thickness of layer divided by the number of pulses needed to reach halve the signal intensity, differed for the two laser sources. Specifically, for the copper substrate an AAR of 700 nm was found using the ns laser, while 55 nm was obtained for the fs laser. To probe the nonconductive substrate sample the laser irradiances were increased and the pressure in the source was reduced in attempt to better ionize elements with higher ionization energies present in the substrate. On this sample it was not possible to distinguish the top two layers when nanosecond laser pulses were employed: Elements from the top three layers appear in the signal of first laser pulse, an AAR was calculated to be 1900 nm. In the case of fs-pulse an AAR of 240 nm was found. Cui et al. [47] have used time-of-flight mass spectrometry coupled with an ion funnel and a ultrafast laser ($\lambda = 800$ nm, $\tau = 75$ fs, 4.5 $\times10^{12}$ W/cm^2, 1 kHz) to investigate its depth profiling capabilities. Due to technical difficulties however it was only possible to ablate with ambient pressure of 10^{-6} mbar and not in the pressure regime that was aimed originally. The sample analyzed consisted

in a ~ 330 nm Ta_2O_5 film deposited on Ta foil. There was no attempt to calibrate the number of laser pulses with the actual depth profile of the Ta_2O_5 film and an estimation for the removal of material was made using the signal drop in K^+ signal (arising mostly from surface). Grimaudo et al. [54] have employed a miniature time-of-flight mass spectrometer and ultrashort pulsed laser ablation ($\lambda = 775$ nm, $\tau \sim 190$ fs) for chemical depth profiling of copper films. An ablation rate at the sub-nanometer level for a single laser pulse and a high detection sensitivity of ~ 10 ppb and dynamic range $\geq 10^8$ was reported. However, subnanometer vertical resolution was achieved only at the lowest laser irradiances (3.0×10^{12} W/cm^2) with a mean ablation rate of ~ 0.3 nm of Cu, but a stable ablation process was achieved only when higher energies were applied resulting in an ablation rate of 1.56 nm/pulse. The same group used the developed method to investigate different copper based layer structures [55, 56].

In order to achieve lower ablation rate the group of Huang [57] separated the ionization step from the sampling using 2 different lasers. A low-irradiance laser (5 ns, 532 nm, 9.0×10^7 W/cm^2) focused on larger surface (~ 150 mm) was used for desorption of a small number of atoms and a high-irradiance laser was fired with a delay for post ionization (5 ns, 266 nm, 10×10^9 W/cm^2). All measurements were performed with a background pressure of 3×10^{-7} mbar and a reflectron time-of-flight mass analyzer was utilized. The AAR was calculated to be 0.026 nm per pulse, corresponding to sub- monolayer removal per pulse. High spatial resolution and possible high repetition rate make LAMS an attractive candidate to characterize the spatial distribution of different analytes in a solid sample generating images. Using the setup already mentioned, the group of Huang determined the distribution of elements in mineral samples. Using a spot size of 50 μm, simultaneous, sensitive, and semiquantitative imaging of metals and nonmetals with detection limit down to 0.1 ppm were performed. [58] The same group used the method for imaging of deep-sea Pacific polymetallic nodules [52]. If more than one layer is ablated or depth profiling experiments are performed close to each other it is possible to create a 3D image of the sample. Example of such 3D-image have been obtain in the group of Wurz [59] and Huang [60].

Table 1.1: Reports on element analyses using LAMS or related techniques published between 2009 and 2019. Not included are papers on fundamental aspects of ablation or ionization and applications of only molecular species. ‡ Open Air LAMS

Method	Analyte(s)	Sample(s)	Laser source	Ablation spot	Imaging	Reference
LAMS	Major and trace elements	Steel	355 nm, 4.4 ns	20 μm		[46]
LAMS	Major and trace elements	Tea Leaf	532 nm, 4.4 ns	50 μm		[61]
LAMS	Major and trace elements	Steel	266, 532, 1064 nm, 4.4 ns	20 μm		[62]
LAMS	Cr, Fe, Ni, Zn, Sn, Pb	Metals	532 nm, 7 ns	124 μm*		[63]
LAMS	Gd isotopes	Metal coated or metallic microparticles	532 nm	n.r.	(yes)	[64]
LAMS	Fe-O Species	Iron Oxides	266, 532, 1064 nm, 5 ns	50 μm		[65]
LAMS	Major and trace elements	Metals and Minerals	355 nm, 4.4 ns	20 μm		[66]
LAMS	Non-metals	Cu powder	532 nm, 4.4 ns	20 μm		[67]
LAMS	Major and trace elements	Al-mineral	532 nm, 4.4 ns	n.r.		[58]
LAMS	Major and trace elements	Steel, Minerals	1064 nm, 4 ns	10 μm		[68]
LAMS	Matrix elements	Steel, gypsum	532 nm, 7 ns	600 μm		[38]
LAMS	Major and trace elements	Metals	800 nm, 45 fs	32x16 μm^2	yes	[47]
X-ray LAMS	Layer compounds	Multilayer system	46.9 nm, 1.5 ns	82 nm	yes	[69]
LAMS	Major and trace elements	Metals and minerals	1064 nm, 4.5 ns / 1030 nm, 500 fs	40 μm	yes	[52]
LAMS	Major and trace elements	Iron, Steel, Pb	266 nm 4 ns	20 μm		[39]
LAMS	Major and trace elements	Polymetallic nodules	532 nm, 4.4 ns	40 μm	yes	[69]
LAMS	Major and trace elements	Cu	1064 nm, 4.5 ns / 1030 nm, 500 fs	40 μm	yes	[70]

Method	Analyte(s)	Sample(s)	Laser source	Ablation spot	Imaging	Reference
LAMS	Trace elements	Single cells	1030, 500 fs	80 μm		[71]
LAMS	Pb-Isotopes	PbS	266 nm, 3 ns	20 μm		[41]
LAMS	Major and trace elements	Meteorite	266 nm, 4 ns	20 μm		[72]
LAMS	Metalloporphyrines	Powder pellets	532 nm, 4.4 ns	45 μm		[73]
OALAMS ‡	Pb, Al, Si	Metals	1032 nm, 600 fs	n.r.		[74]
X-ray LAMS	Layer compounds	Multilayer system	46.9 nm, 1.5 ns	n.r.	yes	[75]
LAMS	Cu, Polymers	Multilayer system	775 nm, 190 fs	14 μm	yes	[55]
LAMS	Major and trace elements	Pressed metal powders, Iron meteorite	1030 nm, 500 fs	50 μm	yes	[59]
X-ray LAMS	U, Th	Glass	46.9 nm, 1.5 ns	75 nm	yes	[76]
OALAMS ‡	Pb, U Isotopes	Graphite	248 nm, 23 ns	0.8x1.6 mm^2		[77]
LAMS	Major elements	CuSnPb	775 nm, 190 fs	14 μm	yes	[60]
X-ray LAMS	Major and trace elements, molecular species	CoNCN	46.9 nm, 2 ns	1 μm	yes	[78]
LAMS	Matrix elements	Sn, Cu Solder	775 nm, 190 fs	20 μm	yes	[79]
LAMS	U isotopes	U-Oxide particles	193 nm, 15 ns	n.r.	(yes)	[80]

1.2 THE LASER ABLATION ION FUNNEL MASS ANALYZER (LAFUMA)

In this work, laser ablation and ionization is carried out in a buffer gas, similar to the approach used by Huang et al. [62] but employing a combination of a Convergent-Divergent (CD) nozzle with an ion funnel instead of a skimmer. Different pressure regimes are present in this concept, aiming at an efficient transmission of the ion beam towards a time-of-flight mass spectrometer. The ions are thermalized within an ambient pressure of circa hundred mbar and then extracted into the high vacuum needed for mass spectrometry (Fig. 1.2). Ions are produced in a helium environment, whose pressure is controlled via the gas flow upstream the nozzle and the pump speed applied in the ion funnel region. Through gas dynamics, the ions are then transported from the ablation region into the ion funnel, where the buffer gas is removed.
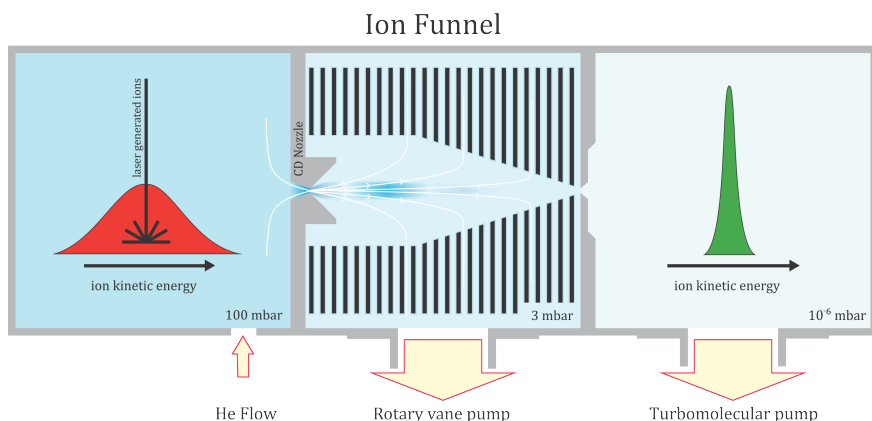
FIGURE 1.2: Laser Ablation/ionization is performed in helium buffer gas (<100 mbar), whereby the laser plasma is confined and a first thermalization of the produced species occurs. The ions are then extracted and pressure is reduced in the ion funnel region, where additional thermalization is achieved. The ions are then transferred into the high vacuum region, wherein mass spectrometry experiments are performed.

The ion funnel (section 1.8) interface is evacuated using a conventional rotatory vane pump and the RF-only ion funnel is employed to radially focus charged species. The ions are separated from the buffer gas and transferred into the ion optic region, where molecular flow regime is assured using a turbomolecular pump. This particular configuration of an

ion funnel renounces the traditional superimposed DC gradient [81], used for the axial acceleration of the ions and makes its construction simpler. In the following section, a brief theoretical description of the various relevant conditions of the setup will be presented.

1.3   CONDITIONS FOR LASING

The simplified description presented in this section is based on Einsteins "The Quantum Theory of Radiation´´ [82], for a detailed derivation the reader is referred to work of K. Renk and O. Svelto [83, 84] . An electron in the lower level of a two-level system, can be excited to an excited state by photon absorption. Once excited, the electron may lose energy and move from the upper state to the lower one. The energy difference between the two states, can be released in form of a photon. The decay of the excited system can occur in two different paths: the first being a spontaneous emission the second being stimulated by a radiation field (see Fig. 1.3). Spontaneous emission is characterized by arbitrary properties of the emitted photon (direction of propagation, polarization, phase). Whereas the photon arising from stimulated emission will have properties identical to those of the incoming radiation. This optical replication is the basis for the operation of a laser.
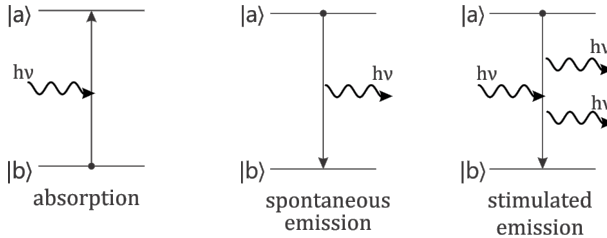
FIGURE 1.3: Interaction of a two-level system with a radiation field. The black dot labels the state of the system prior to the radiative process.

Laser stands for *Light Amplification by Stimulated Emission of Radiation*, however the stimulated amplification of light alone is not sufficient for the operation of a laser. In order to create a laser a positive optical feedback structure is needed, where the photon flux increases with each pass of the photons through a gain medium. This is usually realized by enclosing the gain medium by two mirrors, one being partially reflective. The major part

of the radiation is reflected back into the cavity, where it is amplified further. At each pass a small photon flux is allowed to escape through the partially reflective mirror; this fraction forms the laser beam. In practice it is inefficient to use a two-level gain medium, since the rate of emission will be on the same order as the one of absorption. In order to avoid this problem, a gain medium with more energy levels can be used, which presents a radiation-less transition to an intermediate level (see Fig. 1.4).
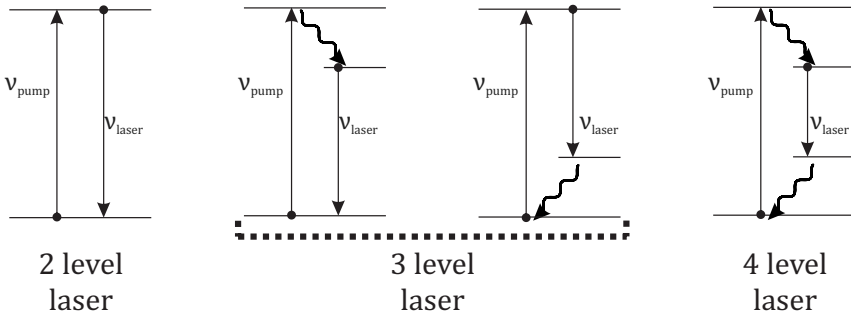
FIGURE 1.4: Operation principles of the three most common types of lasers

The ground state electron can be excited independently since the stimulated emission is occurring at a lower energy. The excitation process ("pumping") is usually achieved using a shorter wavelength than the emitted radiation. The radiation-less transition, shown as a wavy line, can either serve to populate the upper level or to depopulate the lower level of the laser transition. If a second radiation-less transition is present in the system, a 4-level laser, the lasing transition is decoupled form the pump transition by two steps.

1.4   SHORT PULSE LASER

A short pulse laser is a laser capable of emitting pulses of light with a temporal duration in ranging from nanoseconds to tens of nanoseconds. The most common way to obtain such laser pulse is the Q-switching (sometimes referred as *giant pulse*) technique [84].
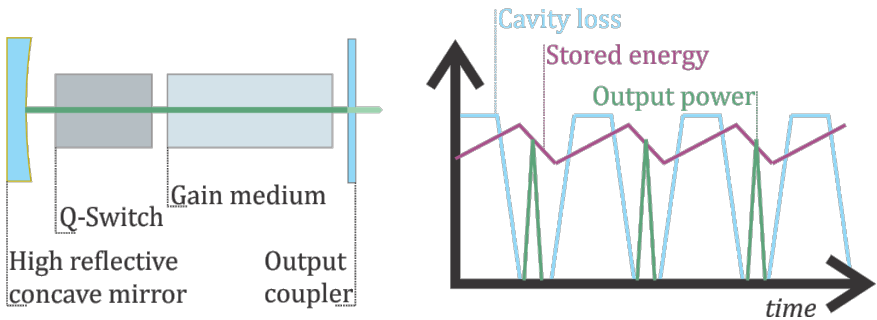
FIGURE 1.5: *Left:* Schematic representation of a laser cavity with Q- Switch. *Right:* Temporal evolution of gain and losses in an Q-switched laser.

Q-switching refers to the fact that the formation of laser pulses is achieved by altering the quality factor (Q-value) of a laser resonator. The Q-value is a parameter that describes the resonance behavior of an underdamped harmonic oscillator. It is defined as the ratio between the energy stored per pass and the energy dissipated per pass. A laser essentially being an optical oscillator it is possible to use the Q-factor to describe the loss of a lasing cavity. For continuous laser sources the Q-factor of the laser cavity stays constant, however a periodical modulation allows to create pulsing laser sources. When the Q factor is kept artificially low, by placing an additional optical element in the cavity (Fig. 1.5, left), energy will gradually accumulate in the laser medium because stimulated emission cannot dominate the population decay. At this point, the laser medium acts as energy storage with energy only slowly released by spontaneous and non-radiative transitions. When the pump energy, stored in the laser medium, has approached the maximum possible level, the introduced loss (often an electro- or acousto-optical induced change) is rapidly removed. This results in a fast electron relaxation, producing a high-power pulse of light (Fig. 1.5, right) [84, 85]. The rapid change in cavity Q-factor is called Q-

switching. For a fixed gain medium, the Pulse duration is then depending on the cavity round-trip time (length of the cavity) [86].

1.4.1 *Nanosecond Nd:YAG Laser*

One of the most frequently used solid state ns lasers in analytical chemistry is the Nd:YAG laser. The active medium in this lasers is a synthetic crystalline material (Yttrium Aluminum Garnet, $Y_3Al_5O_{12}$) doped with Neodymium atoms. It is a four-level system as depicted in the energy level diagram in figure 1.6, which allows for efficient Q-switching. The pumping can be done either using laser diodes or a flashtube. Lamp pumping is possible due to the broadband absorption mainly in the 800-nm region of the gain medium. The higher state of the gain medium used for lasing is mainly the $^4F_{5/2}$ level with a pumping wavelength around 800 nm. The excited electrons relax to the upper laser level ($^4F_{3/2}$) via fast, radiation-free transitions. [84, 87] This level has a fluorescence efficiency greater than 99.5% and a radiative lifetime of 230 μs [88]. The transitions starting from this level have different fluorescence probabilities. The most dominant transmission occurs between the upper $^4F_{3/2}$ and the $I_{11/2}$ level, corresponding to a wavelength of 1064 nm. Starting with that wavelength, outputs at 532, 355, 266 and 213 nm can be generated by frequency doubling, frequency tripling, frequency quadrupling and frequency quintupling, respectively. In Q-switch operation it is possible to adjust the laser output energy by changing the delay between pumping and Q-switching (Fig. 1.6). Thereby it is possible to control the population of $^4F_{3/2}$ level available for stimulated emission.
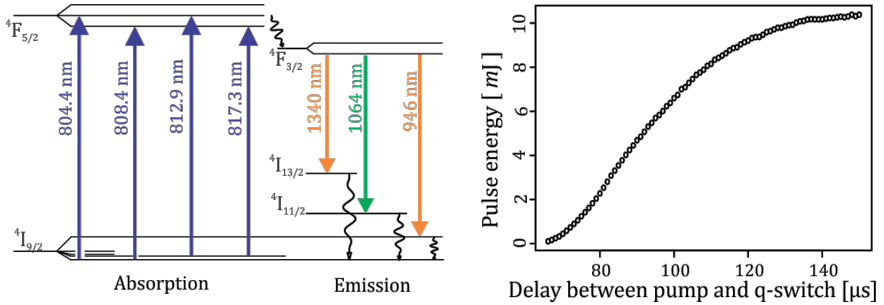
FIGURE 1.6: *Left:* Energy level structure and common pump and laser transitions for Nd:YAG laser. Level notation is accordingly based on this scheme and the symbol characterizing each level is in the form $^{2S+1}L_J$, where S is the total spin quantum number, J is the total angular momentum quantum number, and L is the orbital quantum number. *Right:* Laser energy output in function of Q-switchin timing. The measurements were performed using a frequecy doubled Nd:YAG (Minilite PIV,Continuum Electro Optics Inc., Santa Clara, USA) and changing the delay between pumping and Q-switching.

1.5   ULTRASHORT PULSES

The generation of ultrashort light pulses, with duration below a picosecond, is usually achieved using a technique known as mode locking. The term mode locking originates from a description of the frequency domain of the laser pulse and was investigated already shortly after invention of the laser [89]. Depending on the laser medium (gain) it is possible to emit and amplify simultaneously a broad range of frequencies in a laser resonator, with the underlying condition that the cavity length must be an integer multiple of the selected wavelength (resonance condition). Each wavelength produced represents a "longitudinal mode". When a laser medium is capable of amplification of more than one mode it is called "multimode". An ultrashort pulse arises from the spatial superimposition of different longitudinal modes of the laser, lasing in a phase-synchronous fashion: the electric field associated with the different modes must add constructively at one point and destructively elsewhere to create a high intensity spike (Fig. 1.7).

To force the longitudinal modes to oscillate synchronously, an optical element is introduced in the laser cavity, usually a modular absorber. In
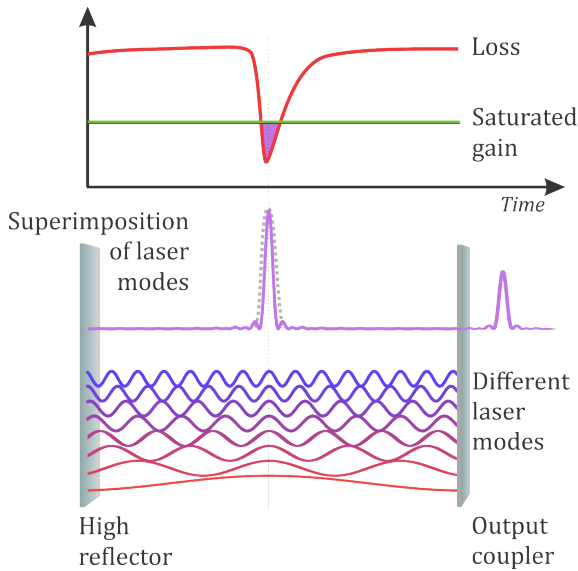
FIGURE 1.7: Pictorial representation of mode locking

a similar fashion to a Q-switched laser, the absorber varies the loss in the cavity periodically. The loss modulation has to correlate with the roundtrip frequency of the laser resonator and through this periodic loss modulation, optical energy is transferred into the neighboring axial modes. The larger the number of frequency components involved, the shorter can be the duration of the generated pulses. This implies that if a laser pulse is very short in time, then it must have a broad wavelength spectrum. This relationship between the temporal and spectral profiles of the laser is governed by the Heisenberg uncertainty principle (also known as Fourier relationship) $\Delta\nu$ $\Delta t \geq 1$ where the ν is the spectral bandwidth. In active mode locking the loss is externally modulated, whereas in passive mode locking the laser pulse circulating in the cavity medium is modulating the loss. In a passive mode locked laser the loss medium is a saturable absorber (or an artificial saturable absorber), which is an optical device that exhibits an intensity-dependent transmission. A saturable absorber has a very short recovery time resulting in a fast loss modulation, which allow the generation of laser pulses with few femtoseconds duration. Commonly used is an artificial saturable absorber based on Kerr lensing [90]. A nonlinear response of this optical medium is used to allow only the portion of the laser with

higher intensity to oscillate in the resonator, stripping the wings of the pulse.

1.5.1   *Femtosecond Laser, Ti:Sapphire*

The femtosecond laser used in this work is a passive mode locking Titanium-doped sapphire solid state laser (Fig. 1.8) . The pump laser for the optical oscillator is a continuous wave (cw) frequency doubled (532 nm) neodymium doped yttrium vanadate (Nd:YVO$_4$) laser. The pump laser is focused via a lens and mirrors through the Ti:Sapphire crystal. The slit allows only narrow beams of high intensity light to pass through to the output coupler, which allows some of the pulse to pass through to form the laser output and reflects the rest back for another round-trip of the system. The prism pair equalizes the time it takes for the slightly different wavelengths in the laser pulse to travel back and forth across the laser, thus ensuring that the short pulse maintain its original shape.
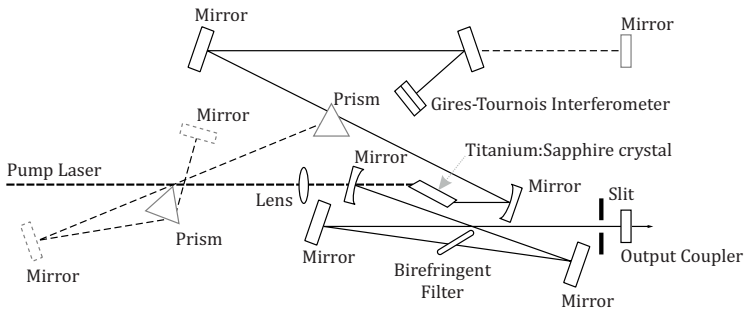
FIGURE 1.8: Optical arrangement of the Coherent Inc., Mira seed laser.

1.5.2 *Chirped-pulse Amplification*

The generated laser pulse in the femtosecond frame has to be amplified in order to provide sufficient energy density for laser ablation to occur. If the fs-pulse would be amplified directly to reach the energy needed for ablation, the amplified pulse would damage the gain medium. To avoid this, so called chirped pulse amplification (CPA) can be used. It exploits the previously mentioned Fourier relationship, namely that an ultrashort pulse has a broad spectral bandwidth. Using a dispersive element (either prism pairs, gratings pairs, or optical fibers) the pulse is stretched to picoseconds duration. The stretched pulse has a temporal/spatial distribution of its wavelengths (i.e. chirp). This reduces the peak power and increases the beam waist, allowing amplification trough a broadband lasing medium, pumped by a pulsed laser (Fig1.9).
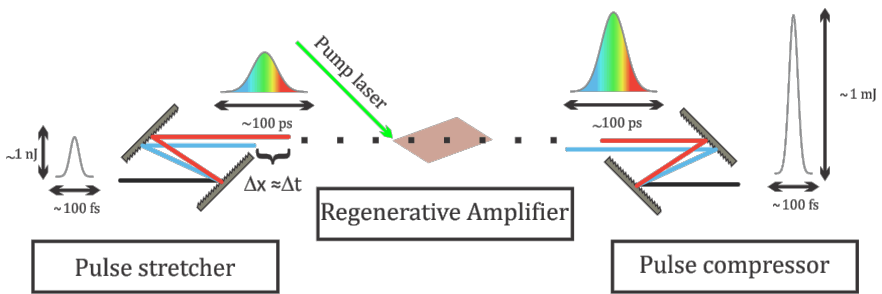
FIGURE 1.9: Schematic of chirped pulse amplification (CPA)

After the amplification step, the pulse is temporally/spatially compressed using an optical element with opposite dispersion, removing the chirp and resulting in a pulse with a duration similar to the input pulse.

In LAMS, material evaporation and ionization are obtained using a high energy laser pulse. The interaction of such a laser with a solid involves many processes including heating, melting, vaporization, ejection of particles as well as plasma formation and expansion. Depending on the material and the type of laser irradiation (i.e. wavelength, fluence, pulse duration) different mechanisms for material ejection and ionization can be observed. The major processes will be described briefly. For a more extensive treatment the reader is referred to the work of Bauerle and of Gamaly [91, 92]. When the surface of a solid is irradiated by a laser beam, a portion of the light will be reflected and the rest will be absorbed by the material. Considering only linear optical phenomena, the absorption in the irradiated material is depth depending and it is dictated by material's absorption coefficient α according to the Beer–Lambert law,

$$I(z) = I_0 e^{-\alpha z} \tag{1.2}$$

where I_0 is the light intensity after considering reflection loss, α is the absorption coefficient (specific for each material) and z describes the depth [91]. The absorption of optical energy is mediated by the excitation of electrons from their equilibrium states to some excited states [93]. In the case of metals is the incoming photons are absorbed by the free electrons, whereas for semiconductors and insulators by vibrations [91]. In the same way that a body in water does not gain energy just fluctuating with a wave, an electron does not increase its net energy at the end of the optical cycle when just oscillating along the electromagnetic wave. In order to gain net energy, the electron has to collide with a third body (mainly other bound electrons or lattice species) and through dephasing, it can absorb energy. This process is known as inverse Bremsstrahlung (or Joule heating process) [94]. The initial electronic excitation is followed by secondary processes which happen at different time scales. The pulse duration then plays an important role since it dictates the processes occurring during the irradiation of the material. If the laser pulse is longer than the phonon relaxation time (>ps) it is commonly called long pulse, if it is shorter (< ps), ultra-short pulse. [93, 95] If the laser pulse duration is longer than the phonon relaxation time (e.g. ns), the mechanism can be regarded as thermal processes involving quasi-equilibrium thermodynamics [91]. The laser radiation is considered merely as a very concentrated heat source and the absorbed laser energy can be seen as transformed into heat, which first melts, then vaporizes the material in the timescale of tens to hundreds of picoseconds.

The ejected material interacts further with the incoming radiation forming an opaque plasma, which shields the surface. The ionization taking place in the plasma greatly influences the dynamics of the plasma plume [96] changing the properties of the formed plasma. The ionization process is usually regarded as thermal for laser with fluences near the ablation threshold and can therefore be estimated using the Saha equation [97]. If the fluence is much higher than the ablation threshold, ion generation occurs mainly by photoionization and the degree of ionization can be estimated using the Boltzmann equation [97, 98]. The expansion dynamics of the ejected species can be described mainly by hydrodynamic expansion in vacuum and electrostatic repulsion, depending mainly on the laser parameters. It has been shown that Anisimov's model [99], which is based on hydrodynamic motion regardless of electrostatic interaction, can describe the motion of ionic species after the ablation event [100]. In contrast to ns laser pulses, where the dissipation of energy in the bulk material and material removal take place during the pulse duration, in the case of femtosecond laser pulses a finite amount of energy is deposited on the target instantaneously compared to the other process taking place. This results in a more complex ablation event, consisting of thermal and non-thermal processes. When a laser with energy sufficient for ablation is shone on a surface the material is driven into a non-equilibrium state with large excess population in the excited states. The absorption in no longer described by the Beer-Lambert law, since nonlinear processes become significant for high peak intensities and photoionization starts to play a major role. The mechanism governing the material ejection during the ultrashort laser ablation depends on various parameters (electric properties of the sample, laser wavelength and fluence), and is still subject to investigations and the scientific community is not yet in complete agreement on the theory. However the most widely accepted models are phase explosion or homogeneous nucleation of gas bubbles [101–103] (the irradiated matter enters the metastable region of the phase diagram (below the binodal), causing homogeneous nucleation of gas bubbles and eventually dissociation into liquid and gas), spinodal decomposition [102, 104] where the system is brought below the spinodal into a mechanically unstable zone of the phase diagram.

1.6.1   *Phenomenological description of laser produced ions*

Although the ablation mechanism is not yet fully understood, many studies have been performed to investigate the origin of the kinetic energy (KE) and angular distributions of the ejected ions. The majority of these studies have been performed using nanosecond laser pulses in vacuum, where shifted Maxwell–Boltzmann–Coulomb (MBC) distributions could be fitted on the KEs of ejected ions [105–114] and a $cos^n(\theta)$ function for the angular distribution [115, 116], with the majority of the ions emitted normal to the target's surface. Different angular distribution of the ejected ions were found for ions with different kinetic energy, where less energetic ions were observed to spread across larger angles and more energetic ones remain close to the normal axis. The photon energies play a major role in the formation ions: shorter wavelength ablated more material [117] and produced ions with a smaller axial expansion [118–120] and narrower angular distribution [121, 122] when compared with longer wavelength but similar fluence. Another major role in the expansion dynamics of the laser produced plasma is played by the ambient gas, which causes effects like thermalization of the ablated species, diffusion, recombination, formation of shock waves, and clusters [123]. During an ablation event in presences of a background gas, some energy is transferred and absorbed by the gas resulting in shockwave generation and propagation. The molecular mass of the background gas affects also the strength of the shock wave produced with heavier gas atom showing a more powerful shock wave [124]. Through simulation it was possible to reveal that the plume expansion tended to be slower and more confined in a heavier ambient gas [125] and that expansion velocity in an ambient gas was reduced by an order of magnitude compared with the expansion in vacuum [125, 126]. The ambient pressure also affects the plasma plume kinetics significantly [126–129] by lowering the population of energetic ions when ablation takes place in a buffer gas [130, 131]. When the pulse duration of the laser employed is in the femtosecond regime, two different ion velocity distributions are found. A population of slower ions can be explained using a thermal model and fitted with a shifted Maxwellian distribution. The faster ions are due to a time-dependent ambipolar electric field, generated by the ejection of electrons after the pulse irradiation, present a Gaussian energy distribution [100, 132–134]. When lasers with similar fluence but different pulse duration (ns vs fs) are compared, it was found that fs irradiation produced ions with significantly higher and broader kinetic energy distribution, but

a narrower angular distribution [135–140]. A more detailed study on the topic can be found in references [36, 100, 134].

1.7 COLLISIONAL THERMALIZATION

Collisions with an inert buffer can be used to reduce the energy distribution ions. [43] The presence of a stagnant buffer gas thus causes ions to loose kinetic energy and eventually reach thermal equilibrium with the gas, thus narrowing their velocity distribution (Fig. 1.10).
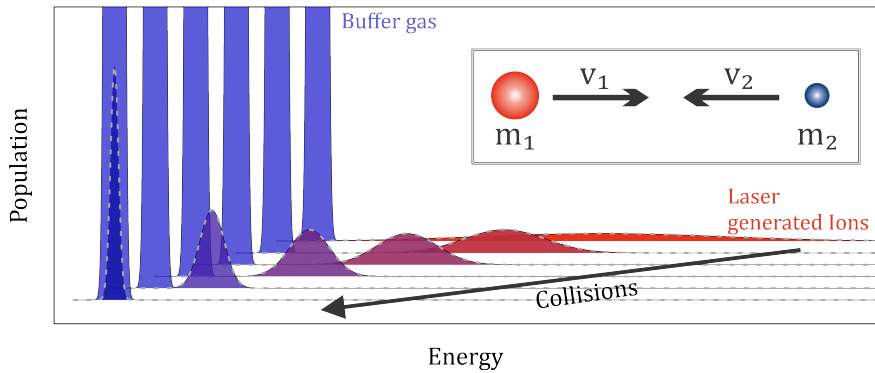
FIGURE 1.10: Schematic representation of the ion kinetic energy thermalization. In red, a Gaussian distribution representing the kinetic energy distribution of laser generated ions, in blue the Gaussian distribution representing the one of buffer gas. The high energetic ions transfer part of the excessive energy trough collision to the inert gas, if sufficient collisions take place a thermal equilibrium is reached. Since the amount ions is very small in comparison to the amount buffer gas atoms, the final temperature can be approximated by the one of the gas.

The interactions between a species A (e.g. an ion) and specie B (e.g buffer gas atom) are collisional processes, and different outcomes are possible,

depending on the energy transformation, three categories can be differentiated:

$$A + B \longrightarrow \begin{cases} A + B \ \ elastic \\ A + B^* \ \ inelastic \\ A + B + C \ \ inelastic \\ C \ \ Absorption/Reaction \end{cases} \tag{1.3}$$
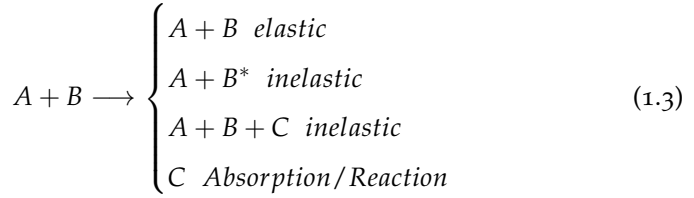
Working with an inert buffer gas and atomic ions, the collision processes can be approximated as elastic. A short description of elastic (no internal excitation) non-reactive collisions will be given in the following. Following the conservation of momentum and energy, the energies and the velocity of the involved species after collision are given by:

$$v_1 = \frac{m_1 - m_2}{m_1 + m_2}v_1' + \frac{2m_2}{m_1 + m_2}v_2' \tag{1.4}$$

$$v_2 = \frac{2m_1}{m_1 + m_2}v_1' + \frac{m_2 - m_1}{m_1 + m_2}v_2' \tag{1.5}$$

$$E_1' = E_1 \left[\frac{m_1^2 + m_2^2}{(m_1 + m_2)^2} \right] \qquad E_2' = E_1 - E_1' \tag{1.6}$$

where m are the masses of the collision partners (index 1 and 2), E and E' are the kinetic energies before and after the collision respectively, v and v' are the velocities before and after the collision [141]. The amount of energy absorbed by the buffer gas in each collision and the velocity vector of the ions are inherently dependent on the masses of the involved species. A greater fraction of energy is absorbed when the mass of the buffer gas increases, resulting in a more efficient thermalization. However, backscattering can be observed, when a lighter object collides with an heavier one. The number of collisions that an ion can undergo in a buffer gas is depending on pressure, size and relative velocities of the collision partners. The kinetic theory of gases defines the mean free path as the average distance between collisions, and can be described by:

$$l = \frac{k_b T}{\sqrt{2}\pi d^2 p} \tag{1.7}$$

Where where k_B is the Boltzmann constant, T is the absolute temperature, $\sqrt{2}\pi \ d^2$ is the effective cross-sectional area for spherical particle, and p is the pressure. An estimation of the different mean free path for the different pressure regime present in this work can be found in table 1.2.

TABLE 1.2: Calculated mean free path for the different pressure present in the setup. Temperature was assumed to be 25° C and a radius of 28 pm [142] for He.

	Ambient	Ablation region		Ion Funnel	Mass spectrometer
	1013 mbar	80 mbar	20 mbar	3 mbar	10^{-7} mbar
Mean free path (m)	1.2×10^{-5}	1.5×10^{-4}	6×10^{-4}	4×10^{-3}	1.2×10^{4}

1.8   THE ION FUNNEL

In its initial configuration, the ion funnel was proposed by Shaffer et al. [143], who successfully used it to increase ion transmission in electrospray ionization mass spectrometry (ESI-MS). It consists of a series of stacked ring electrodes with decreasing diameter towards the mass spectrometer orifice. Radiofrequency (RF) voltage is applied to the ring electrodes at opposite phase between adjacent electrodes. Such an arrangement creates a repulsive, quasi-stationary potential (i.e. effective potential [144]) in the radial direction that confines ions near the funnel axis. Transiting the funnel, the ions experience both the effective potential near the electrodes' inner surfaces and collisions with a buffer gas. In order to compensate for the ions' axial energy loss, an axial DC field was initially used to accelerate ions towards the funnel exit. [145] It was shown to improve the transmission of ions when installed in the intermediate pressure region before the mass analyzer [146] . Matching the effective potential for a broad mass to charge (m/Q) range and lowering their kinetic energy by collisions can efficiently contain the ions within the inner volume in a similar way to multipole ion guides. Nevertheless, ion funnel geometry and operating conditions influence the quasi-stationary potential that can lead to a mass to charge dependent ion transmission. The presence of axial potential wells (trapping potential [145, 147, 148]) particularly at the smaller apertures near the end of the funnel and RF-heating can also cause such m/Q dependent transmission. For a fixed geometry the effective potential (V_{eff}) and depth of a trapping "well" (V_{trap}) are proportional to amplitude and frequency of the RF field:

$$V_{eff}, V_{trap} \propto \frac{Q}{m} \cdot \frac{E_{rf}^2}{\omega^2} \tag{1.8}$$

where E_{rf} is the amplitude (peak to peak) of the applied electric field and ω its angular frequency [81, 147, 149] . For ion transmission through the ion funnel the repulsive effective potential should be higher than the radial kinetic energy vector of an ion while the trapping well should remain smaller than the ions' axial kinetic energy. It follows therefore that ions with higher m/Q require a higher effective potential to be transmitted, while the lower m/Q ions might already get trapped in the potential wells between the electrodes. [81, 146, 150]. Depending on the amplitude and the frequency applied to the funnel it is possible that the conditions for adiabaticity [144] are not met, causing the ions to be excited and eventually lost through RF heating. The transmission of low m/Q ions is reduced when the RF frequency is decreased [81], RF amplitude is increased [146] and, as in a quadrupole trap, when the buffer gas pressure is increased [42]. In this study we investigated another approach proposed in [151] for improving ion transmission in a LAMS setup, which makes use of a convergent-divergent (CD) nozzle upstream an RF-only ion funnel. In the here presented instrument a DC gradient along the funnel axis is omitted and the transmission trough the funnel relies solely on the gas dynamic inside the funnel. Thereby the construction and RF-feed to the funnel can be vastly simplified, as only one lead per phase is required to drive the opposite polarities of the electrodes.

1.9   CD NOZZLE

The nozzle used is a convergent-divergent (CD) nozzle (or de Laval nozzle) which can be described as a pinched tube, having an asymmetric hourglass shape (Fig. 1.11). A short description of the properties of a CD nozzle based on [152] is given in the following.
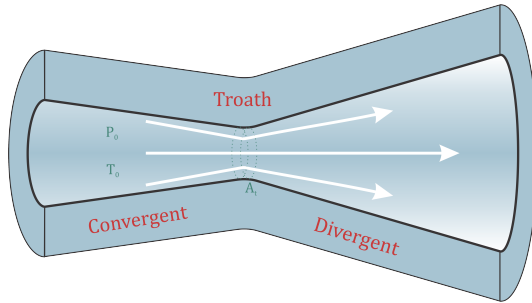
FIGURE 1.11: Schematic of a CD-nozzle. In white the gas flow direction

An isentropic, reversible (frictionless and without dissipative losses), adiabatic (no heat exchange) and compressible gas flow is considered. The gas is in a steady-state and flows symmetrically along a straight line from the inlet to the exit. The flow is directly linked to the dimensionless Mach number, defined as the ratio between the speed of the fluid (u) of and speed of the sound (c). The speed of sound is related to fluid properties such as the density and heat capacity:

$$M = \frac{u}{c} = \frac{u}{\sqrt{\gamma T R}} \tag{1.9}$$

Where R is the specific gas constant, T the temperature in the fluid and γ is the ratio of specific heat capacities:

$$\gamma = \frac{c_p}{c_v} \tag{1.10}$$

c_p and c_V are the specific heat capacities at constant pressure and at constant volume, respectively. When the Mach number is less than one, the flow is in the subsonic regime, for M=1 the regime is sonic, and for M>1 it is supersonic. A CD nozzle is characterized by three regimes: subsonic upstream, sonic within and supersonic downstream the throat. In the nozzle

the speed in the first part increases because the diameter decreases while flow rate is conserved. At sufficient pressure (i.e. flow rate) upstream the nozzle, the flow becomes sonic at the throat. This is a condition called choked flow and the mass flow rate ($\dot{m}_{chocked}$) can be derived from:

$$\dot{m}_{chocked} = \rho \cdot pu \cdot pA \underset{M=1}{\rightarrow} A_t p_0 \sqrt{\frac{k}{R_s T_0}} \left(\frac{2}{\gamma+1}\right)^{(\gamma+1)/(\gamma-1)} \qquad (1.11)$$

Where ρ is the density of the gas, A_t the throat area and p_0 and T_0 are the upstream pressure and temperature of the gas, respectively. It is interesting to note that, for a given gas, the maximum flow rate of a chocked orifice depends only on its size (A_t) and the conditions upstream. After the nozzle throat, the gas flow can either reach the subsonic or supersonic flow regime, depending on the pressure downstream the nozzle. When the pressure is low enough after the throat, the gas expansion in the divergent part of the nozzle will increase the gas velocity. The gas jet resulting is therefore influenced by the pressure in the divergent section. How the pressure in the divergent section influence the gas jets properties can be seen in figure 1.12. A CD- nozzle exhibits choke properties at the throat if the pressure and mass flow through the nozzle is sufficiently high to reach sonic speeds. If this is not the case, no supersonic expansion is achieved, and the CD-nozzle will act as a Venturi tube.
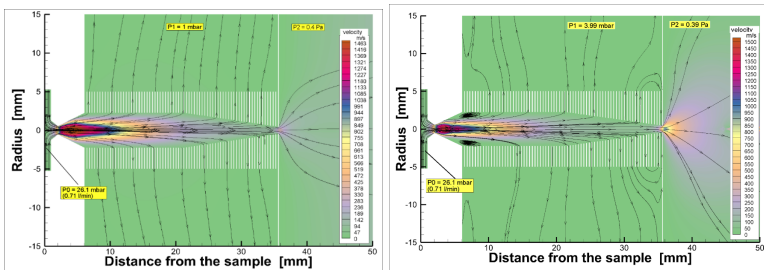
FIGURE 1.12: Simulated gas velocity for different pressure regimes before and after CD-nozzle of the developed instrument. The simulations were performed by Prof. V. Varentsov. The pressure in the ablation region is constant (26 mbar) and varied the pressure in the ion funnel region (1mbar *left*, 4 mbar *right*). It can be seen that different gas jets are formed.

1.10 TIME-OF-FLIGHT MASS SPECTROMETRY (TOFMS)

Principally any type of mass analyzer could be coupled with a pulsed laser ion source. High transmission efficiency together with a large dynamic range and simultaneous ion detection are beneficial to effectively measure the ion signals from a single ablation event. A few examples of laser ion sources coupled with a sector-field mass spectrometers have appeared in the literature at the advent of LAMS, using, for example, the double-focusing Mattauch-Herzog sector field geometry with simultaneous ion detection [153]. However, the development of modern fast detection electronics has made time-of-flight mass spectrometry (TOFMS) appealing. In TOFMS (Fig. 1.13), an ion's mass-to-charge ratio is determined via an accurate time measurement. [154]
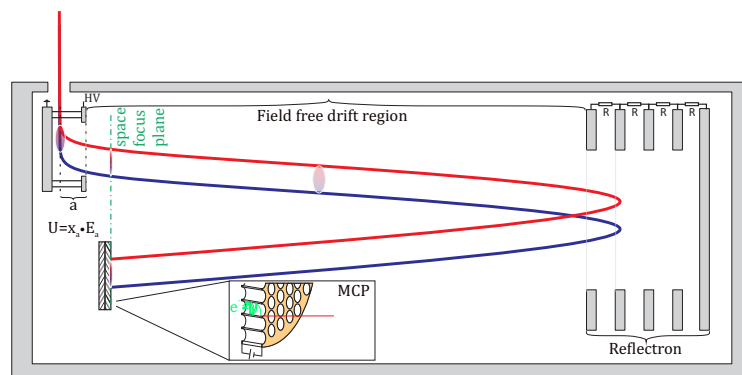
FIGURE 1.13: Schematic of a time of flight mass analyzer with orthogonal extraction. The ions are accelerated to identical (in the ideal case) energy by a pulsed electric field. Then the ions travel a constant distance and reach the detector accordingly to the m/Q ratio. Multichannel plates are commonly used as detector. When ions reach the surface of the plates, they initiate electron avalanches inside the MCP channels, resulting in a measurable current, which is proportional to the initial ion current.

A population of ions experience an acceleration by an electric field of known strength. The ions' potential energy given by the electric field is converted in kinetic energy following:

$$E_p = zqU \tag{1.12}$$

$$E_k = \frac{1}{2}mV^2 \tag{1.13}$$

$$E_p = E_k \Rightarrow v = \sqrt{\frac{2QU}{m}} \tag{1.14}$$

where E_p and E_K are the potential and kinetic energy respectively, Q is the species charge, U is the electric potential across which the ion is accelerated, v is the final velocity of the particle, and m is the mass of the particle. In the ideal case, the kinetic energy of all the ions is only due to Coulomb forces and therefore their velocities after the electrostatic acceleration will be inversely proportional to the square root of their mass/charge ratios. Ions traveling the same distance, but with different velocities, will arrive at different times. Knowing that the distance (d) divided by time t is equal to the velocity v, the flight time can be expressed as function of mass to charge:

$$t = k\sqrt{\frac{m}{Q}} \quad \Leftrightarrow \quad \frac{m}{Q} = \frac{t^2}{k^2}; \qquad k = \frac{d}{\sqrt{2Uq}} \tag{1.15}$$

It is therefore possible to obtain a mass to charge spectrum recording the flight time. However, in real cases, the mass resolving power and the mass accuracy of the TOF mass analyzer are mainly influenced by different factors:

- Initial kinetic energy distribution of the ions.

- Initial spatial distribution of the ions.

- Experimental factors:
    - Jitter in timing circuitry.
    - Detector rise/fall time.
    - Temporal resolution of data acquisition system.

It is possible to minimize the errors arising from the ion population properties using different strategies. To correct for the difference in kinetic energy of the ions it is preferable the extract the ions along the direction where their energy spread is smallest (orthogonal extraction) [155]. To compensate for the ions' initial position (a in figure 1.13) in the extraction region, the detector can be positioned in the space focus plane, which is the distance where faster-moving ions (initially located closer to repeller) overtake slower-moving counterparts [156]. The space focus plane position is m/Q-independent, albeit different m/Q arrive at different times. When

only one electric field is employed for the extraction of the ions, the space focus plane's is positioned fairly close to the extraction region, and poor resolution is to be expected. To correct for this effect, increasing the flight time and compensate the energy spread of ions with the same starting position, a reflectron can be used. Firstly developed by Mamyrin et al. [157]; the reflectron can compensate for the position dependent energy spread by introducing an energy-dependent elongation of the flight path and creates a "mirror" space focus plane. A single-stage reflectron exposes the ions to a potential gradient along the flight trajectories. The ions will penetrate into the potential gradient according to their kinetic energy, before being reflected. The penetration depth increases linearly with energy, and since the ion with higher energy will travel a longer path it is possible to obtain a narrow arrival distribution for the ions with the same mass/charge at the detector, placed in the second space focal plane. For a more extensive theoretical explanation the reader is referred to [158–161]. On the other hand, the experimental factors are inherently hardware specific and therefore dependent on technology advancements in electronics and detector design.

Many of today's TOFMS use a MCP detector systems due to their fast response times and high amplification of the incoming signal. Once one ion reaches the detector, it starts a cascade of secondary electrons, producing an electron cloud that produces a detectable current at an anode. The generated current can then be amplified and converted to digital signal using a fast analog to digital converter (ADC). The produced output signal can be described by a Pulse-Height Distribution (PHD) (Fig. 1.14 dotted red line) which is characteristic of given MCP detector setting. In order to relate the voltage to a physical number of ions, a calibration factor called Single-Ion Signal (SIS) is used (Fig. 1.14) . For Further information the reader is refereed to reference [162].
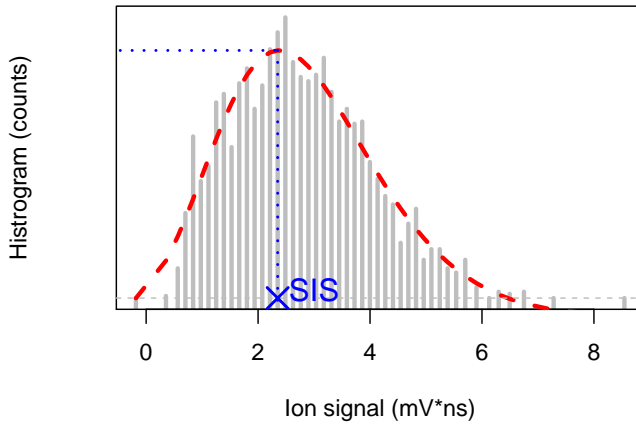
FIGURE 1.14: MCP-response to low frequency ion detection. The current produced after ion impact in MCP can be described using PHD (dotted red line). Characterizing this distribution allows for SIS estimation and therefore counts conversion

2

AN RF-ONLY ION FUNNEL FOR COOLING IONS FROM LASER ABLATION

This chapter has in part been published as *"An RF-only Ion Funnel Interface for ion cooling in Laser Ablation Time of Flight Mass spectrometry."*
Authors: Lorenzo Querci; Victor Varentsov; Detlef Günther; Bodo Hattendorf

2.1 INSTRUMENT DESCRIPTION

The prototype of the "LAFUMA" was realized by coupling an available time-of-flight (TOF) mass analyzer [163, 164] to a custom built ion optic and a nozzle-funnel setup [165] as shown in figure 1. This specific configuration was conceived primarily because the laser beam must be guided through the ion funnel and CD nozzle to achieve ablation of the sample. Additionally, it provides a second expansion stage, to reduce the flow of buffer gas into the mass spectrometer. Thereby low operating pressure and higher abundance sensitivity can be attained.
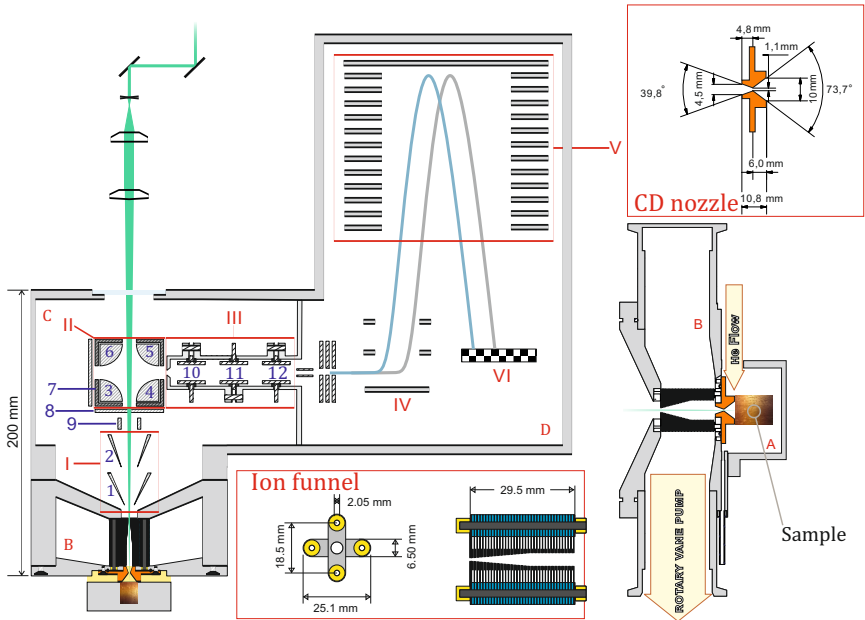
FIGURE 2.1: (I) Extraction cones, (II) Quadrupole deflector, (III) Einzel lens, (IV) Extraction lens, (V) Reflectron, (VI) MCP detector. Pressure stages: (A) ablation region, (B) funnel chamber, 3 mbar, (C) ion optic region, 10^{-4} mbar, (D) TOFMS, 10^{-6} mbar. Labels 1 to 12 indicate individual ion optics elements; further explanation can be found in the following sections. **Top-right**: Close-up and dimensions of the Convergent/Divergent (CD) nozzle. **Bottom right**: Details of the sample-nozzle-funnel arrangement.

Sample holder

The sample holder is shown in figure 2.2. Up to 5 samples can be placed in the sample revolver where they are fixated with screws. The sample holder is put into the evacuation chamber and held up towards the vacuum gate valve, which can be opened. The sample revolver can be pushed against the CD-nozzle, the distance between them is adjusted using a screw. Each hole in the revolver corresponds to a number on the display. The sample holder can then be rotated in between measurements to ablate different spots.
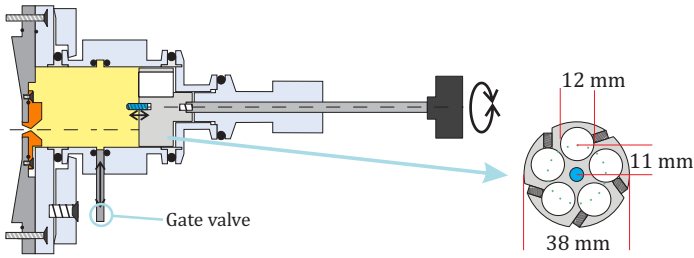
FIGURE 2.2: Schematic of the sample holder from above (left) and the front (right). Left the sample revolver (gray). The dotted green line represents position of the laser beam when the sample is rotated.

Pressure and gas dynamics

Helium was used as buffer gas because its high ionization energy should minimize charge exchange reactions with laser generated ions and the low mass reduces scattering losses during ion transfer. The gas flow fed into the ablation chamber directly affects the pressure. It was adjusted using a mass flow controller (1179A General Purpose, MKS instruments, 0-2 L/min N_2), calibrated for He against a bubble-flow meter (Debitmetre Numerique, Bioblock Scientific, Illkirch Cedex, France) to obtain the actual volumetric flow. The pressure inside the ion funnel was maintained with a rotary vane pump (UNO 065 D, Pfeiffer Vacuum, Asslar, De) equipped with a throttling valve for adjustment of the pump rate. The ion optics region pressure of $\approx 10^{-4}$ mbar was sustained by a turbomolecular pump (TMP 361, Leybold, De). Over the course of the initial experiments, different empirically designed, nozzles were tested resulting in a final nozzle featuring a throat diameter of 1.1 mm, a convergent throat of 73.7° and 6 mm length and a divergent cone of 37.8° and 4.8 mm length (see Fig. 2.1). With this geometry a buffer gas flow rate between 0.18 L/min and 1.78 L/min caused the pressure in the ablation region to vary between 8 mbar and 51 mbar.

The ion funnel

The funnel consisted of 74 electrodes made from 0.1 mm thick stainless steel plates with circular inner apertures. Electrodes of opposite phase are mounted in a crosswise pattern (Fig. 2.1 bottom) and separated by 0.7 mm spacers to achieve a 0.3 mm separation of the adjacent electrodes. The first
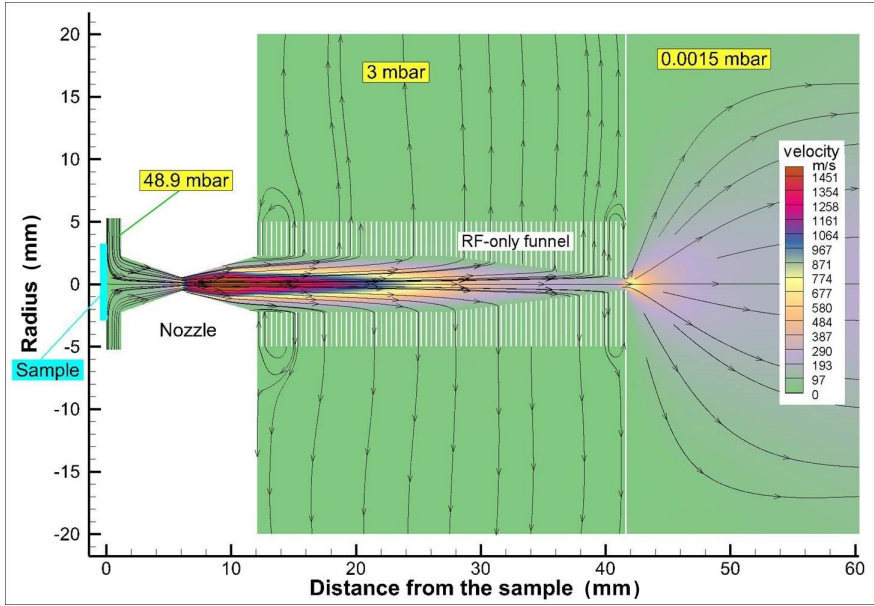
FIGURE 2.3: Calculated buffer gas velocity flow field for the RF only ion funnel with
           CD nozzle derived by numerical simulations for the initial experimen-
           tal configuration.

32 electrodes have an inner aperture of 4.5 mm, which then decreases lin-
early towards an exit aperture of 0.9 mm. RF power is supplied via a func-
tion generator (SFG 2110, GW Instek, TW), feeding a frequency and ampli-
tude adjustable sine wave to an R -power amplifier (Model 2100, ENI USA).
A 180° phase shift in the RF amplitudes at the ion funnel electrodes is ob-
tained from the secondary coil of a split-phase transformer. This configu-
ration allows sinusoidal RF frequencies between 0.1 and 5 MHz and am-
plitudes between 0 and 40 V_{pp} to be applied. Waveform and amplitude at
the electrode sets are monitored permanently via an oscilloscope(DPO4054,
Tektronix, USA).

Ion optics

The ion optics downstream the ion funnel used to steer the laser generated
ions to the mass spectrometer were developed in-house before the start of
this project. They consist of two conical primary extraction and focusing

lenses (I) and steering plates (9,8), followed by a quadrupole deflector lens (II) and an Einzel-lens arrangement (III) before the entrance to the commercial TOF mass analyzer, which remained unmodified. Potentials at the electrodes are supplied from a custom made power supply (12 channels, $0 - 350$ V) of switchable polarity. The voltages applied to the ion optic were empirically optimized aiming at higher transmission, the employed voltage can be seen in table 2.1.

TABLE 2.1: Typical ion optics settings used, numbering as in Fig. 2.1

	Cone 1	Cone 2	Deflector 3	Deflector 4	Deflector 5	Deflector 6	Housing 7	Z-Focus 8	Y-Focus 9	Einzel lens 10	Einzel lens 11	Einzel lens 12
Setting (V)	-4	-150	-70	-25	-5	-20	-3	+25	-2	-300	-40	-300

Mass analyzer and data acquisition

The mass spectrometer is a TOF (HTOF, Tofwerk AG Thun) with orthogonal ion extraction. It provided full spectrum readout at a frequency of 33 kHz. The detector is a multichannel plate (MCP, chevron configuration, active diameter 40 mm x 34 mm (special cut)) capable of delivering a signal output ranging from 0 to 300 mV. After 120 mV a nonlinear response of the detector was observed. Signal acquisition was triggered using the "Q-switch out" signal of the laser. After each trigger event a sequence of 150 individual waveforms or spectra was collected for each laser pulse through an ADQ1600RF 14-bit digitizer (SP Devices, Teknikringen, Se; sampling rate 1.6 GSPS, analog bandwidth 35Hz - 680MHz, spurious-free dynamic range 68 dB). This corresponds to a total sequence time of 4.69 ms, covering the entire transient ion signal generated by one laser pulse. Mass channels of a width between 0.003 Da (^1H) and 0.318 Da (^{238}U) with an average of 0.262 Da according to the ions' TOFs were defined and integrated by the TOFDaq software (Tofwerk, Thun, CH). The respective transient signals (see e.g. Fig. 2.5) were evaluated for each experiment.

Laser

In this initial study a frequency doubled Nd:YAG laser (Minilite, Continuum, San Jose, USA; central wavelength of 532 nm, pulse duration of 3

ns) was used for ablation. For the experiments described here a power of 7.6×10^5 W (24 J/cm^2 for an 110 μm spot diameter, 8×10^9 W/cm^2) was applied. The optical setup consisted of a set of two steering mirrors, a beam expander (6x magnification) and a final focusing lens (f-250 mm, best form), positioned before the entrance window of the ion optics chamber.

2.1.1 *Materials*

Two certified brass alloy standards (MBH B22 and B26) was used to evaluate the influence of instrumental operating conditions on ion transmission. The certified elemental composition of the two brass alloy standards are summarized in table 2.2 and table 2.3. Modifications of the instrument were necessary to compare laser ablation using the nozzle-funnel interface and in high vacuum. Therefore, a brass disk was fixed at the position of the ion funnel exit. The elemental composition of this brass disk was characterized with conventional LA-ICPMS and the results of this analysis are summarized in table 2.4.

TABLE 2.2: Certified mass fractions of standard reference material, MBH 22

Element	Al	Ni	Zn	Cu	As	Cd	Sn	Pb
Weight%	0.0402	0.154	15.92	82.47	0.165	0.0117	0.16	0.152
Uncertainty	0.0011	0.003	0.13	0.12	0.003	0.0006	0.004	0.004
Element	Bi							
Weight%	0.17							
Uncertainty	0.01							

TABLE 2.3: Certified mass fractions of standard reference material, MBH 26

Element	Al	Ni	Zn	Cu	As	Cd	Sn	Pb
Weight%	1.005	1.397	30.3	62.93	0.126	0.0147	1.476	0.93
Uncertainty	0.007	0.009	0.13	0.16	0.002	0.0007	0.015	0.009
Element	Bi							
Mass%	0.106							
Uncertainty	0.002							

TABLE 2.4: Mass fraction in an in-house brass disk employed. Data obtained with conventional LA-ICPMS using MBH26 as external standard, given are the mean of 3 measurements and, as uncertainty, the corresponding standard deviation.

Element	Al	Ni	Zn	Cu	As	Cd
Mass%	<0.0003	0.056	38.3	60	< 0.000146	0.11
Uncertainty	-	(0.0004)	(0.4)	(0.5)	-	(0.003)
Element	Sn	Pb	Bi			
Mass%	0.1	2.14	<0.0000034			
Uncertainty	(0.002)	(0.16)	-			

2.2 RESULTS AND DISCUSSION

The first characterization of the system was performed using a ns. The operating parameters (ion optics parameters, RF amplitude, RF frequency, pressure in ablation region, pressure in funnel region and TOFMS' parameter, laser focus position and laser energy) were optimized in order to achieve the highest ion transmission. To assess how a specific optimization of the source affects the relative ion detection and therefore the analytical precision of the setup, a series of parameter studies was carried out to characterize ion transmission through the nozzle-funnel arrangement. Since no precise sample movement was possible, measurements were carried out by continuous ablation on a single spot. The effects observed in these experiments were therefore a convolution of parameter changes and crater formation.

2.2.1 Laser drilling

To assess the influence of the crater formation and the feasibility of parametric studies during crater formation, 10'000 laser pulses were applied on brass sample (MBH22) and the evolution of the signal as the crater is forming was investigated. The averaged transient signal obtained from 300 laser pulses in dependence on number of laser pulses, and therefore crater formation, can be found in figure 2.4. It can be seen that the continuous ablation lead to a steady decrease in ion signal intensities (Fig. 2.4), which was very pronounced for approximately the first 1800 pulses, where the signals dropped by up to one order of magnitude. Afterwards a relatively

moderate decrease in ion signals was observed (50% during 8000 pulses) and this regime was considered sufficiently stable to investigate the influence of operating conditions on ion transmission. The initial signal drop is attributed to the deepening of the ablation crater (depth after 10'000 pulses approximately 73 μm) and thereby increasing loss of evaporated material to the crater wall. As the depth/diameter ratio increased, progressively fewer ions reached the crater mouth and could be sampled through the nozzle. After 1500 pulses a critical aspect ratio appeared to be reached and the fraction of material left inside the ablation crater remained constant. A second factor that could have been responsible for the signal loss is the continuous reduction of fluence on the developing crater walls.
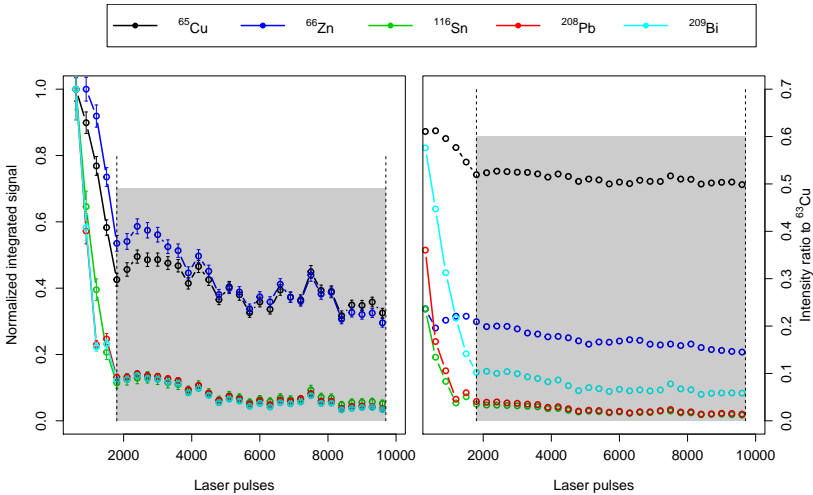
FIGURE 2.4: *Left:* Averaged integrated transient signals for different isotopes during single spot LAMSof sample MBH B22. Ion signals are normalized to their respective maxima. *Right:* Intensity ratios relative to the $^{63}Cu^+$ signal; the ratio of $^{116}Sn^+$ is multiplied by 50 for better visualization. Each data point represents the average of 300 laser pulses. Gas flow rate: 1.36 L/min, RF frequency 2.6 MHz RF amplitude 20 V_{pp}, ion funnel pressure: 3 mbar

The magnitude of the signal decrease during the first laser pulses appeared to be dependent on the element (Fig. 2.4 left) and even differed for the isotopes of Cu (Fig. 2.4 right). On closer inspection of the mass spectra it was found that ion signals of the main isotope of the matrix elements Cu

and Zn were above the dynamic range of the detection system. The initial signal intensities were thus severely underestimated, making their drop to appear less pronounced. This also explains the trend in the $^{65}Cu^+/^{63}Cu^+$ intensity ratio which also decreased during the first 2000 laser pulse (Fig. 2.4, right), because the less abundant ^{65}Cu was less affected by detector linearity. On the other hand, the elements present with lower mass fraction (Sn /Bi / Pb) were always within the dynamic range and the profiles thus represent the actual decrease in ion density at the ablation site. After the 2000 pulses, however, the measured intensity ratio approached the natural abundance of Cu indicating that detector saturation was not as significant anymore. It was not possible to limit the total ion currents to within the detector range for the first pulses because of the large spot obtained employing the laser system and optical arrangement.

2.2.2 *Parameter studies*

Gas flow rate

During initial tests, the optimum pressure inside the funnel region was found to be 3 mbar, which was afterwards kept constant by adjusting the pumping rate to the changes in mass-flow to the ablation region. With a fixed pressure in the ion funnel chamber, the pressure in the ablation region was found to increase linearly with the He flow rate. A higher pressure would reduce the initial expansion of the ablation plume and cool the ions. At the same time, it increases the velocity of the ion cloud after expansion through the CD nozzle. While maintaining constant conditions downstream the nozzle (RF: 2.5 MHz, 20 V_{pp}; 3 mbar in funnel) the impact of the flow rate on the transmission was investigated. As illustrated in figure 2.5, the average transient profile of the ion signals became shorter with increasing He flow rate (Fig. 2.6 insert), whilst the integrated ion signals increased exponentially (Fig. 2.5 insert). Apart from $^{65}Cu^+$, the ion signals of different isotopes showed a increase of similar magnitude, indicating that the composition of the ion beam is not significantly affected by the flow rate applied. This is most likely resulting from the compression of the ion cloud, which at the same time reduces the signal width and, by confining the ion cloud more densely, also improves the overall transmission. The smaller relative increase observed for $^{65}Cu^+$ on the other hand most likely is again caused by the signal approaching detector saturation. Additional loss may however also be caused by an increase in cluster ion formation with increasing pressure (see section molecular ion formation 2.2.2).
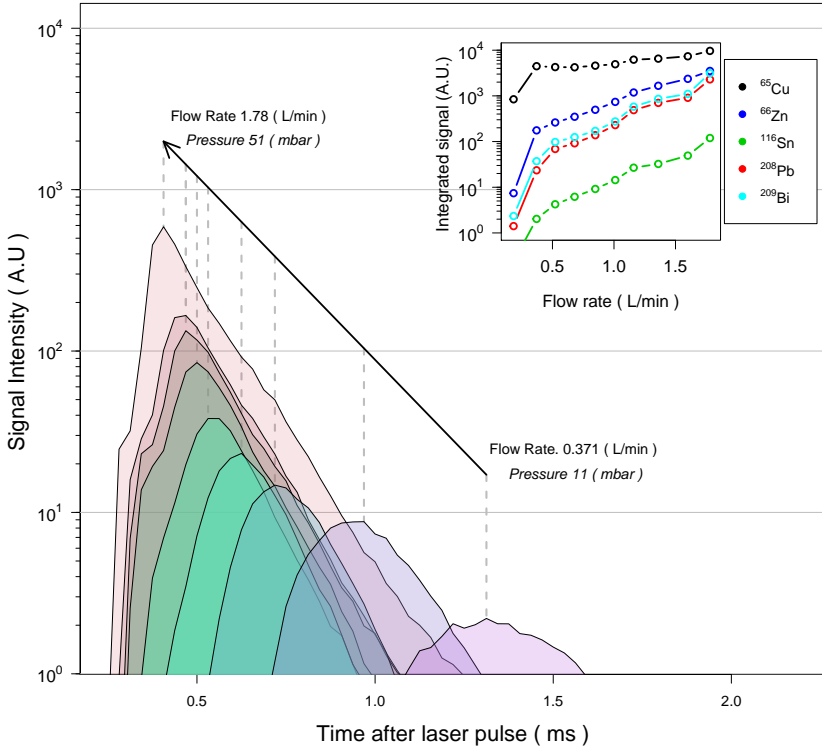
FIGURE 2.5: Average transient signals for ^{209}Bi for Helium flow rates ranging from
0.18 to 1.78 L/min. 0.18 L/min data are too low to be visible in the
transient profiles. The insert shows the integrated signal intensity in
dependence on the helium flow rate for different atomic ions. All data
represent an average of 300 laser pulses.

As can also be seen in figure 2.6, an increase in buffer gas flow rate was
causing an earlier arrival of the ion cloud in the MS after the laser pulse.
The delay between laser pulse and the transient peaks' maxima, as well as
the signal durations (Fig. 2.6 insert), were found to decrease steeply with
increasing flow rate until a value of ≈ 0.5 L/min was reached, after which
only a moderate decrease was observed (Fig. 2.6).
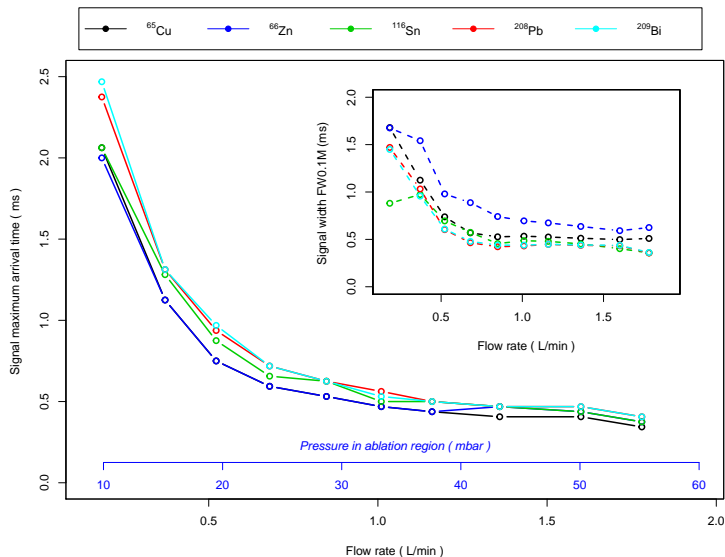
FIGURE 2.6: The delay between laser pulse and the transient peaks' maxima in dependence on the helium flow rate. In the top-right panel the full width at 10% maximum (FW0.1M) is plotted against the He flow rate. Ion signals represent an average of 300 laser pulses.

Figure 2.6 indicates a mass dependency in arrival times on the applied gas flow rate. The heavier ions appeared to arrive later in the MS than lighter ones. This may indicate the presence of isoenergetic ions, due to their acceleration in the ion optics. The inverse of arrival time was however not found to be proportional to the square root of the different m/Q. This finding may be related to an isokinetic acceleration in the ion optic region given by the residual gas expansion or the insufficient time resolution of the data acquisition. The signal durations on the other hand showed a tendency towards shorter signals for higher m/Q at all gas flow rates.

RF parameters of the ion funnel

As visible in figure 2.7, transmission of the different m/Q through the ion funnel was affected differently by RF amplitude, RF frequency and gas flow rate.
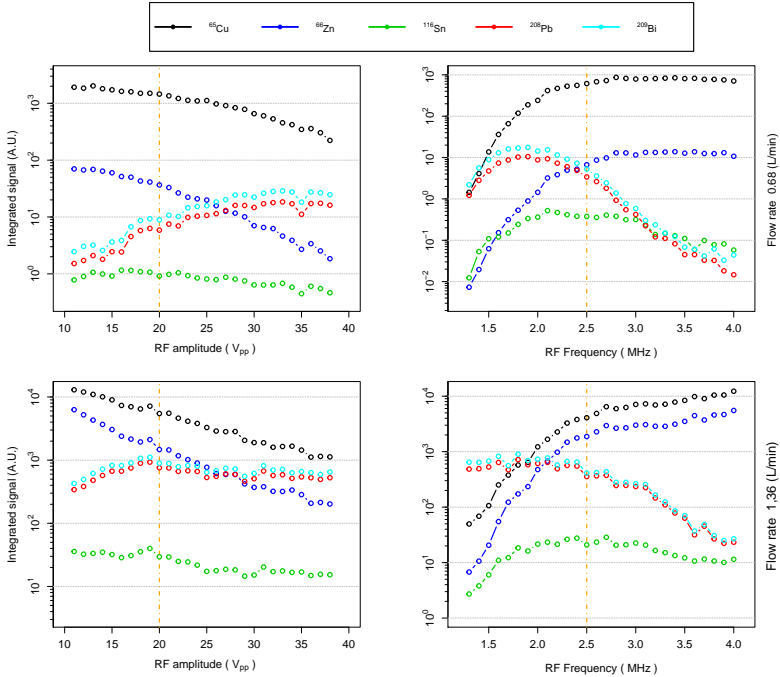
FIGURE 2.7: *Left:* Integrated signal intensities of the main components plotted against the applied RF amplitude (constant RF frequency 2.5 MHz). *Right:* Integrated signal intensities of the main components plotted against the applied RF Frequency (constant RF amplitude 20 V$_{pp}$). *Top:* constant flow rate of 0.68 L/min. *Bottom:* constant flow rate of 1.36 L/min. The yellow line indicates, which parameters were selected as default parameters for further experiments. Ion signals represent an average of 300 laser pulses.

The signal of lighter ions (Cu, Zn) steadily decreased when increasing amplitude from 11 V to 38 V, while high m/Q signal either increased monotonically (low gas flow rate) or reached a plateau (high gas flow rate).

Intermediate m/Q (e.g. Sn) showed correspondingly intermediate trends. Increasing the RF frequency from 1.3 MHz to 4 MHz on the other hand lead to more pronounced changes with opposite trends for the different m/Q. Lighter ions were found to reach a plateau (low gas flow rate) or steadily increase (higher gas flow rate) while the heavier ones showed an intermediate maximum (low gas flow rate) or suppression from an initial plateau (high gas flow rate). These results seem to indicate that the general trend in transmission through the ion funnel is not greatly dependent on the initial conditions in the ablation region. Higher ion signals are observed for higher gas flow rates or pressures but the dependence of transmission on frequency or amplitude is very similar. The major difference occurs in the slopes of the respective dependencies. For the higher gas flow rate the increase or suppression of the ion signals appeared to be less pronounced than at low flow rate. Also the onset of the plateau appeared to be at lower amplitude or higher frequency respectively when increasing the gas flow rate, which would indicate that lower effective and trapping potentials are required at higher gas flow rate. The mass dependency of ion transmission on the other hand is related to a combination of effective and trapping fields as well as RF heating. Transmission of higher m/Q requires a higher effective potential for the confinement of ions inside the funnel (i.e. lower frequency and/or higher amplitude). In the case of lower m/Q ions the transmission gets adversely affected by RF heating and trapping in the potential wells, which reduces their intensities. To investigate this more in detail, the ions' signals were plotted against E_{rf}^2/ω^2, which is directly proportional to V_{eff} (figure 2.8). A correlation between m/Q and the effective potential can be seen. It is interesting to notice that, in the plotted range, different signal decrease for the same species were found when the applied effective potential was varied changing either RF frequency or amplitude. Two order of magnitude signal decrease was found for the lighter species when the RF frequency was changed, whereas only one when the amplitude was changed. The same trend (stronger variation in case of RF frequency changes) can be observed for the signal increase of heavier species. This indicates a stronger effect of RF frequency in the transmission capabilities of the RF only ion funnel. When plotting the ions signal against E_{rf}/ω^2, a greater similarity can be observed, as can be seen in figure 2.9. Looking at the plots it interesting to notice the very similar signal evolution for the same interval plotted. This finding was not expected from the theory of a conventional ion funnel (section 1.8) and need further investigation.
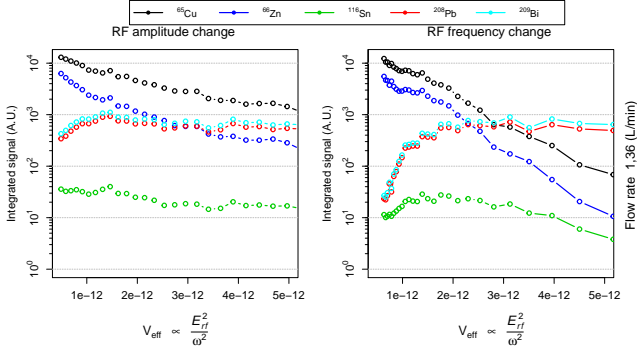
FIGURE 2.8: *Left:* Integrated signal intensities of the main components plotted against E_{rf}^2/ω^2 obtained while changing the applied RF amplitude (constant flow rate of 1.36 L/min, and constant RF frequency 2.5 MHz). *Right:* Integrated signal intensities of the main components plotted against E_{rf}^2/ω^2 obtained while changing the applied RF frequency (constant flow rate of 1.36 L/min, and constant RF amplitude 20 V_{pp}). Each point represent an average of 300 laser pulses.
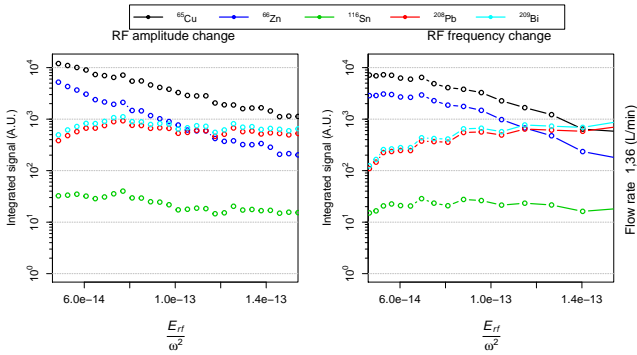
FIGURE 2.9: *Left:* Data from figure 2.8 plotted against $\frac{V_{rf}}{\omega^2}$ obtained changing the applied RF amplitude (constant flow rate of 1.36 L/min, and constant RF frequency 2.5 MHz).

Right: Integrated signal intensities of the main components plotted $\frac{V_{rf}}{\omega^2}$ obtained changing the applied Frequency (constant flow rate of 1.36 L/min, and constant RF amplitude 20 V_{pp}).

RF frequency

It was also observed that varying the RF frequency affected the shape of the transient signals of different m/Q differently (Fig. 2.10).
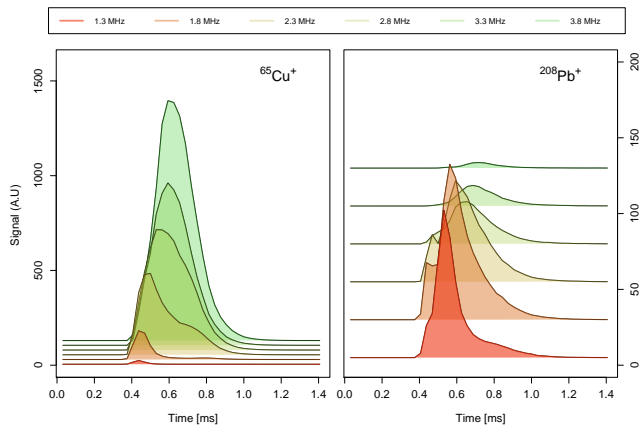
FIGURE 2.10: Examples of the transient signals observed for ^{65}Cu and ^{208}Pb at different RF frequencies, ranging from 1.3 to 3.8 MHz for a constant flow rate and RF amplitude of 1.36 L/min and 20 V$_{pp}$ respectively. For the sake of clarity, the baselines were shifted on the y-axis by 25 A.U. Ion signals represent an average of 300 laser pulses.

At the highest applied frequency, the peak for Cu$^+$ appeared almost symmetrical while lowering the frequency lead to a progressive truncation of the peak tail. High m/Q ions on the other hand were found to exhibit a similar truncation in the peak front when the frequency was increased. From the position of the peak respective maxima it appears as if a fraction of Cu$^+$ ions was suppressed when the Pb$^+$ intensity was the highest and vice versa. This is currently considered to be a result of a convolution of the transmission characteristics of the ion funnel and space charge effects, where high currents of high m/Q ions cause suppression of low m/Q (Fig. 2.11).
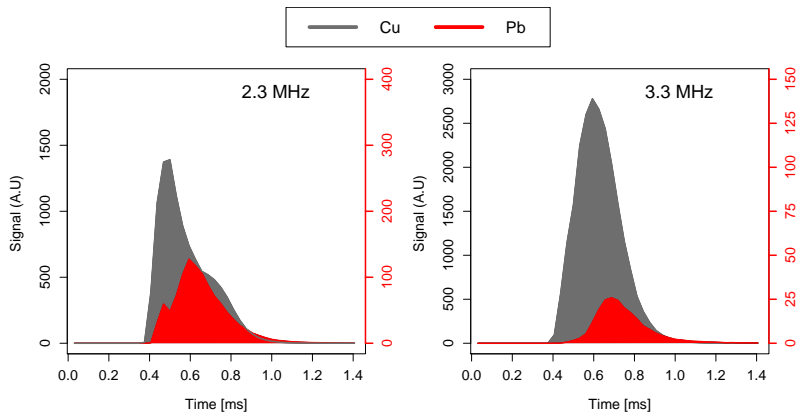
FIGURE 2.11: Examples of the transient signals observed for ^{65}Cu (black) and ^{208}Pb (red) at different RF frequencies.

Molecular ion formation

The presence of molecular and cluster ions in LAMS spectra is well known and can be a severe limitation for quantitative analyses when not separable from the target isotopes [166] . Their abundances are usually depending on the sample material and on the conditions used for ablation. The spectra obtained during these studies also showed significant levels of polyatomic ions, which could be partly resolved from atomic ions (see e.g. Fig. 2.13). For the brass samples analyzed in this work, we tentatively assigned the most abundant species to either Cu or Zn cluster ions (e.g. Cu^{2+}) or adducts of water to atomic ions and clusters. Figure 2.12 showcases the relative abundances of selected Cu-based ($^{65}Cu(H_2O)^+$, $^{63}Cu(H_2O)_2^+$, $^{63}Cu_2^+$ and $^{65}Cu_2(H_2O)_3^+$) species in dependence on operating conditions and ablation duration. In particular, the abundance of the metal cluster ions was strongly affected by the gas flow rate applied to the source (Fig. 2.12), indicating that they were more readily formed in higher pressure ablation conditions. It can also be seen that the intensity ratio of water adduct ions relative to the parent ion is relatively stable, indicating that the reaction rates do not change significantly with pressure in the source. There is furthermore only little variation in the abundance of water related clusters during single spot ablation, while the metal cluster ions occurred at lower abundance after approximately 2000 laser pulses. The dependencies on the

ion funnel operating conditions were found generally similar to those of
atomic ions of similar m/Q. High RF frequency and low RF amplitude re-
duce the transmission of cluster, as has been seen previously for high m/Q
ions such as Pb^+ or Bi^+.
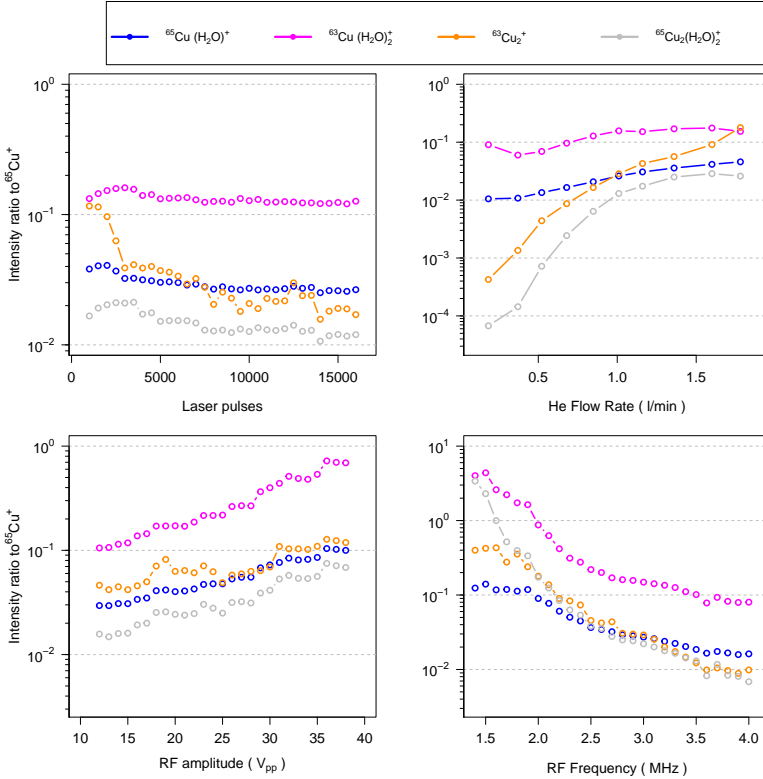
FIGURE 2.12: Intensity ratios of molecular ions relative to $^{65}Cu^+$ in dependence on
operating conditions. All the experiment where carried out using a
starting parameter set of 2.5 MHz, 20 V_{pp}, 1,36 L/min: for each exper-
iment one parameter was changed while the others remained constant.
Ion signals represent an average of 300 laser pulses.

Time resolved signal evolution.

The time resolution provided by the TOFMS also allows monitoring the evolution of different species across the transient signal. As an example shown in Figure 2.13 it was possible to distinguish periods of the transient signal where the relative abundances of water adduct ions differed substantially. The molecular ions, which occur in the proximity of the Sn atomic ions (tentatively assigned to $Cu(H_2O)_3^+$ and $Zn(H_2O)_3^+$) had significantly higher abundances in the later part of the transient signal than in the beginning. It is currently not clear why the relative abundance of the water adduct ions changes during the evolution of the peak. It may however offer an opportunity for a relative straightforward discrimination between molecular and atomic ions in the mass spectra by adjusting the integration period. Again space charge effects due to heavier species are were found with closer inspection on how the transient signal of Zn is effected by abundant Pb ions (Fig 2.13).
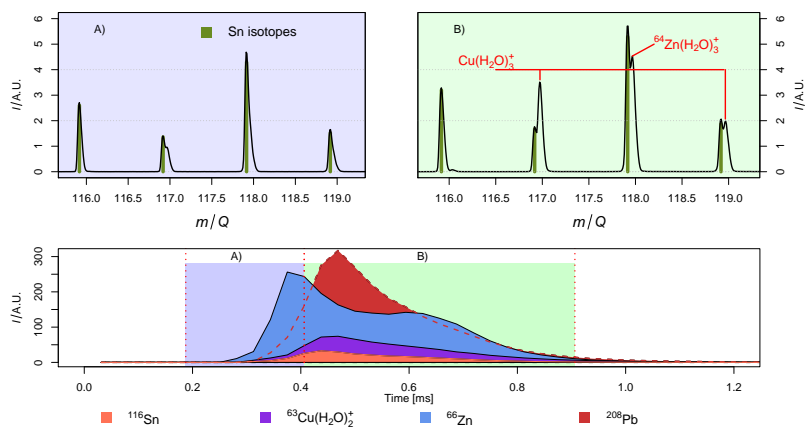
FIGURE 2.13: Mass spectra between m/Q 116 and 119 for different periods of the transient peaks. The *top left panel* shows the average spectrum between 0.2 and 0.4 ms ("faster ions"), the *top right panel* displays the average spectrum between 0.4 and 0.9 ms ("slower ions"). Green bars in the spectra indicate the natural abundance of Sn, based on the signal at m/Q 116. In the *bottom panel* is presented the averaged transient signal. Mass spectra represent an average of 500 laser pulses.

2.2.3   *Quantitative analyses of different brass samples*

Different operating conditions were chosen, which corresponded to highest transmission of either high, intermediate or low m/Q (see Tab. 2.5). Prior to each experiment a set of 2000 laser pulses where applied as preablation routine. Then 500 laser pulses were applied to the pretreated sample surface and the ion signal intensities were recorded and averaged. To compare the system response, relative sensitivity coefficients (RSC), defined as the ratio between the sensitivities of a target isotope and of a reference isotope, were calculated for the brass reference materials. Because of its high abundance and supposedly homogeneous distribution in both samples $^{65}Cu^+$ was chosen as the reference isotope.

The agreement of the RSCs for both reference materials was moderate for the experimental conditions studied (Tab.2.5). Remarkable differences were found mostly for low m/Q species (Al^+), where the standard with higher mass fraction of heavy elements (BH26) shows lower RSC for lighter elements. Their absolute values however were found to always significantly differ from 1 even for isotopes close in m/Q. It was to some extent caused by the laser source used (3 ns), which is known to cause severe inter-element fractionation effects. This makes matrix matching essential for reliable quantification. In addition to that, the funnel operating conditions strongly affected the transmission across the mass range studied and consequently the absolute values of the RSCs. When low RF frequency was applied (High a), the spectra were dominated by high m/Q isotopes resulting in extreme RSC values. At the same time the transmission of molecular and cluster ions increased, leading to more abundant spectral interferences and an eventual overestimation of the sensitivity. Based on the mass spectra however, this contribution is estimated to be < 5% of the peak intensity for Pb or Bi in B22. High m/Q optimization at lower frequency and higher amplitude (High b) alleviated the mass discrimination inside the ion funnel to some extent but RSCs still differed by orders of magnitude. At intermediate settings (Intermediate a or b) more similar RCSs for the different isotopes were obtained. Operation at lower gas flow rate to reduce the abundance of molecular species lead to a significant drop in sensitivity and no remarkable change in absolute RSC apart from Pb and Bi. Lower gas flow rate however also leads to a lower relative standard deviation for the different isotopes and is most likely due to avoiding detector saturation with lower ion signals, especially for the reference isotope.

TABLE 2.5: RSCs and relative standard error (in brackets) obtained for the different brass reference materials at different operating conditions of the ion funnel and gas flow settings. *Intermediate a* (2.5 MHz, 20 V_{pp} 1.36 L/min) and *Intermediate b* (2.5 MHz, 20 V_{pp} 0.68 L/min): balanced transmission across m/Q range, *High a* (1 MHz, 20 V_{pp},1.36 L/min) and *High b* (2.5 MHz, 30 V_{pp}, 1.36 L/min): optimized for high m/Q, *Low a* (4 MHz, 20 V_{pp},1.36 L/min) and *Low b*(2.5 MHz, 10 V_{pp},1.36 L/min): optimized for low m/Q. Pressure in the ion funnel chamber was kept at 3 mbar.

		^{27}Al	^{58}Ni	^{66}Zn	^{75}As	^{113}Cd	^{116}Sn	^{208}Pb	^{209}Bi
Intermediate a	BH22	0.99	0.23	5.96	-	19.1	21.2	168	94.1
		16%	19%	2%		(19%)*	5%	(3%)*	(3%)*
	BH26	0.27	0.2	4.66	0.11	11.6	20.6	83.9	71.2
		8%	8%	2%	29%	(23%)*	3%	(3%)*	-3%
	BH22/MBH26	3.67	1.15	1.28	-	1.65	1.03	2	1.32
High a	BH22	-	-	-	-	-	-	6380	3949
								(13%)*	(13%)*
	BH26	-	-	0.95	-	-	-	4207	4226
				38%				(18%)*	(18%)*
	BH22/MBH26	-	-	-	-	-	-	1.52	0.93
Low a	BH22	10.42	0.33	5.58	0.02	2.49	4	11.8	6.47
		3%	7%	3%	23%	(27%)*	6%	(3%)*	3%
	BH26	3.8	0.32	4.47	0.04	2.8	4.94	7.86	6.28
		3%	4%	3%	22%	(27%)*	3%	(3%)*	(4%)*
	ratio	2.74	1.03	1.25	0.5	0.89	0.81	1.5	1.03
Low b	BH22	2.27	0.25	4.48	0.03	3.57	5.49	21.8	11.83
		7%	10%	3%	26%	(29%)*	6%	(3%)*	(3%)*
	BH26	0.79	0.26	4.37	0.05	3.48	7.28	16.4	13.23
		4%	5%	3%	25%	(29%)*	3%	(3%)*	(4%)*
	BH22/MBH26	2.87	0.96	1.09	0.6	1.03	0.75	1.33	0.89
High b	BH22	0.42	0.21	3.15	-	18.7	20.7	178	95.95
		32%	25%	2%		(26%)*	6%	(3%)*	(3%)*
	BH26	0.13	0.15	2.88	-	16.7	22.56	117	93.69
		15%	11%	3%		29%	3%	(3%)*	(3%)*
	BH22/MBH26	3.23	1.4	1.09	-	1.12	0.92	1.52	1.02
Intermediate b	BH22	0.02	0.33	0.44	0.04	1.4	1.5	7.03	4.3
		52%	11%	3%	24%	54%	12%	4%	4%
	BH26	0.01	0.28	0.47	0.02	0.87	2.46	5.59	5.01
		21%	5%	2%	33%	57%	4%	3%	4%
	BH22/MBH26	2	1.18	0.93	2	1.62	0.62	1.26	0.86

*Contribution from molecular ions detected in the mass spectrum.

2.2.4 *LAMS in high vacuum vs. nozzle-funnel interface*

The effect of the new source on transmission of the laser produced ions was estimated by comparing the ion signals with those obtaining when ablation took place in the high vacuum part of the instrument. Therefore, the ion funnel was replaced by a brass disk and ablation was carried out after adjusting the laser beam delivery to the new sample position and the ion optics to match the higher ion kinetic energies.
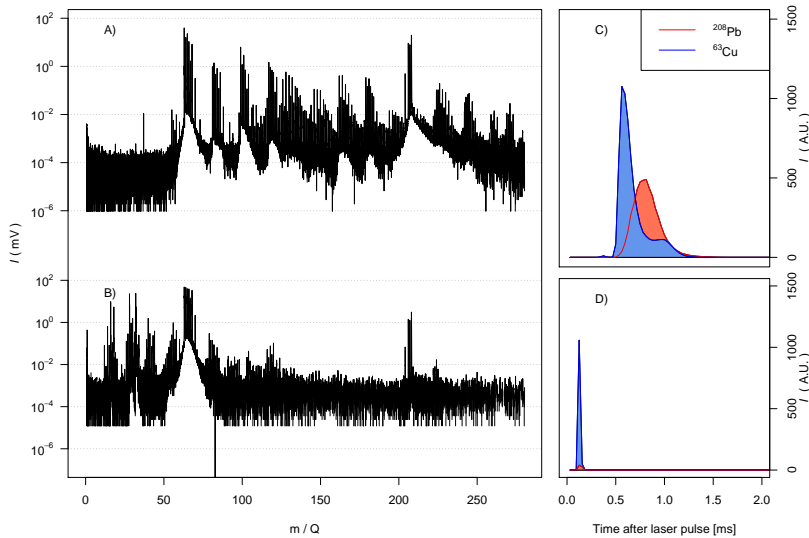
FIGURE 2.14: *A)* Mass spectra obtained using the LAFU source. Resulting from averaging of 500 transient signals in the region from 0.21 ms to 1.6 ms *B)* Ablation in high vacuum. Resulting from averaging of 500 transient signals in the region from 0.05 ms to 0.14 ms *C)* Averaged transient signal of $^{+63}Cu^{+}$ and $^{208}Pb^{+}$ the LAFU source using 2.5 MHz, 20 V_{pp} and 0.68 L/min and *D)* in high vacuum

500 laser pulses were applied and the signals were compared to those from ablation using LAFU source under identical ablation conditions. Figure 2.14 shows the difference in the resulting spectra and temporal profiles recorded with both settings. When the LAFU source is removed the transient signals transformed into a short, intense peak of approximately 100

µs duration. Air related peaks ($^{16}O^+$, H_3O^+, O_2^+, N_2^+, NO^+, NH^+, etc) can be seen in the low m/Q region of the mass spectra; they are most probably due to a gas leak present in the sample holder used for the vacuum measurement. Doubly charged Cu and Zn species are also detected, although with two order of magnitude lower intensity than the singly charged. Because the limited dynamic range of the detection system did not allow for a quantitative comparison for the matrix elements present, the data of the minor and trace elements were evaluated. As listed in table 2.6, all matrix and minor elements present in the samples showed significantly higher intensities when using the LAFU source, in particular when integrating the entire transient peak. Especially high m/Q

TABLE 2.6: Signal intensity using different operating condition.

	Signal maximum (A.U.)			Integrated signal (A.U.)		
	2.5 MHz 20 V_{pp} 1.36 L/min	2.5 MHz 20 V_{pp} 0.68 L/min	High vacuum	2.5 MHz 20 V_{pp} 1.36 L/min	2.5 MHz 20 V_{pp} 0.68 L/min	High vacuum
^{107}Ag	0.4	0.5	0.1	4.3	5.3	0.2
^{116}Sn	1.6	1	0.6	18	10	0.7
^{208}Pb	1340	490	40	12600	4940	65

isotopes were found to increase dramatically in signal intensities and enhancements of up to 200 times could be realized for the most sensitive conditions. At lower m/Q the enhancement was more moderate but still 20 times enhancement was obtained. It is interesting to notice the space charge effect of heavier species on the shape of the transient signal of Copper, resulting in signal suppression for Cu when the majority of heavier species is present. Also for this sample material the signal intensity generally increased with buffer gas flowrate. However, as it can be seen for Ag (Tab. 2.6), the lower m/Q appeared suppressed at higher flow. Upon closer inspection of the transient signal indicated that this is most likely a result of higher space charge effects caused by the higher Pb-content. The abundance of molecular ions is significantly higher for the LAFU source compared to ablation in vacuum. This indicates that a higher amount of water was present inside the source resulting an a higher reaction (and molecular ion generation) probability. It is considered a result of adsorbed

moisture on the interior surface and residual amounts present in the buffer gas supply.

2.3 CONCLUSION AND OUTLOOK

A novel ion source for laser ablation and ionization with TOFMS detection has been realized and a first characterization of the system was performed. The source enabled detection of laser-generated ions by carrying out ablation at elevated pressure in a helium buffer gas in combination with an RF only ion funnel for ion focusing before an electrostatic ion optics. Thereby a higher ion transmission could be achieved when compared to an ablation/ionization in high vacuum. The duration of the transient peak was found to increase by more than 10 times and depended significantly on the pressure within the ablation region. Increasing the Helium flow rate into the ablation region while maintaining the pressure downstream the nozzle constant, caused the signal intensities to become higher and shorter. In relation to that, an increase in the mean velocity of the ion packet is indicated through shorter ion transit times. Species with different m/Q were almost equally affected by gas dynamics, while operating parameters of the ion funnel exhibited a distinctly different effect on low and high m/Q. The introduction of the buffer gas on the other hand detrimentally affected the situation with respect to spectral overlaps. A variety of water adducts to atomic and cluster ions complicate the spectra. The fact that the temporal evolution of these adducts is different from the atomic ions together with higher mass resolving power and/or purification of the gas is expected to alleviate this situation. A major limitation in this study however was the high ion currents generated during the ablation event. This caused problems in respect of detector saturation for matrix elements in particular and also space charge effects are notable inside the ion funnel. Nonetheless the results obtained in this study show that the combination of an ion funnel and the CD-nozzle for ion thermalization is an effective means to increase sensitivity while still allowing for kHz laser repetition rates for the direct elemental analysis of solids. Current work is focused on lowering the ion current produced per laser pulse by employing femtosecond LA at lower fluence and spot size. Thereby not only a better representation of the sample stoichiometry is expected but also space charge and detector saturation shall be minimized or avoided. [52, 167].

3

INFLUENCE OF LASER PULSE DURATION

The use of a femtosecond (fs) laser as been proven to reduce inter element fractionation effects found when employing ns laser pulses (chapter 1), for this reason the LAMS setup was combined with a fs laser that is available in the laboratory. To investigate the influence of laser pulse duration on the detection capabilities of the setup, parameter studies were performed.

3.1 EXPERIMENTAL AND MATERIALS

The experimental setup remained virtually unvaried from the previous chapter, with the exception of the implementation of a new RF power amplifier (QBH 2832, Spectrum Microwave, USA) and of a gas purifier (MC200-902, Pure Gas Products, Germany). New calibration of the pressure sensor in the ion funnel region was performed.

For these studies two lasers were used, the frequency doubled Nd:YAG laser (500 μm spot diameter, fluence 1.02 J/cm^2 , irradiance 3.5$\times$10^8 W/cm^2) used also in the previous experiments (chapter 2) and a frequency doubled Ti:Sapphire (Legend, Coherent Inc., USA; τ =250 fs, λ = 400 nm, spot diameter: 50 μm, fluence: 1.06 J/cm^2, irradiance: 6.8$\times$10^{12} W/cm^2). A schematic of the fs laser optical setup can be seen in figure 3.1. The fs-laser employed exhibited high day to day variability in beam shape, and therefore a pinhole was employed after frequency doubling in order to "clean" (spatial filtering) the beam profile. The output laser energy was regulated changing the conversion efficiency during the frequency doubling of the laser pulse. Using the fs-laser with high repetition rate and low fluence allowed to establish a quasitstationary ion current that was used to generate the detector's single ion conversion factor (see chapter 1.10). The voltage applied to the MCP was lowered from the previously used 2100 V to 1900 V, which additionally reduced the danger of detector saturation.
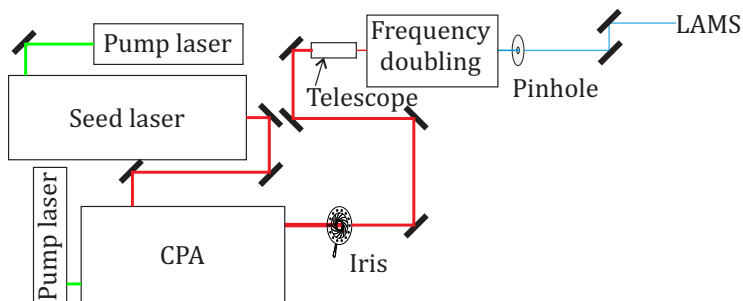
FIGURE 3.1: Schematic of fs laser optical set-up. The seed laser, is producing laser Infrared (IR) fs pulses ($\tau = 250$ fs, $\lambda = 800$nm) which are then frequency double to blue light ($\lambda =400$ nm). The telescope positioned in front of the frequency doubling unit is employed to increase the conversion efficiency. The iris and pinhole are used to produce Gaussian beams

Both lasers were used at a repetition rate of 10 Hz and in both cases a pinhole was used. The ion optic parameters used in the previous studies were found to be optimal also when employing the femtosecond laser. He was employed as buffer gas. For the experiments, certified brass alloy standard (MBH B26, tab. 2.3) was used to evaluate the influences of laser pulse duration on the signal acquired.

3.2   RESULTS AND DISCUSSION

During preliminary experiments employing fs laser pulses, it was observed that an ion detection increased when the distance of the sample to the CD-nozzle aperture was increased from ≈ 1 mm to ≈ 3 mm. Afterwards the distance was kept a ≈ 3 mm. Employing the different sample position it was also found that a lower He flow rate (from 1.36 l/min to 0.71 l/min), and therefore a lower pressure (from 44 mbar to 23 mbar) in the ablation region, was sufficient for optimal ion detection. Changing the distance of the sample together with a change in pressure in the ablation region, changes the number of collision experienced by the laser generated ions which influences the final detection efficiency of the set up. This basic position adjustment made a more systematic investigation of this effect difficult. In chapter 2 it was shown how cluster ions were found to be a major limitation, making the interpretation of the spectra difficult. The origin of gas

impurities (e.g. water) was attributed to the laboratory gas supply and therefore a gas purifier was implemented to the gas feed before the ablation chamber. Already from the first tests it became clear that the use of a gas purifier did not diminish the abundance of cluster ions and the water origin was investigated further (see chapter 4.2.9). During the preliminary tests it was also noticed that the pressure in the ion funnel region was affecting the composition of the ion cloud reaching the detector. After the pressure sensor calibration, it was found that an ion funnel pressure of 4 mbar resulted in a high transmission of atomic ions and simultaneously suppression of molecular ions. The change from 3 mbar to 4 mbar is considered to be a result of the increased sample distance from the nozzle aperture. With this new gas parameters it was also found that the m/Q transmission dependence was decreased when an RF frequency of 5 MHz and a RF amplitude of 20 V_{pp} were employed. However due to unforeseen reason, the previously used RF amplifier had to be replaced and the use of a different RF amplifier could also explain the different optimal RF parameters found. For the above mentioned reasons, standard operating condition were chosen to be 23 mbar in the ablation region, 4 mbar in the ion funnel, an RF frequency of 5 MHz and an RF amplitude of 20 V_{pp}.

3.2.1 *Single spot ablation*

Signals from six thousand laser ablation events were collected and the evolution of the integrated transient signal for different isotopes obtained ablating the same material (MBH 26) but using lasers pulses with different pulse duration and wavelength is shown in figure 3.2. Each point represents the averaged ion signal of 300 subsequent laser pulses. The overall signal evolution with increasing number of pulses for the two different laser sources is substantially different. In the upper plot it can be seen that in the case of fs-pulses an increase in signal was found during the first 1500 pulses and afterwards a signal decrease sets in. The precise reasons behind this finding are unknown and may relate either to different ion formation, different ion ejection trajectory or different initial kinetic energy of the ions. In the lower plot, showing ns-LAMS, one can see that the signal decreased from half an order of magnitude (in the case of Al) to almost two orders of magnitude (for Zinc) within the first 1200 laser pulses. The lower melting point of Zn typically leads to preferred release of the metal at the onset of ablation when the sample is heated by a ns laser pulse [168]. This is less pronounced when looking at observing the more similar evolution of the

signal in the case fs-LAMS where smaller thermal alteration of the sample reduces this fractionation effect [169]. Fluctuation in the signal of lead were found for both laser sources, and they were attributed to inhomogeneities in the sample [170].
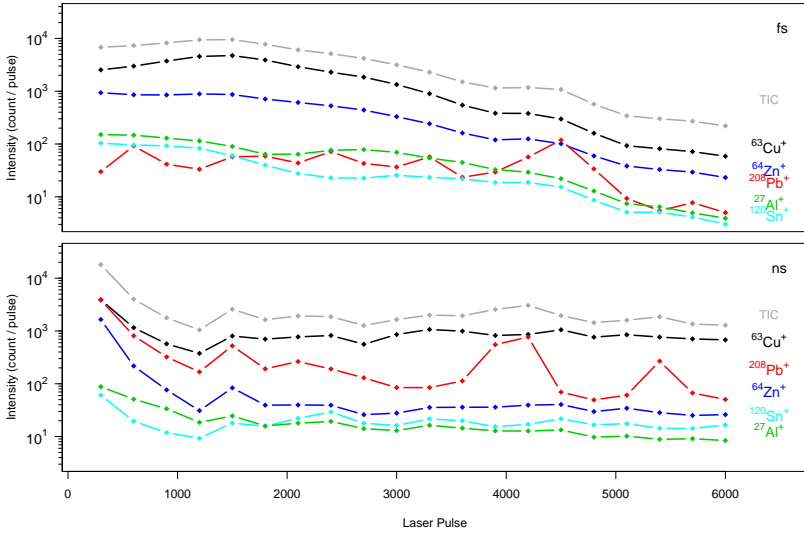
FIGURE 3.2: Integrated ion signals during LAMS for sample MBH B22. Each point represent the averaged ion signal of 300 laser pulses.

In figure 3.3 the averaged m/Q spectra for the two laser sources for the experiment presented in figure 3.2 can be seen. The most significant species have been identified according to m/Q ratio and isotopic pattern. It can be noticed that the spectra obtained with different laser pulse duration differs mostly for species with m/Q up to 60. When looking at fs-LAMS spectra it is possible to notice air related species (H_3O^+, O_2^+), whereas such species are not present in the case of ns laser pulses. The detection of these species may arise from a different interaction of molecular species present in the buffer gas with the plasma generated from the target after irradiation with fs-pulses. When the experiment was performed without a target, no ions were detected. This may hint to the absence of plasma formation in pure buffer gas, however it is not conclusive since ion transmission was also found to be dependent on position where the ions are formed: when no

target is present ion formation may occur but not transported efficiently through the CD nozzle.
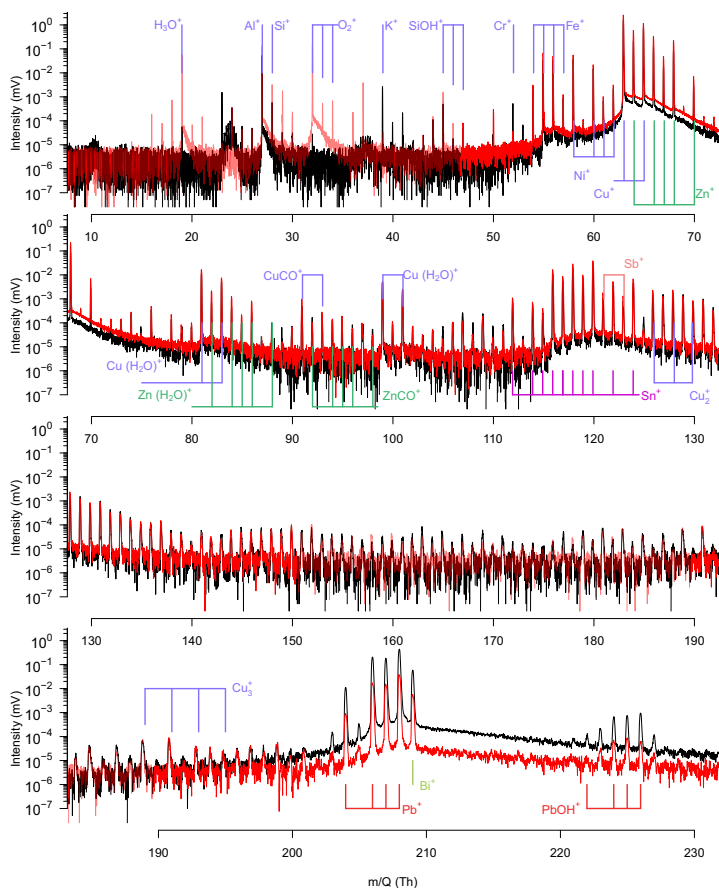
FIGURE 3.3: Average m/Q spectra for two laser sources used. In red the spectra obtained using fs laser pulses, in black the ns laser pulses. The most predominant species were assigned using isotopic patterns

Looking at the ns-LAMS spectra, an elevation with a periodic structure, in the signal in the vicinity of m/Q 25 and 38 m/Q can be seen. It is arising from species which reached the detector together with the ions from a subsequent TOF-extraction. The species arriving after the TOF period are most likely water cluster with m/Q higher than 330, which had a flight

time longer than the 31.250 μs TOF period used. It is also possible to notice an elevated baseline in the region of 200 m/Q in the case of ns-LAMS. The elevated baseline is resulting from the higher quantity of lead ions transmitted when ns laser pulses where employed. In both cases the region in the m/Q spectra ranging from 70 to 200 is heavily populated by peaks which were attributed from molecular ions and water adducts .

Right in figure 3.4 it can be seen that the ion signals for these experiments were typically higher when employing fs laser pulses than for ns pulses. The volatile element Pb (BP: 1749 °C) and Bi (BP: 1564°C) showed however an inverted trend. This effect was also observed in the work of Zhang et al [52] and it is most likely due to ns-laser pulses presenting a more thermal ablation. It could be noted though, that Sb, with even lower BP, and Ag, with an higher BP, don't follow the trend. In general, the ions produced using fs pulses were found to be reaching the detector faster when compared to the ns laser produced ions (Fig. 3.4 left). When the evolution of the transient profile of both Cu^+ and Pb^+ for the different laser pulses duration is compared it is possible to notice difference in the shapes. The signals generated using fs laser showed a more confined characteristic, whereas longer tailing was present for the nanosecond pulses. An initial maximum was observed at 0.5 ms in the ns-LAMS signal of Cu^+ and Pb^+, which was found only in the first 1000 pulses. This is currently assumed to be arising from the interaction with the material deposited on the nozzle, which was not cleaned previous to the experiment, and the laser generated plasma created above the surfaces.

Water adducts (represented in the figure using $Cu(H_2O)2^+$) were found to occur at similar ratio to their parent ion (Fig. 3.4, left violet) and similar intensity for both laser sources. Even tough less pronounced than in the previous chapter (2), it can be seen that the ratio of cluster to parent ion was found to be increasing during the first ms before a relatively stable abundance ratio was obtained. The reason behind this finding is most probably given by the larger cross section of the molecular ions, which increases the collisions experienced in the ion funnel region, slowing the molecular ions: corroboration of this hypothesis could also be found when the pressure in the ion funnel region was increased (Fig. 3.10). It is interesting to notice that in the case of fs-LAMS, O_2^+ ions were detected resulting in an intense signal and that these ions reached the detector earlier than the major sample components. In the case of ns laser pulses, O_2^+ signal was almost absent, which indicates that low irradiance ablation could not ionize species with higher ionization energies.
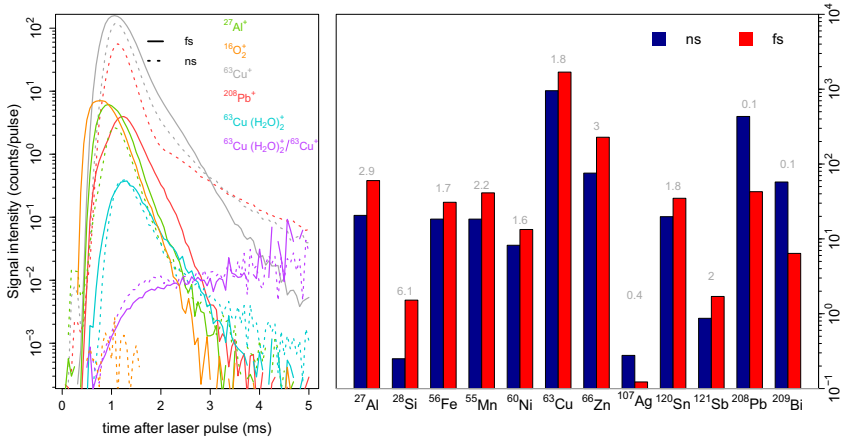
FIGURE 3.4: *Left:* Averaged transient signal for Al^+, Cu^+, Pb^+, and $Cu(H_2O)2^+$, from 6000 laser ablation events (RF frequency 5 MHz and the Rf amplitude 20 V_{pp}), funnel pressure of 4 mbar, pressure in the ablation region 23 mbar). The dotted lines represent signal profiles for the nanosecond pulses, whereas the solid lines represent fs pulses. *Right*: Average integrated signal, for different isotopes. Their identity (absences of isobaric interferences) was verified by controlling the isotopic pattern for the analyzed m/Q species. The number represent the ratio of data generated using fs laser pulses over data generated using fs laser pulses.

3.2.2 *Laser pulse duration effects on operating condition*

To assess the effect of the laser pulse duration on the ion transmission capability of the setup, parameter studies where performed. As a set of reference variables using a pressure in the ablation region of 23 mbar (flow rate 0.71 l/min), an ion funnel pressure of 4 mbar, employing an RF field of 20 V_{pp} and oscillating at 5 MHz were chosen. One parameter was varied individually, maintaining the others constant, and 500 ablation events employing laser fluence of circa 1 J/cm^2 (see 3.1) were recorded. The aim of the studies presented in this section was to compare the signal responses for both laser sources under different source operating condition. Employing the ns laser pulse no substantial signal change was observed after the initial 1500 pulses(Fig. 2.4). The period after 2000 pulses was considered sufficiently stable to evaluate the ion funnel characteristics. It was there-

fore decided not to change position for each experiment and discard the first 2000 laser pulses. When the fs laser was used, on the other hand, ion signal intensities never reached a stable level. As no obvious change in the ion beam composition was detected (Figure 3.2), these experiments were carried out by collecting ion signals from fresh ablation spots each. The raw intensities for both laser systems are thus not comparable. The trends in ion transmission upon variation of the ion funnel settings are however considered representative.

3.2.2.1   *RF parameters*

The ion transmission dependence on RF amplitude and frequency for different laser pulse duration can be seen in figure 3.5 . Each point represents the integrated averaged signal over 500 laser pulses for different isotopes. Only one variable was changed (either RF amplitude or RF frequency), maintaining the other constant over the course of the experiment. The upper limits (from 1.2 MHz to 5.4 MHZ and from 2 V_{pp} to 22 V_{pp}) investigated were imposed by the hardware. Inhomogeneities [170] in the standard reference material used, affected the evaluation of Pb response curves and it was difficult to differentiate between higher ion transmission or higher ion generation due to a locally variable mass fraction. For both laser sources similar trends can be observed, increased transmission was found with increasing amplitude, with ions with lower m/Q reaching the plateau at lower voltages. Changing the applied frequency was shown to have a stronger dependence on laser pulse duration, which is in agreement with the results presented in the chapter 2. Looking at the effect of RF amplitude on ion transmission for different m/Q, only minor differences for the two laser sources were found. Comparing fs-LAMS and ns-LAMS, a higher ion transmission was obtained for fs-LAMS for the main elements at low amplitude (2 V_{pp}). Slight differences in the signal increase are present when considering the region from 0.2 MHz to 2.5 MHz and from 2 V_{pp} to 10 V_{pp} for both laser sources. ns-LAMS presented a steeper increase in transmission. This may arise from an axial confinement of fs laser generated ions. It can be also seen that when employing an RF frequency higher than 4 MHz with the ns laser, a three order of magnitude decrease in transmission for species with higher m/Q ratio is found whereas only one order of magnitude is loss in the Total Ion Current (TIC). It is interesting to notice that TIC (calculated by summing 214 integrated value for different mass channel across the m/Q spectrum) in the case of ns lasers, seems to

be influenced by the ion cloud composition. Higher total ion current was found due to higher signals of Pb and Bi.
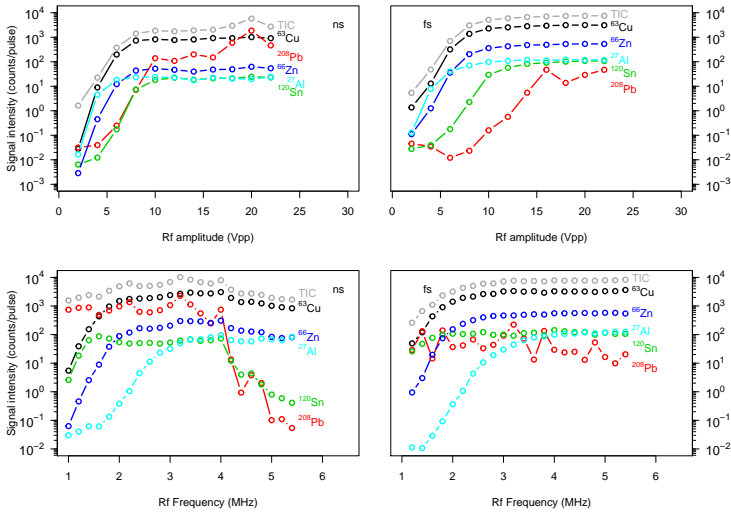
FIGURE 3.5: *Top:* Integrated signal intensities of the main components plotted against the applied RF amplitude (RF frequency 5 MHz, funnel pressure of 4 mbar, pressure ablation 23 mbar). *Bottom:* Integrated signal intensities of the main components plotted against the applied RF frequency (RF amplitude 20 V$_{pp}$,funnel pressure of 4 mbar, pressure ablation 23 mbar). *Left:* ns-LAMS. *Right:* fs-LAMS.

3.2.2.2   *Gas dynamics*

The delay between laser pulse and transient peak maximum of different elements for the 2 different lasers is plotted against the pressure in the ablation region and in the ion funnel can be found in figure 3.6. The pressures investigated varied from 5 mbar to 47 mbar for the ablation chamber and from 1 mbar to 5 mbar for the ion funnel. The ion travel time was reduced with increasing pressure for both laser sources, showing similar trends. In both cases an exponential decay was found to reach a plateau at around 1 ms, which is slightly lower (higher speed) for the fs laser pulses generated ions. This trend was found for all the pressures investigated. The difference in arrival time found between the data presented here and chapter 2

are explained by a difference in sample position with respect to the nozzle entrance.
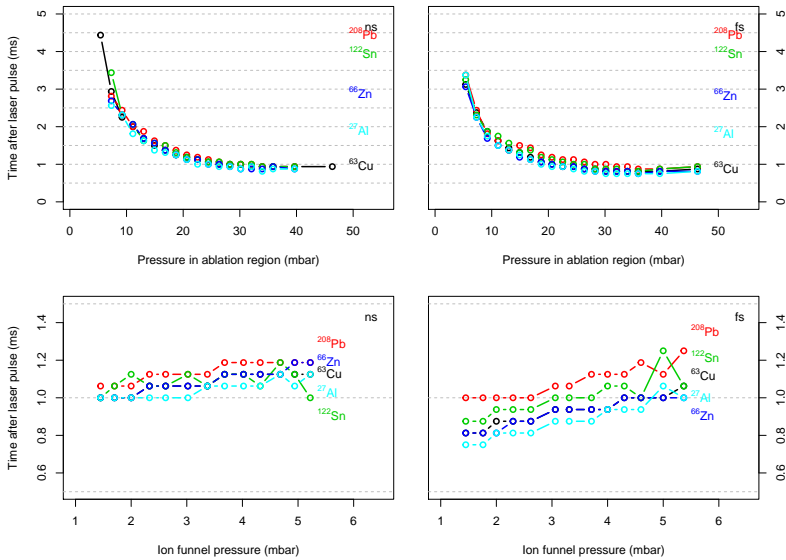
FIGURE 3.6: The delay between laser pulse and the transient peaks' maxima in dependence to pressure in the ablation region (*top*) and ion funnel pressure (*bottom*). *Left:* ns-LAMS. *Right:* fs-LAMS.

It can be noticed that, when the ablation took place with a pressure of 5 mbar using the ns pulses, it was only possible to define a peak maximum for Cu^+, since the other ions were barely detected and their transient shape was irregular. Changing the ion funnel pressure was found to increase the arrival time of the ions for both laser sources, with a more pronounced effect in the case of fs-LAMS. Figure 3.6 (bottom right) shows that fs pulses produced ions with a greater temporal separation between the different m/Q, with heavier ions being slower than lighter ones. This would suggest that their kinetic energies resulted from iso-energetic processes (i.e. field acceleration in the plasma plume) rather than iso-kinetic ones (choked flow in the nozzle or gas expansion in ion optic region). The step wise increase in this case is due to the time resolution (62.5 μs) used in this the experiments. The dependence of sensitivity on pressure changes (in both ablation chamber and ion funnel) for ns and fs pulses can be found

in figure 3.7. For increasing pressure in the ablation chamber (Fig. 3.7 top) the sensitivities across the mass spectrum initially increase until reaching a maximum around 20 mbar. Afterwards a decrease in sensitivity can be found, with exception of Zn^+, which seems to reach a maximum at higher pressure in the case of fs-LAMS. The cause of this difference in behavior was however not clear, but it may be related to a wider expansion of the more volatile compound. The difference between the finding presented in chapter 2 are not fully understood. It seems however to be depending on sample position relative to the nozzle entrance and therefore a different number of collisions experienced.
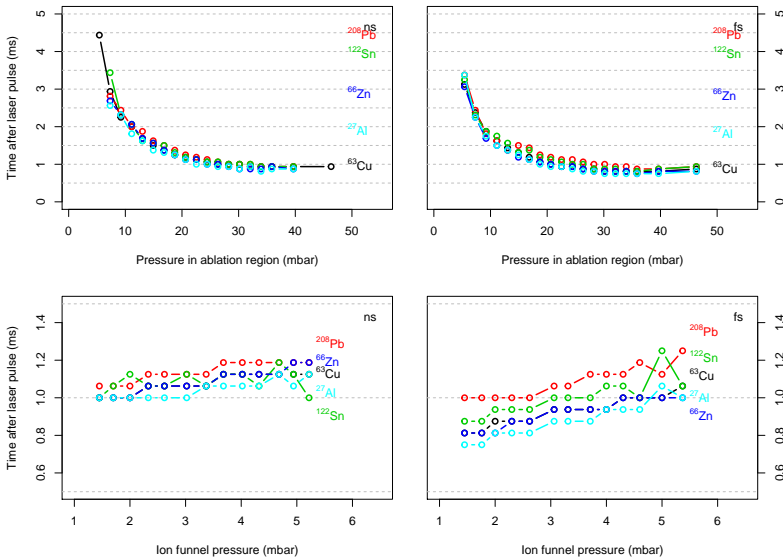
FIGURE 3.7: *Top:* Integrated signal intensities of the main components plotted against the employed pressure in the ablation chamber (RF frequency 5 MHz and the RF amplitude 20 V$_{pp}$,funnel pressure of 4 mbar) for ns laser pulse (*left*) and fs laser pulses (*right*). *Bottom:* Integrated signal intensities of the main components against the employed pressure in the ablation chamber (RF frequency 5 MHz and the RF amplitude 20 V$_{pp}$, pressure ablation 23 mbar) for ns laser pulse (*left*) and fs laser pulses (*right*).

In figure 3.7 bottom, the influence of ion funnel pressure to the ion detection for the two laser sources can be found. Similar trends can be seen

for both laser sources. It seems however that fs laser pulses produced ions tend to be about 1.4 times (Zn: 1.6 times) stronger attenuated at the highest pressure used than ns laser produced ions. The reason behind this finding is not clear since changing the pressures changes simultaneously gas dynamics and number of collision experienced by the ions.

3.2.3 *Clusters ion abundances*

Figure 3.8 presents the evolution of the abundance of selected molecular ions in a single spot ablation experiment. The data presented are from the experiments shown in section 3.2.1.
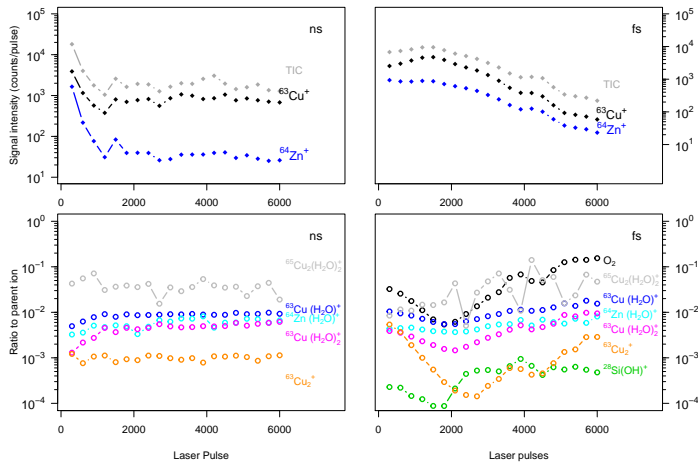
FIGURE 3.8: Molecular ions and clusters for different laser sources (ns *left* and fs *right*). Each point represent the average signal of 300 ablation events (RF frequency 5 MHz and the RF amplitude 20 V_{pp}, funnel pressure of 4 mbar, pressure ablation 23 mbar). Intensity ratio to the parent ion of the cluster, more precisely $^{63}Cu(H_2O)^+$, $^{63}Cu(H_2O)_2^+$, $^{63}Cu_2^+$ were normalized using $^{63}Cu^+$ signal, $^{63}Cu_2(H_2O)_2^+$ using $^{63}Cu_2^+$ signal and $^{64}Zn(H_2O)^+$ using $^{64}Zn^+$ signal. The signal of O_2^+ and $Si(OH)^+$ were normalized using TIC. Major isobaric interferences were excluded by controlling the isotopic pattern for the analyzed m/Q species. *Top:* Parent ions. *Bottom:* Cluster ions

Each point represents the intensity ratio of molecular ions and water cluster ions relative to their parent ions, more precisely $^{63}Cu(H_2O)^+$, $^{63}Cu(H_2O)_2^+$, $^{63}Cu_2^+$ were normalized to the $^{63}Cu^+$ signal, $^{63}Cu_2(H_2O)_2^+$ to $^{63}Cu_2^+$ signal and $^{64}Zn(H_2O)^+$ to $^{64}Zn^+$ signal. The signal of O_2^+ and $Si(OH)^+$ are normalized to the TIC. The identity of the species was verified by verifying the relative abundances for the analyzed isotopes. Major differences can be seen between the signal evolution of the same species when the two laser sources are compared.

In the case of ns pulses, variation within the experiment are less pronounced, with a slight decrease for $^{63}Cu(H_2O)^+$ and $^{63}Cu_2^+$ and increase for $^{63}Cu(H_2O)_2^+$. More pronounced variations are present in the case of fs-pulses. Similar signal ratio evolution can be seen for diatomic molecules $^{63}Cu_2^+$ and O_2, however after the first 1800 laser pulses the signal ratio of $^{63}Cu_2^+$ present a stronger decrease within the subsequent 600 laser pulses. $SiOH^+$ was found to follow a different trend, with an initial decrease for the first 1800 pulses followed by an increase up to a plateau. For both lasers the evolution of $Zn(H_2O)^+$ and $Cu(H_2O)^+$ intensity ratios followed similar trend with similar relative abundances.

Figure 3.9 summarizes the differences in cluster ion formation observed in the previous experiments. When fs laser pulses were employed also molecular ions (H_3O^+, O_2^+) were found in the spectra, whereas in the case of ns laser pulses the detected signal in the respective mass channel was determined by the baseline. It is interesting to notice that cluster formation was also depending on laser pulse duration. Higher abundances of $^{63}Cu_2(H_2O)^+$ and, to a lesser extent, $^{63}Cu(H_2O)_2^+$ were observed when employing nanosecond laser. Molecular ion formation and transmission was also found to be dependent on laser pulse duration. Using fs-laser pulses the signals of O_2^+ and H_3O^+ appeared in the spectra, which indicates that high irradiance ablation can more efficiently ionize species with higher ionization energies.
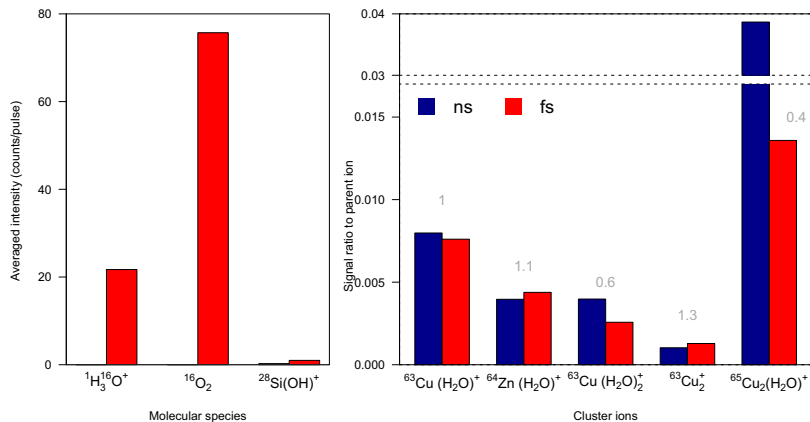
FIGURE 3.9: Molecular and cluster ion relative abundances for different laser sources. Averaged transient signal over 6000 laser ablation events (RF frequency 5 MHz and the RF amplitude 20 V_{pp}), funnel pressure of 4 mbar, pressure ablation 23 mbar). Intensity ratio to the parent ion of the cluster, more precisely $^{63}Cu(H_2O)^+$, $^{63}Cu(H_2O)_2^+$, $^{63}Cu_2^+$ were normalized using $^{63}Cu^+$ signal, $^{63}Cu_2(H_2O)_2^+$ using $^{63}Cu_2^+$ signal and $^{64}Zn(H_2O)^+$ using $^{64}Zn^+$ signal. The signal of O_2 and $Si(OH)^+$ were normalized using TIC.

In figure 3.10 the dependence of the relative abundance of the cluster and molecular ions to pressure changes in both, ablation region and ion funnel, can be found. The data presented were obtained with the experiments presented in section 3.2.2.2.

Considering the effect of pressure changes in the ablation region it can be seen that between 20 mbar and 40 mbar, the change in pressure had the same effect on cluster ions abundances for both laser sources. All the species were found to increase with Cu_2^+ showing the largest increase by 2.5 orders of magnitude. The higher formation rate of Cu_2^+ is most probably due to the higher compression of the laser generated plasma at higher pressures ablation resulting in more collisions. When the pressure in the ablation region was varied between 5 and 20 mbar, major differences were found for $^{63}Cu(H_2O)_2^+$ and $^{63}Cu_2(H_2O)_2^+$ whose relative intensities appeared to drastically decrease in the case of fs-LAMS while only minor changes occur with the ns laser .

When the pressure in the ion funnel was increased an approximatively lin-
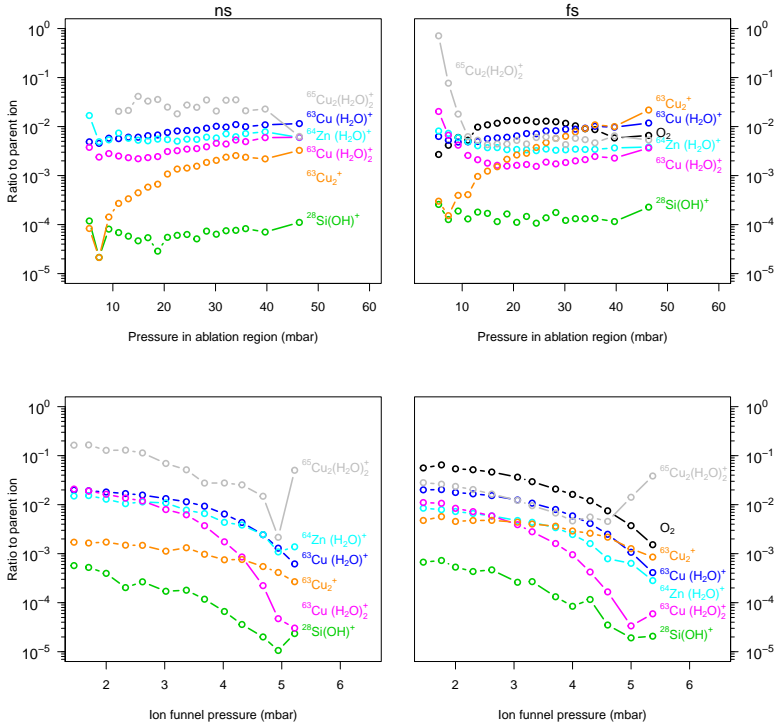
FIGURE 3.10: Changes in molecular and cluster ions in dependence to gas parameter for different laser sources. Each point represent the average signal of 300 ablation events (RF frequency 5 MHz and the RF amplitude 20 V_{pp}). Intensity ratio to the parent ion of the cluster, more precisely $^{63}Cu(H_2O)^+$, $^{63}Cu(H_2O)_2^+$, $^{63}Cu_2^+$ were normalized using $^{63}Cu^+$ signal, $^{63}Cu_2(H_2O)_2^+$ using $^{63}Cu_2^+$ signal and $^{64}Zn(H_2O)^+$ using $^{64}Zn^+$ signal. The signal of O_2 and $Si(OH)^+$ were normalized using TIC. Absences of major isobaric interferences was validated controlling isotopic pattern for the analyzed m/Q species.

ear decrease of all the molecular and cluster species was observed. It is interesting to notice that the suppression rate for the different species seems to correlate with the size of the species and therefore with the amount of collision which they experience in the ion funnel region. When a ion is completely thermalized it will not exit the ion funnel region and therefore

it will not be detected, resulting in a lower signal. The increase found for $^{65}Cu_2(H_2O)_2^+$ at and 5.5 mbar (and 5 mbar in the case of fs LAMS) is not fully explained, however it may show that cluster formation is present in ion funnel region. The different signal suppression for diatomic species (O_2^+ and Cu_2^+), is most likely due to the different mass of the ions, since the quantity of energy dissipated by a collision and the scattering angle are dependent on the mass difference between the collision partners.

3.3   CONCLUSION

A direct comparison of the ns laser and the fs laser was made in order to study if and how significant the use of a high-irradiance laser can improve the capabilities of the LAFU source. During the initial tests it was noticed that a higher ion signal could be achieve when the distance of the sample to the CD nozzle's entrance was increased. For this new sample position, a lower effective pressure in the ablation chamber was found to be optimal for ion detection. A broader m/Q transmission range was also found when an RF frequency of 5 MHz and 20 V_{pp} were used with the new RF-amplifier. When the two lasers with similar fluence, yet different irradiance, were used, it was found that the signal evolution differed substantially as the crater developed. Employing fs laser pulses for the ablation of a brass sample resulted in a slight increase in ion signals during the first 1500 laser pulses. This was followed by a steady decrease for nearly an order of magnitude for the subsequent 4500 pulses. In the case of ns pulses on the other hand, the first 1200 resulted in a steep decrease by circa one order of magnitude, followed by a comparably steady state signal across nearly 5000 pulses. In general a 1.5 to 3 times increased sensitivity was observed for the majority of the ions, with exception of Pb and Bi where the use of ns laser pulses resulted in higher signals. Similar trends for the two laser sources were found when changes in RF parameters were investigated, however transmission of species with higher m/Q at frequency over 4 MHz seems to be negatively affected when generated by ns laser pulses. It was shown that using fs laser pulses resulted in a shorter travel time of the ions and greater separation between the arrival time of different m/Q, however gas dynamics seems to be the dominating parameter determining the ions' arrival time.

Molecular ion formation and transmission were also found to be dependent on laser pulse duration using fs-laser pulses signals of O_2^+ and H_3O^+ appeared in the spectra, which indicates that high irradiance ablation can

more efficiently also ionize species with higher ionization energies. Similar abundances for cluster ions were found for the 2 laser sources, and it was further investigated the dependence of cluster ion to pressure dynamics. For both laser sources higher pressure within the ablation region caused their relative abundances to increase because of the higher density of the laser generated plasma plume and eventually a higher total amount of the reactants. A higher pressure inside the ion funnel on the other hand led to a decrease in relative abundances of the larger ions due to more efficient cooling and, eventually, trapping inside the ion funnel.

4

ANALYTICAL CAPABILITIES: fs-LAMS OF METALS

4.1 EXPERIMENTAL

Different energies of the laser pulses were employed. The amount of laser energy reaching the sample was varied by changing the efficiency of frequency doubling process. The laser pulse energies reported were measured after the pinhole aperture before each experiment (see Fig. 3.1), nonetheless the laser fluences presented were corrected for the energy loss between the energy measurement position and the target surface. It was found an energy loss circa 58%, due to the optical components (lens and windows) present in the setup. The Ion optic parameters used in the previous studies were not changed. The extraction voltages and lenses voltages of time of flight mass analyzer were optimized aiming at the highest ion transmission and mass resolving power. Helium was employed as buffer gas. The crater morphology and crater volume was measured using Confocal Microscopy (CM) (PluNeox, Sensofar, Spain) and the obtained data evaluated using the software Gwyddion [171]. For the experiments, a certified Standard Reference Material (SRM) of a brass alloy (MBH B26, Tab. 2.3), a steel alloy (ECRM 298-1 Tab. 4.1) and a zinc based metal (MBH 42X Z7 Tab. 4.2) were used. The elemental compositions of each sample can be found below.

TABLE 4.1: Elemental composition in weight percent of the steel sample ECRM 291-1. No uncertainties were given by the manufacturer.

Element	B	C	N	Al	Si	P	S	Ti
Mass%	0.0021	0.0146	0.263	0.0286	0.262	0.0198	0.0006	0.0014
Element	V	Cr	Mn	Fe	Co	Ni	Cu	Mo
Mass%	0.06	24.72	0.398	63.377	0.0662	7.068	0.201	3.799
Element	Pb							
Mass%	0.000079							

TABLE 4.2: Elemental composition in weight percent of the zinc sample MBH 42X Z7 Type C.

Element	Al	Mn	Fe	Ni	Cu	Cd	Sn	La
Mass%	4.39	0.0045	0.027	0.0067	0.0249	0.03	0.012	0.08
Uncertainty	0.05	0.0003	0.003	0.0003	0.0007	0.001	0.001	0.01

Element	Ce	Pb
Mass%	0.09	0.0097
Uncertainty	0.01	0.0009

4.2   RESULTS AND DISCUSSION

To explore the analytical capabilities reachable with the developed setup employing fs laser pulses, different experiments were performed to assess the figures of merit of the setup and of the technique.

4.2.1   *Crater morphology*

The different samples were ablated under constant operating conditions (RF frequency: 5 MHz and the RF amplitude: 20 V_{pp}, funnel pressure: 4 mbar, pressure ablation region: 23 mbar), while varying the laser pulse energy (20 μJ corresponding to a fluence on the sample surface of $\approx$ 0.4 J/cm^2, 30 μJ corresponding to $\approx$ 0.6 J/cm^2, 40 μJ corresponding to $\approx$ 0.8 J/cm^2 and 50 μJ corresponding to $\approx$ 1.2 J/cm^2). All the experiments were done in triplicate and each measurement consisted of 200 laser pulses applied on a fresh surface. All samples were polished before the experiment. It was not possible to count the number of laser pulses reaching the surface of the sample since the laser had to be manually stopped after the LAMS measurement. Therefore the actual count for each experiment may be uncertain by 20 pulses.

In figure 4.1 different craters, formed by the consecutive ablation of circa 200 laser pulses with an energy of 30 μJ ($\approx$ 0.6 J/cm^2) are shown. It can be seen that all the craters exhibit a circular shape with small variance between the different matrices (Tab. 4.3). In the picture of the brass sample (MBH 26, insert A) and steel sample (ECRM 298-1, insert B) a halo around the crater can be seen. It was not investigated if the halo is arising from material deposited during the crater formation, from modification of the
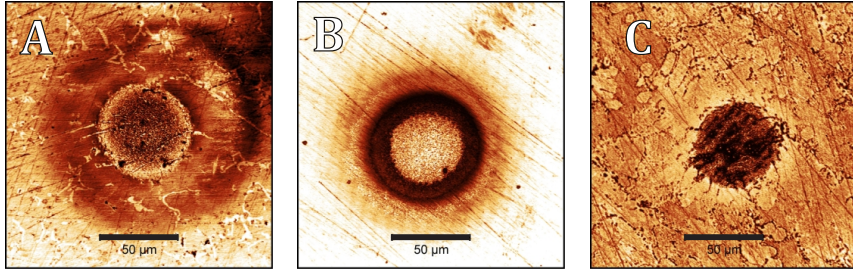
FIGURE 4.1: Microscope pictures of the ablation craters in different sample materials employing 200 laser pulses with a pulse energy of 30 μJ.
A: Brass (MBH26). **D:** Steel (ECRM298-1) **D:** Zinc (MBH 42X Z7). The original gray-scale image was modified to the current color for visualization purpose.

sample surface due to laser irradiation or interaction of the laser generated plasma plume.

In figure 4.2 the morphology, obtained using confocal microscopy (CM), of the craters can be seen. CM measurement were performed with the sample in the sample holder of the LAMS experiments, in order to determine the inclination of the sample. In the upper part of the figure it can be seen that a Gaussian curve could be fitted to the crater morphology for the brass sample as well as for the Zinc sample. Showing that the ablation was obtained from a Gaussian beam. On the other hand the profile obtained on the steel sample, appears be cylindrical in the top part and exhibits poor correlation with a Gaussian shape. The profilometry measurements of the zinc sample showed a rough surface at the bottom of the crater. Optical investigation also confirmed the finding. It can be also seen that MBH26 and ECRM 298-1 were not oriented perpendicular to the incoming laser beam (2.4° tilt for MBH26 and 1.4° tilt for BCR298-1). The profilometry experiments allowed to estimate the ablated volume of different materials at different energies (Tab. 4.3). To obtain this information the acquired surface were evaluated using build-in functions in Gwyddion. The surface plane was computed from image points of the surface and was subtracted from the data, which eliminated the tilt. The crater volumes as well as the ablated spots' radii and the depths were extracted from the profilometry data.
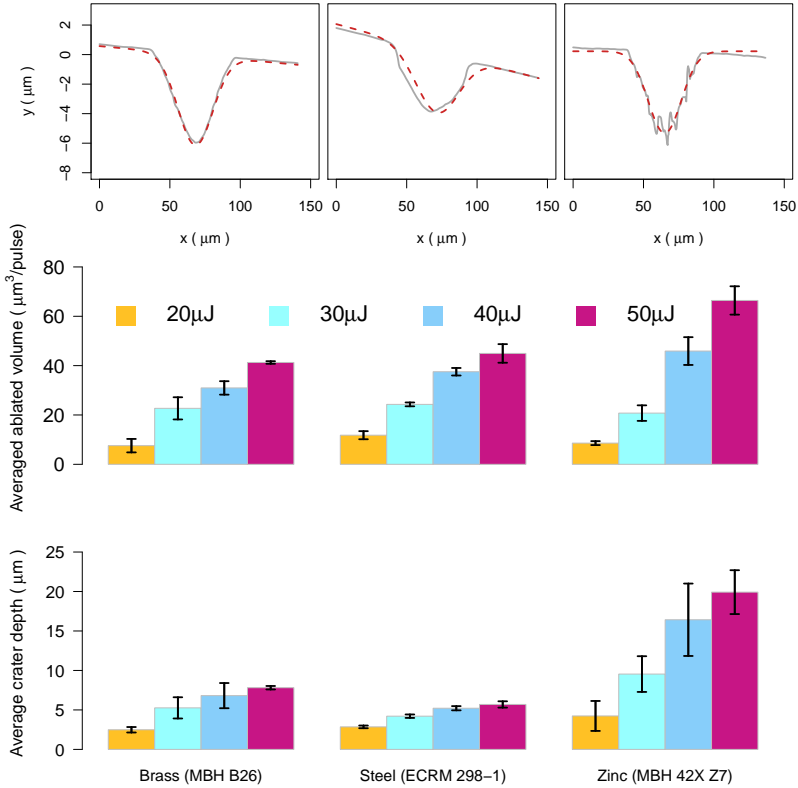
FIGURE 4.2: Confocal microscopy measurements of the crater produced. *Top:* Gray different profiles obtained using 30 μJ pulses. Red: Fitted Gaussian. *Bottom:* Average volume ablated per laser pulse.

The data can be found in table 4.3. For the same laser energy, the averaged crater diameter (Tab. 4.3) did not vary substantially between the sample presented. However an increase in the crater diameter was found for increasing laser fluence. This finding can be explained with the Gaussian shape of the laser employed. With higher energy enough fluence is reached for ablation in a outer part of the laser beam. A linear regression between employed fluence and ablated volume (with correlation coeffi-

cient $r^2 \geq 0.98$, Fig. 4.2) could be fitted for all the sample analyzed. The crater depth however did not show the same linear relationship (with correlation coefficient $r^2 \geq 0.94$, Fig. 4.2).

TABLE 4.3: Crater properties measured by means of CM. The average ablated volumes are given as the average volume of the craters divided by the number of pulses.

	Energy: 20μJ	Energy: 30μJ	Energy: 40μJ	Energy: 50μJ
Average crater depth (μm)				
Brass	2.5±0.2	5.3±0.7	6.8±0.8	7.81±0.01
Steel	2.9±0.1	4.2±0.1	5.2±0.1	5.7±0.2
Zink	4.2±0.9	10±1	16±2.3	20±1
Averaged crater radius (μm)				
Brass	25±1	28±0.3	32±1	33±0.1
Steel	26±2	30±1	31±1	36±0.2
Zink	25±1	27±0.4	30±1	31±1
Averaged vol. ablated per pulse (μm^3/pulse)				
Brass	8±1	23±2	31±1	41.3±0.3
Steel	11.8±0.8	24.3±0.4	37.5±0.8	44±2
Zink	8.6±0.4	20.8±2	46±3	66±3

4.2.2 *Sensitivity*

In figure 4.3, 4.4 and 4.5 the calculated sensitivities for different element calculated using the previous results, can be found. The sensitivity for different isotopes (S_x) with known mass fraction in the sample were calculated using :

$$S_x = \frac{(I_x)}{C_x \times \text{Ab}} \tag{4.1}$$

where I_x is the integrated ion signal of the isotope of interest (counts), C_x is the mass fraction reference value (μg/g) and Ab natural abundance of the analyzed isotope. The isotopes used for the calculation can be found in table 4.4

TABLE 4.4: Isotope evaluated

^{24}Mg	^{27}Al	^{28}Si	^{47}Ti	^{52}Cr	^{55}Mn	^{56}Fe	^{60}Ni
^{59}Co	^{63}Cu	^{66}Zn	^{65}Cu	^{75}As	^{97}Mo	^{107}Ag	^{111}Cd
		^{118}Sn	^{121}Sb	^{208}Pb	^{209}Bi		
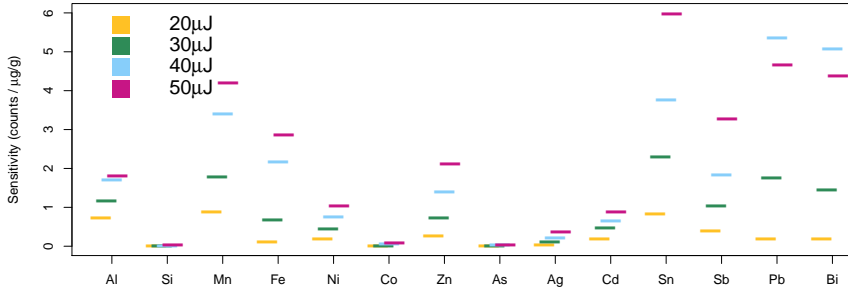
FIGURE 4.3: Sensitivity obtained ablating a brass standard reference material (MBH B26) employing different laser energies.
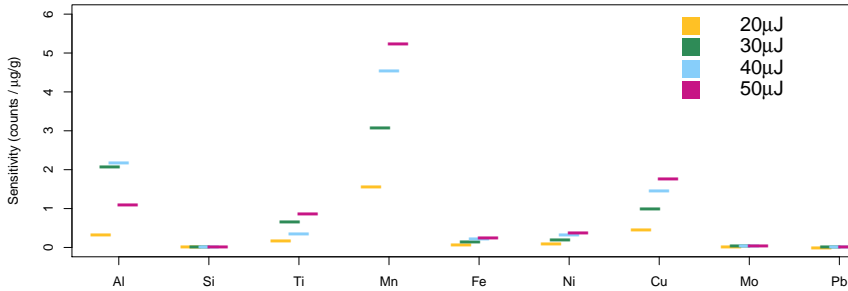
FIGURE 4.4: Sensitivities obtained when ablating a steel standard reference material (ECRM 291-1) employing different laser energies.
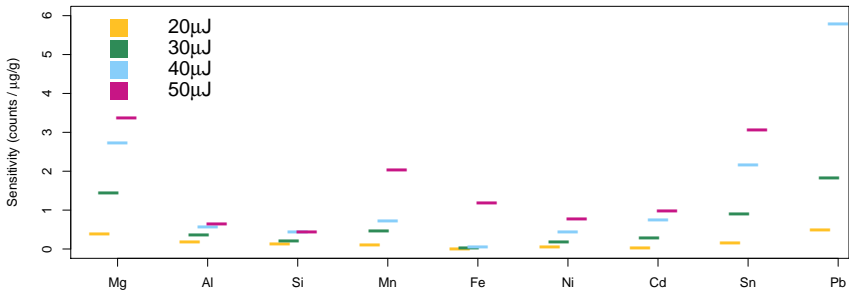
FIGURE 4.5: Sensitivities obtained when ablating a zinc standard reference material (MBH 42X Z7) employing different laser energies. The points are plotted of axis of the element tags to avoid overlapping

It can also be seen that a strong elemental dependence for sensitivity was found within the same sample and in between the matrices. The physical property differences of samples (e.g. surface roughness, absorption coefficient, thermal conductivity, etc) affect how the laser energy is coupled to the sample and therefore the properties of the ejected ions. For a given material, the different physical properties of the elements (e.g ionization potential, boiling point, reactivity, etc) influence the ion formation efficiency as well as the recombination process which ions may undergo in the laser generated plasma. At this stage of the project it can not be distinguished between different ionization process, different recombination process or different detection efficiency of the system. In any case, an increase in sensitivity was observed for all isotopes analyzed in the 3 matrices when laser pulse energy was increased. Exception to this finding are the sensitivities obtained with 50 μJ pulses for Pb and Bi in brass and for Al in steel. The decrease found in the brass sample may be attributed to sample inhomogeneities.

4.2.3   *Relative sensitivity coefficients*

In order to compare the system response to the increase of laser energy, RSC were calculated for the different materials using the equation 1.1. Main component elements were chosen as reference elements, $^{65}Cu^+$ was chosen for brass, $^{52}Cr^+$ for the steel and $^{64}Zn^+$ for the zinc sample. The copper isotope was chosen for continuity with chapter 2, where detector saturation was a major obstacle. The calculated RSC are presented in figure 4.6, figure 4.7 and figure 4.8 for brass, steel and zinc samples respectively.
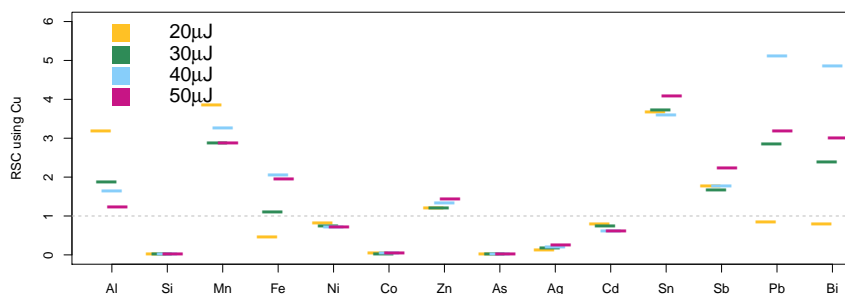
FIGURE 4.6: RSC obtained ablating a brass standard reference material (MBH B26) employing different laser energies.

Substantial variation of the RSC obtained for different laser energy was found for all the matrices. Variation between circa 5% (for Sn) and circa 60% (for Bi, Pb and Cd) from averaged RSC for different energy were found in the case of the brass sample. Variation between circa 20% (for Cd) and circa 160% (for Fe) from averaged RSC for different energy were found in the case of the zinc sample. Variation between circa 2% (for Zn) and circa 70% (for Si) from averaged RSC for different energy were found in the case of the steel sample. From this data was not possible to find an explanation behind this discrepancy, however they show the importance of laser fluence matching. Quantification experiments should be performed using the same laser fluence for the sample as well as using a matrix-matched SRM.
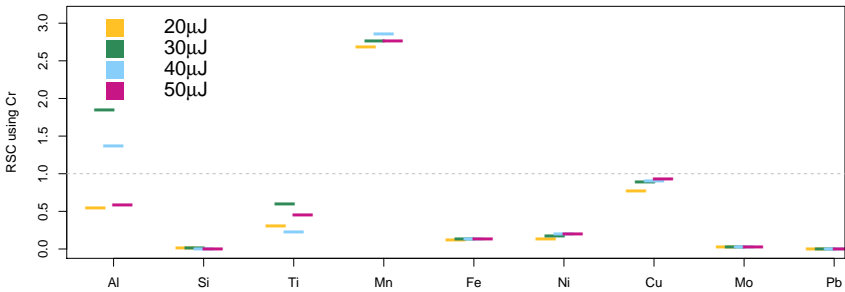
FIGURE 4.7: RSC obtained ablating a steel standard reference material (ECRM 291-1) employing different laser energies.
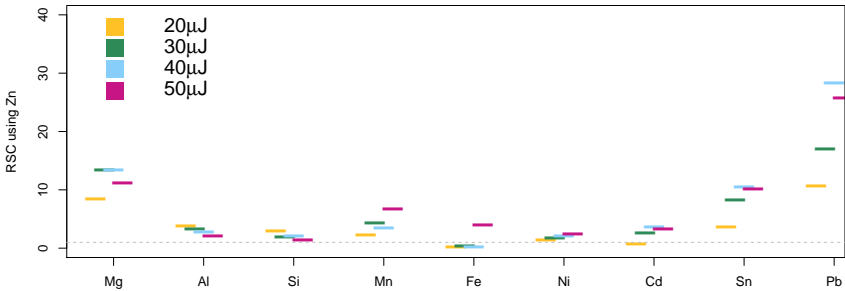
FIGURE 4.8: RCS obtained ablating a zinc standard reference material (MBH 42X Z7) employing different laser energies.

4.2.4   *Quantification of a brass sample of unknown composition*

To assess the quantification capabilities of the fs-LAMS, matrix matched quantification experiments were performed. A standard (MBH 26) and an in-house brass sample with unknown composition were analyzed applying 200 laser pulse (with energy varying (20 μJ corresponding to $\approx$ 0.4

J/cm^2, 30 μJ corresponding to $\approx$ 0.6 J/cm^2, 40 μJ corresponding to $\approx$ 0.8 J/cm^2 and 50 μJ corresponding to $\approx$ 1.2 J/cm^2) and constant operating condition (RF frequency: 5 MHz and the RF amplitude: 20 V_{pp}, funnel pressure: 4 mbar, pressure ablation: 23 mbar). All measurements were done in triplicate. Reference measurements for the in-house brass sample were performed using state of the art LA-ICPTOFMS [172]. Quantification calculation was based on the method of Longerich et al. [173] using the formula:

$$C_x^{sample} = I_x^{sample} \times \frac{C_x^{cal}}{I_x^{cal}} \times \left(\frac{C_{IS}^{sample}}{I_{IS}^{sample}} \times \frac{I_{IS}^{cal}}{C_{IS}^{cal}} \right) \tag{4.2}$$

$$\Rightarrow C_x^{sample} = \frac{I_x^{sample}}{S_x^{cal}} \times \left(\frac{S_{IS}^{cal}}{S_{IS}^{sample}} \right) \tag{4.3}$$

where C, I and S are the mass fraction, the signal intensity and sensitivity for the isotope of interest (x) or the internal standard (IS), measured during the ablation of either a calibration standard (*cal*) or the sample (*sample*). ^{65}Cu was used as internal standard and in both cases a mass fraction of 24.66 % was assumed, corresponding to a mass fraction of 80 % total Cu.
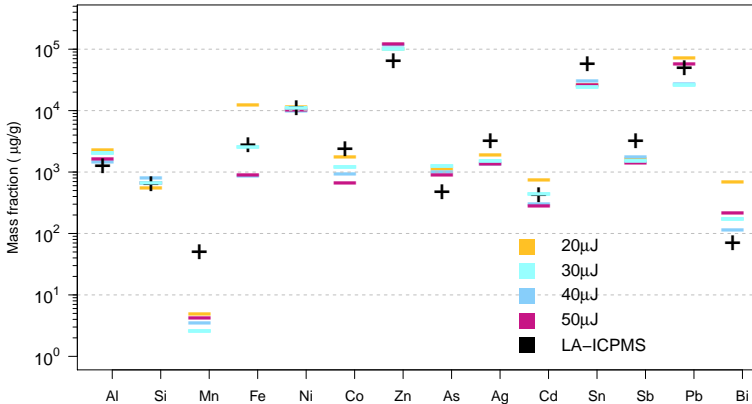
FIGURE 4.9: Mass fraction obtained for an in-house brass sample obtained using fs-LAMS and LA-ICPTOFMS.

The results shown in figure 4.9, represent mass fractions of the elements quantifiable using the chosen standard. In fs-LAMS, the absence of spectral interferences was controlled by isotope pattern matching. An energy dependence of the RSC had to be expected from the previous experiment and the changes in RSC caused the mass fraction determined to vary accordingly. The quantified value obtained with fs-LAMS and with LA-ICPTOFMS measurements can be found in table 4.5. A deviation by up to a factor of 2 was found for the majority of the elements investigated at different energies, with overestimated mass fraction being similarly frequent as underestimated ones. A systematic underestimation of Mn was found for all the energies investigated. The reason may be the presence of an isobaric interference when the SRM was ablated. It was, however not possible to identify a likely candidate in the mass spectrum. The overestimation of Bi may arise as well from an isobaric interference measured only for the in-house brass sample. In any case, the relative sensitivities obtained also with fs-LAMS appear to not be independent on the element investigated. The claims for RSC values close to unity [51] could not be verified in these experiments.

TABLE 4.5: Mass fraction obtained from fs-LAMS measurements and from LA-ICPMS measurements.

($\mu g/g$)	LA-ICPMS	fs-LAMS $20\mu J$	fs-LAMS $30\mu J$	fs-LAMS $40\mu J$	fs-LAMS $50\mu J$
Al	1.21×10^3	2.31×10^3	2.04×10^3	1.44×10^3	1.65×10^3
Si	629	543	678	791	668
Mn	48	5	3	4	4
Fe	2.66×10^3	12.4×10^3	2.55×10^3	881	887
Ni	10.9×10^3	11.5×10^3	11.1×10^3	10.1×10^3	10.1×10^3
Co	2305	1739	1231	945	656
Zn	62.6×10^3	10.3×10^4	10.2×10^4	11.8×10^4	12.3×10^3
As	458	1139	1266	989	897
Ag	3.16×10^3	1.91×10^3	1.50×10^3	1.4×10^3	1.40×10^3
Cd	417	758	447	304	286
Sn	56.4×10^3	26.1×10^3	24.4×10^3	30.0×10^3	26.6×10^3
Sb	3135	1611	1502	1788	1423
Pb	48.5×10^3	71.6×10^3	26.2×10^3	27.4×10^3	56.7×10^3
Bi	67	689	172	115	212

4.2.5 *Isotope ratio precision*

To assess the precision attainable for isotope ratio measurements and the mass bias of the setup, a polished brass SRM (MBH 26) was ablated using 2000 laser pulses (20 μJ, corresponding to $\approx$ 0.4 J/cm^2) and constant experimental condition (RF frequency: 5 MHz and the RF amplitude: 20 V$_{pp}$, funnel pressure: 4 mbar, pressure ablation: 23 mbar). In order to improve signal/background ratios and reduce the contribution from molecular ions, the width of mass channels was decreased from 0.003 to 0.0009 amu for 1H and from 0.318 to 0.096 amu for 238U and the respective averaged transient signals were evaluated. The experiment was done with 5 replicates. The mass calibration was continuously updated during post-processing using the signal of O$_2^+$,^{63}Cu$^+$, ^{56}Fe$^+$, ^{120}Sn$^+$ and ^{208}Pb$^+$, to correct for eventual drift which may have occurred during the measurements. The deviation of isotope ratio from the natural abundance was calculated using the delta notation :

$$\delta = \left(\frac{I(^nX)/I(^mX)}{Ab(^nX)/Ab(^mX)} - 1 \right) * 1000 \qquad (4.4)$$

where I(X) is the averaged signal intensity and $Ab(X)$ is the natural abundance for different isotopes (n and m). In figure 4.10 the deviation of the measured isotopic ratios from the natural abundances, the error propagation based on counting statistics (gray area) and the standard deviation obtained from 5 replicates (dotted line) can be seen. Four isotope pairs (^{65}Cu/^{63}Cu, ^{68}Zn/^{67}Zn, ^{119}Sn/^{117}Sn,^{208}Pb/^{206}Pb) were chosen and for each of them, the deviation from natural abundance was calculated for increasing number of laser pulses (the integration of pulse one to ten, one to twenty, etc). Assuming counting statistics as the dominant source of uncertainty, the precision of the isotope ratios was propagated via the recorded ion signals :

$$RSD^{cs}_{ratio} = \sqrt{(\sqrt{I_1}/I_1)^2 + (\sqrt{I_2}/I_2)^2} \qquad (4.5)$$

where RSD^{cs}_{ratio} is the calculated relative standard deviation (RSD) for the isotope ratio base on counting statistics, I_1 is the sum of integrated ion counts obtained for one isotope and I_2 for the other. From figure 4.10 it can be seen that with accumulation of more than 1000 laser pulses the δ values converge to a value similar for all the isotope ratios. More precisely 24.55 (rsd: 1.4%) for Cu, 24.20 (rsd: 1.8%) for Zn, 26.28(rsd: 1.5%) for Sn and 26.28 (rsd: 2.2%) for Pb.
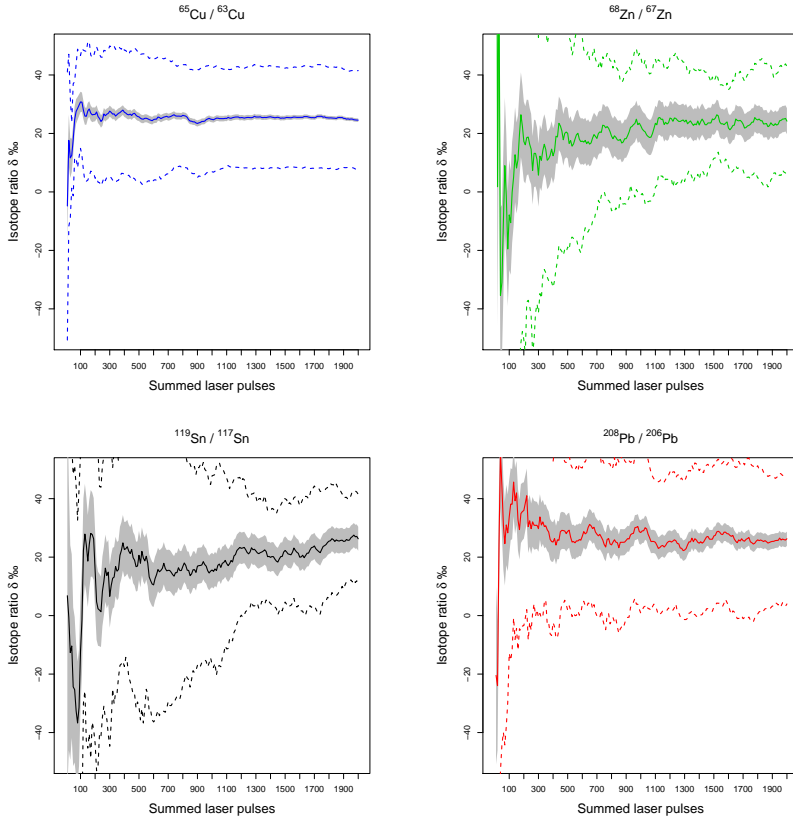
FIGURE 4.10: Isotopic ratio for different isotope pairs in dependence to number of laser pulses integrated. Dashed lines represent the standard deviation of the five replicates. The gray areas show the uncertainty based on counting statistics

These data indicate a generally a positive mass bias, whose magnitude slightly increases with mass of the isotopes studied. From figure 4.10 it can be seen that the uncertainty of the δ-value is not determined from counting statistics, and that additional experimental factors affect the isotope ratio precision. It is interesting to notice that the variability of the δ value for the 5 replicates (dashed lines in figure 4.10) remains substantially larger than the uncertainty based on counting statistics. This indicates that the stability

of either ion generation or ion transfer substantially affects the precision of the analyses.

4.2.6 *Detection efficiency*

To assess the overall performance of the instrument, Detection Efficiency (DE) were calculated using data from section 4.2.2 and 4.2.1 via the formula:

$$DE_x = \frac{I_x}{\text{Nr of atoms}} \rightarrow I_x \times \left(\underbrace{\frac{V_{ablated} C_x \rho_{sample}}{M_x} N_A}_{\text{Nr. of moles}} \right)^{-1} \tag{4.6}$$

where I_x, C_x and M_x are the signal intensity (counts), the isotope mass fraction (μg/g) and the atomic weight (g/mol) of the isotope of interest respectively, $V_{ablated}$ is the measured ablated volume (cm^3), ρ_{sample} is density (g/cm^3) of the metal ablated and N_A is the Avogadro constant . Errors presented the calculated DE were estimated from the standard deviation of both measurements (volume and ion signal intensities) and the density of the metal analyzed. The densities were estimated by averaging the highest and lowest reference value found [174] and using their difference from the mean as uncertainty. The results can be found in table 4.6, table 4.7 and table 4.8.

The DEs were found to differ by up to almost tree order of magnitude difference for the same matrix and same laser fluence (Tab. 4.6, 50 μJ, Si and Bi). However for the majority of the isotopes only a variation between 2 order of magnitude can be found. The highest detection efficiency found is in the range of one ion in each 10^8 atoms ablated for heavy elements (Pb or Bi), when ablating brass and zinc matrices. It is interesting to notice that the DE does not exhibit a clear correlation with laser fluence applied. The decrease in detection efficiencies that were obtained for the highest fluence are currently, at least in part, attributed to the ion optic system used. An indication for this can be seen in figure 4.11 where a photograph of the the ion lens downstream the Einzel lens assembly (Fig. 2.1) is shown. The halo present on the base of this TOFMS entrance lens is attributed to ion deposition and suggesting that that a substantial fraction of the ion beam is deposited at this stage.

TABLE 4.6: Calculated DE for the brass sample (MBH26) for selected isotopes and different energies, obtained from ablation of 200 laser pulses, in brackets the propagated standard deviation from the measurement uncertainty and the estimated density of the material.

Brass	Energy: 20μJ	Energy: 30μJ	Energy: 40μJ	Energy: 50μJ
^{27}Al	1×10^{-09}(19%)	7×10^{-10}(11%)	7×10^{-10}(5.5%)	6×10^{-10}(4.2%)
^{28}Si	1×10^{-11}(49%)	5×10^{-12}(10%)	7×10^{-12}(22%)	9×10^{-12}(2.6%)
^{56}Fe	4×10^{-10}(41%)	8×10^{-10}(83%)	2×10^{-09}(100%)	2×10^{-09}(100%)
^{58}Ni	7×10^{-10}(19%)	6×10^{-10}(11%)	7×10^{-10}(5.5%)	7×10^{-10}(4.7%)
^{59}Co	4×10^{-11}(43%)	3×10^{-11}(41%)	5×10^{-11}(16%)	6×10^{-11}(27%)
^{64}Zn	1×10^{-09}(19%)	1×10^{-09}(11%)	1×10^{-09}(7.9%)	2×10^{-09}(4.7%)
^{65}Cu	9×10^{-10}(21%)	8×10^{-10}(11%)	1×10^{-09}(15%)	1×10^{-09}(11%)
^{75}As	2×10^{-11}(42%)	2×10^{-11}(24%)	3×10^{-11}(42%)	3×10^{-11}(27%)
^{107}Ag	2×10^{-10}(79%)	2×10^{-10}(17%)	4×10^{-10}(19%)	5×10^{-10}(6.8%)
^{111}Cd	1×10^{-09}(49%)	1×10^{-09}(23%)	1×10^{-09}(41%)	1×10^{-09}(30%)
^{118}Sn	6×10^{-09}(23%)	6×10^{-09}(13%)	7×10^{-09}(7.5%)	8×10^{-09}(2.7%)
^{121}Sb	3×10^{-09}(30%)	3×10^{-09}(13%)	3×10^{-09}(18%)	5×10^{-09}(11%)
^{208}Pb	3×10^{-09}(82%)	8×10^{-09}(63%)	2×10^{-08}(83%)	1×10^{-08}(37%)
^{209}Bi	2×10^{-09}(86%)	6×10^{-09}(59%)	2×10^{-08}(94%)	1×10^{-08}(26%)

TABLE 4.7: Calculated DE for the Steel (ECRM298-1) sample for selected isotopes and different energies, obtained from ablation of 200 laser pulses, in brackets the propagated standard deviation from the measurement uncertainty and the estimated density of the material.

Steel	Energy: 20μJ	Energy: 30μJ	Energy: 40μJ	Energy: 50μJ
^{27}Al	4×10^{-10}(23%)	1×10^{-09}(39%)	8×10^{-10}(110%)	4×10^{-10}(33%)
^{28}Si	7×10^{-12}(65%)	5×10^{-12}(18%)	1×10^{-12}(80%)	1×10^{-12}(43%)
^{48}Ti	4×10^{-10}(18%)	7×10^{-10}(45%)	2×10^{-10}(19%)	5×10^{-10}(11%)
^{52}Cr	1×10^{-09}(11%)	1×10^{-09}(6.1%)	1×10^{-09}(6.4%)	1×10^{-09}(7.6%)
^{55}Mn	4×10^{-09}(13%)	4×10^{-09}(6.3%)	4×10^{-09}(7.9%)	3×10^{-09}(7.2%)
^{56}Fe	2×10^{-10}(15%)	2×10^{-10}(5.8%)	2×10^{-10}(6.3%)	2×10^{-10}(7.3%)
^{58}Ni	2×10^{-10}(17%)	2×10^{-10}(6.6%)	3×10^{-10}(9.8%)	3×10^{-10}(8.4%)
^{63}Cu	1×10^{-09}(17%)	1×10^{-09}(7.4%)	1×10^{-09}(8.6%)	1×10^{-09}(7%)
^{98}Mo	9×10^{-11}(15%)	6×10^{-11}(18%)	5×10^{-11}(8.6%)	5×10^{-11}(9.8%)
^{206}Pb	5×10^{-12}(34%)	9×10^{-12}(7.9%)	1×10^{-11}(45%)	8×10^{-12}(12%)

TABLE 4.8: Calculated DE for the zinc sample (MBH 42X Z7) for selected isotopes and different energies, obtained from ablation of 200 laser pulses, in brackets the propagated standard deviation from the measurement uncertainty and the estimated density of the material.

Zinc	Energy: 20μJ	Energy: 30μJ	Energy: 40μJ	Energy: 50μJ
^{24}Mg	7×10^{-10}(7%)	1×10^{-09}(24%)	8×10^{-10}(14%)	7×10^{-10}(22%)
^{27}Al	3×10^{-10}(12%)	3×10^{-10}(11%)	2×10^{-10}(12%)	2×10^{-10}(8.8%)
^{28}Si	3×10^{-10}(30%)	2×10^{-10}(12%)	2×10^{-10}(34%)	1×10^{-10}(30%)
^{55}Mn	5×10^{-10}(38%)	7×10^{-10}(43%)	5×10^{-10}(48%)	1×10^{-09}(120%)
^{56}Fe	2×10^{-11}(140%)	5×10^{-11}(35%)	3×10^{-11}(140%)	6×10^{-10}(170%)
^{58}Ni	3×10^{-10}(120%)	3×10^{-10}(17%)	3×10^{-10}(40%)	4×10^{-10}(67%)
^{66}Zn	2×10^{-10}(27%)	2×10^{-10}(8.9%)	2×10^{-10}(13%)	2×10^{-10}(17%)
^{110}Cd	1×10^{-09}(65%)	9×10^{-10}(15%)	7×10^{-10}(16%)	1×10^{-09}(37%)
^{118}Sn	1×10^{-09}(70%)	3×10^{-09}(18%)	3×10^{-09}(6.6%)	3×10^{-09}(25%)
^{208}Pb	7×10^{-09}(5.2%)	1×10^{-08}(52%)	2×10^{-08}(37%)	1×10^{-08}(20%)
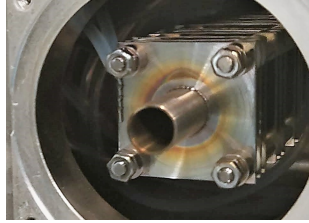
FIGURE 4.11: Entrance lens of the TOFMS employed. A halo is visible on the surface of the electrode.

4.2.7 *Signal stability in single spot fs-LAMS*

To assess the down hole fractionation effect of fs-LAMS, drilling experiments of different standard reference materials were performed using different laser pulse energies (20 μJ corresponding to $\approx$ 0.4 J/cm^2 and 40 μJ corresponding to $\approx$ 0.8 J/cm^2) and constant experimental condition (RF frequency: 5 MHz and the RF amplitude: 20 V$_{pp}$, funnel pressure: 4 mbar, pressure ablation: 23 mbar). Three replicates of each experiment were performed and the evolution of the integrated transient signals averaged. After each experiment the sample position was changed in order to create a new crater. Figure 4.12 shows the normalized signal ratio to ^{52}Cr of different isotopes for different laser pulse energies obtained during continuous

ablation of the steel sample (ECRM298-1), normalized to the ratio maximum.

FIGURE 4.12: Normalized, transient profiles of different signal ratio during continuous ablation of steel reference material (ECRM298-1), using different laser energies. Each point represents the average ion signals from 20 subsequent laser pulses.

^{52}Cr was chosen as reference isotope because it yielded the most intense signal present in the spectra. From the figure it can be seen that laser energy influences the evolution of signal as the crater is formed. With lower laser energy higher variability for Mn and Ni was found. Detector saturation for ^{52}Cr could be excluded since the same trend was found also when the ratio was plotted using ^{53}Cr and, after investigation of ^{52}Cr mass spectral peak. The reason behind this variation are not known. Figure 4.13 shows the normalized signals ratio to ^{63}Cu of different isotopes for different laser pulse energy obtained during continuous ablation of two different brass reference materials (MBH26 and the in-house brass sample used in sect. 4.2.4).

From figure 4.13 can be seen that with higher laser pulse energy (40 μJ) smaller isotope variance for Cu was found (1.3% and 1.7 % for A and C, 0.5 % and 0.6%for B and D) most likely due to the higher amount of material ablated and the corresponding higher signal. All the intensity ratios for the selected isotopes were found to decrease with crater formation, however with different relative magnitude. An increase in ion detection was present during the 200 laser pulses, however the increase was found to be element specific.
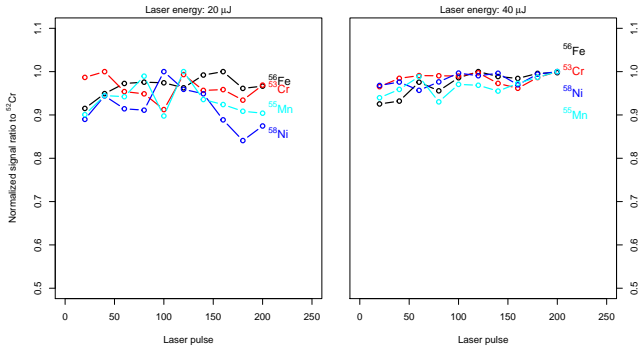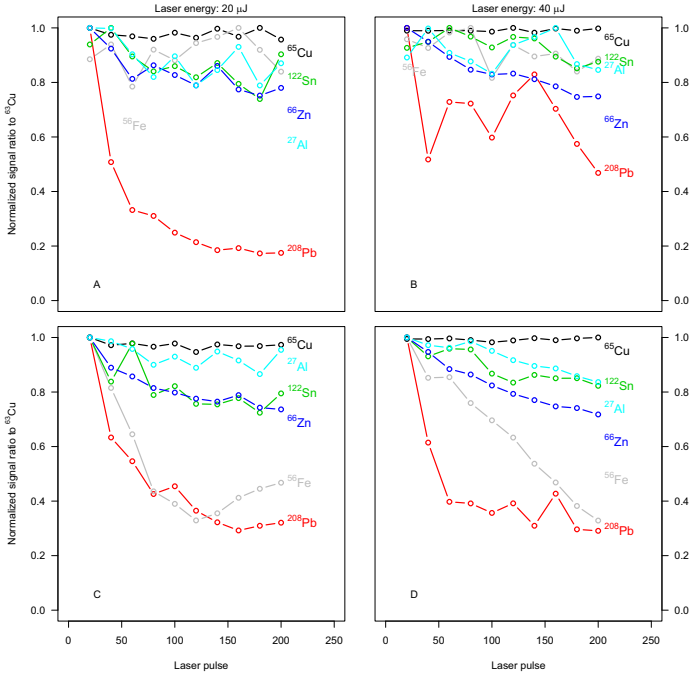
FIGURE 4.13: Normalized, transient profiles of different signal ratio during contin-
uous ablation of two different brass reference materials for different
energy. Each point is the obtained averaging 20 consequent pulses. *A*
and *B)* and in-house brass sample; *C)* and *D)* MBH 26. *Left)* 20 μJ.
Right) 40 μJ

The intensity ratio of Zn, Sn and Al relative to Cu were found to de-
crease with similar magnitude, while the decrease observed for Fe and Pb
was more pronounced. The intensity ratio of Fe relative to Cu shows not
substantial variability during the measurement period, while it decreases
sharply within the first 100 or 200 laser pulses when ablating MBH 26
with 20 or 40 μJ laser energy respectively. Pb on the other hand shows sim-
ilar suppression of the intensity ratios in bot samples with slightly smaller
magnitude in the in-house sample at the higher laser energy. While hetero-
geneity might be partially responsible for the variability observed for Pb,
the similarity in its suppression in all cases studies would suggest that in
fact element fractionation effects do occur also in under these conditions.

4.2.8 *Day to day reproducibility*

To assess the reproducibility of the ion signals, generated using the setup on different days, ion signals and intensity ratios obtained when ablating a brass sample (MBH26) under constant experimental settings (laser energy after the pinhole: 20 μJ corresponding to $\approx$ 0.4 J/cm^2, RF frequency: 5 MHz, the RF amplitude: 20 V$_{pp}$, funnel pressure: 4 mbar, pressure ablation: 23 mbar) are compared in figure 4.14. Between each experiment the sample was removed from the sample holder and polished. Each point represents the averaged ion signal or intensity ratio of the first 200 ablation events at a new surface each.
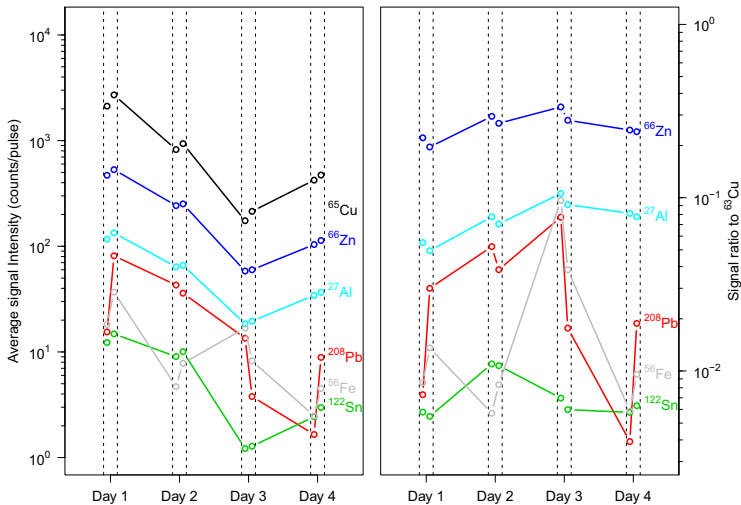
FIGURE 4.14: Signal (*left*) and intensity ratio to ^{63}Cu (*right*) of different isotopes obtained ablating a brass sample (MBH26) under constant experimental condition. Each point represents the averaged signal per pulse obtained using the first 200 laser pulses.

Within this period, differences up to one order of magnitude were found for the signal intensity for all the species (Fig. 4.14). The intensity ratio to ^{63}Cu was also found to be varying from day to day. This variability in raw intensities and intensity ratios is currently considered to result from either

variability of the laser beam profile, which was not investigated further or from the prototype's sample holder, which made adjustment of the sample position and surface orientation relative to the nozzle difficult. Changes in surface angle may cause fractions of the ions generated to be lost at the nozzle walls to varying degree (Fig. 4.15) which directly affects the absolute sensitivity. Changes in sensitivity ratios may then occur from varying expansion velocities of elements of differing volatility [36].
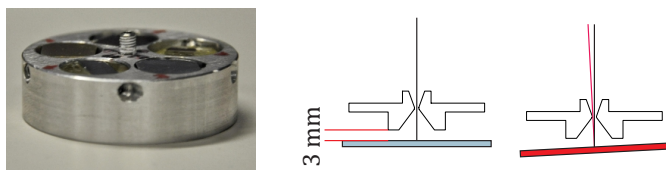
FIGURE 4.15: *Left)* Sample holder. *Right)* Different inclination of the sample (3°). The red lines represent the normal to the sample surface and the black line the normal of the nozzle entrance

4.2.9 *Origin of water clusters and molecular species*

Molecular ions (e.g. O_2^+ and H_3O^+), water ($M_x(H_2O)_y^+$, chapter 2 and 3) and hydrogen adducts were observed at varying levels in the mass spectra. In part it was possible to resolve these species through the mass resolving power of the time of flight instrument or their differences (detector arrival time, Fig. 2.13) from the atomic ions. However, their presence was found to be one major limitation for analytical purposes, making the interpretation of m/Q spectra challenging. In order to investigate the origin of the water, systematic study of the possible source was initiated. Having implemented a gas purifier, contamination of the laboratory supply gas line were excluded as possible source and attention was focused on the setup itself. A polished brass sample (MBH 26) was placed in the sample holder and introduced in the set up. Experiments were performed under standard conditions (1000 laser pulse with energy of 20 μJ corresponding to ≈ 0.4 J/cm^2 , RF frequency: 5 MHz, the RF amplitude: 20 V$_{pp}$, funnel pres-
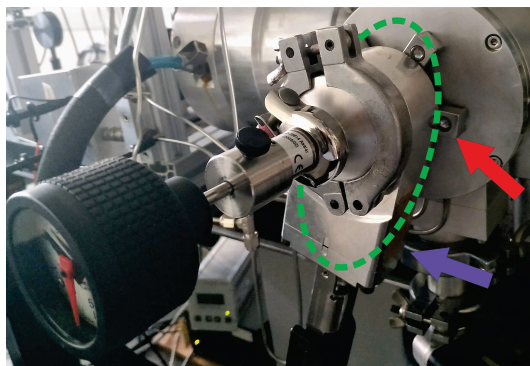
FIGURE 4.16: Picture of the sample introduction arrangement. In green is highlighted the region which was heated using an heat gun, the red arrows highlight the junction between ablation chamber and the 2 of the 4 screws used to tighten it, the violet arrow highlights the gate valve serving as air lock

sure: 4 mbar, pressure ablation: 23 mbar), but between each experiment the sample (and sample holder) was kept in the ablation chamber which was evacuated by closing the buffer gas inlet. During different time intervals, the sample was slightly rotated, in order to form a new crater, and LAMS experiment were performed. After circa 100 minutes the gas line and the ablation chamber (Fig 4.16 green) were heated using a heat gun for circa 10 min. The sample was then left overnight under high vacuum conditions. After one control experiment the sample (and sample holder) was then removed from the ablation chamber and kept for 30 minutes under laboratory condition. It was then reintroduced and an LAMS experiment under standard conditions was performed. To control if manipulation of the setup would result in an increase or decrease of molecular ions, the vacuum gate, which is also serving as ablation chamber was moved (Fig 4.16 violet arrow), LAMS measurements were performed and lastly, the junction between sample introduction and ion funnel was tightened (Fig. 4.16 red arrow). In figure 4.17 it can be seen that the abundance of molecular ions and water cluster ions relative to their parent ions decreased during initial storage in high vacuum. The relative abundance of the Cu_2^+ on the other hand remains practically stable and the O_2^+ signal increased.
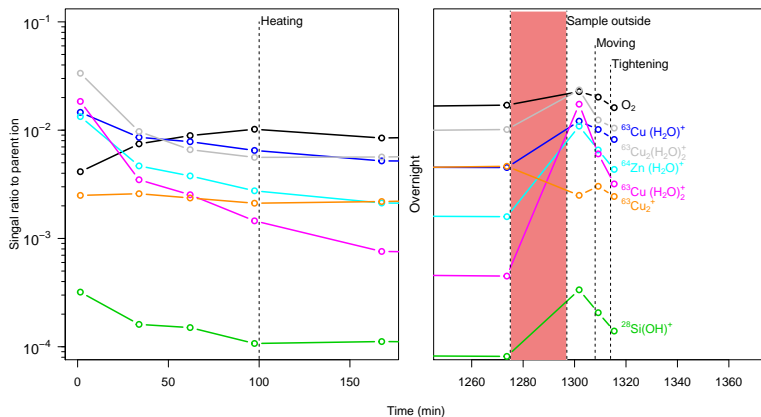
FIGURE 4.17: Cluster and molecular ions signal ratio to parent ion in dependence on time spent of the sample and sample holder in high vacuum. Each point is the obtained averaging 1000 laser pulses. Intensity ratio to the parent ion of the cluster, $^{63}\text{Cu}(\text{H}_2\text{O})^+$, $^{63}\text{Cu}(\text{H}_2\text{O})_2^+$, $^{63}\text{Cu}_2^+$ were normalized using $^{63}\text{Cu}^+$ signal, $^{63}\text{Cu}_2(\text{H}_2\text{O})_2^+$ using $^{63}\text{Cu}_2^+$ signal and $^{64}\text{Zn}(\text{H}_2\text{O})^+$ using $^{64}\text{Zn}^+$ signal. The signal of O_2^+ and $\text{Si}(\text{OH})^+$ were normalized using TIC

Heating the ablation chamber and the gas lines did not substantially affect the relative abundance of the cluster ions. It is interesting to notice significantly higher Cu_2^+ and, $\text{Cu}_2(\text{H}_2\text{O})_2^+$ and O_2^+ abundances after the sample was kept overnight in high vacuum. Looking at the right side of the plot it can be seen that when the sample was exposed to ambient conditions, an increase of all the water/air related species was found. It can be concluded that sample and the sample holder absorbed some ambient water which gets slowly released under low pressure. After slightly moving the sample holder's housing and especially after tightening the mounting screws, the abundances of air-related cluster ions (O_2^+, MH_2O_x^+) drops substantially. This would indicate that even small leaks at the sample holder junctions can cause a substantial alteration of the spectra via the occurrence of molecular and cluster ions.

5

ANALYTICAL CAPABILITIES: fs-LAMS OF THIN FILMS

5.1 EXPERIMENTAL

The experimental setup remained unvaried from the previous chapters. The laser pulse energy was measured after the pinhole aperture before each experiment. Energy loss through the downstream optical components was found to be ≈ 60%, which was considered when calculating the fluence on the sample. The crater dimension was measured using confocal microscopy (CM) (PluNeox, Sensofar, Spain) and the obtained data evaluated using the software Gwyddion [171]. For these experiments a thin-film multilayered standard reference material NIST SRM 2135c and a commercial Hard Disk (HD) were used as test samples. The reference material is composed of five layers of pure Cr alternating four layers of pure Ni on a polished silicon substrate. A nominal thickness of 57 nm for each Cr layer and of 56 nm for each Ni layer is present. A commercial HD was disassembled and a piece of the disk was used as sample. A modified version of the sample holder was used where the sample is fixed by being held against perforated front plate (Fig. 5.1).

FIGURE 5.1: Picture of the sample holder used for this experiments

5.2 RESULTS AND DISCUSSION

5.2.1 *Commercial Hard Disk*

The commercial HD was cut (≈ 1cm x 0.5cm) to fit the sample holder. It was then ablated using laser energy (ranging from 13 μJ to 29 μJ, ≈ 0.3

J/cm^2 and $\approx$ 0.6 J/cm^2 respectively) and the set up was operated with a pressure in ablation region of 18 mbar and a funnel pressure of 2.5 mbar an RF field of 20 V$_{pp}$ at 5MHz. The sample was kept in a constant position, with the laser pulses forming a crater. The change in composition of different layers could be clearly revealed (Fig. 5.2). It was possible to identify Ru and Cr in a very thin superficial layer (Fig 5.3). The signal of the subsequent layer was found to be dominated by Ni showing some traces of Pb (Fig 5.4). The underlying substrate appeared to be composed of an alloy of Al and Mg (Fig 5.5). Through the drilling experiment O_2^+ and $H_5O_2^+$ were detected and were found to follow H_3O^+ signal evolution (Fig 5.2). An increase in their signal was observed when the layer of Al-Mg was reached, the reason of this finding is however not clear. It may be cause by a change in the composition of the laser plasma, leading to changes in ionization pathways as discussed by Moreno-Garcia et al [175].
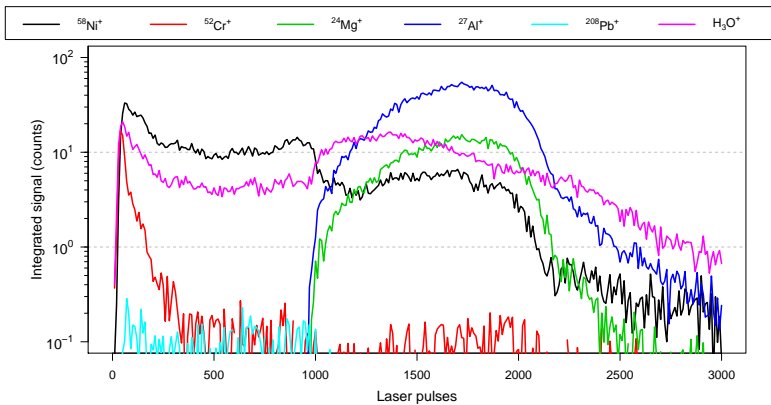
FIGURE 5.2: Measured depth profile of the hard disk sample
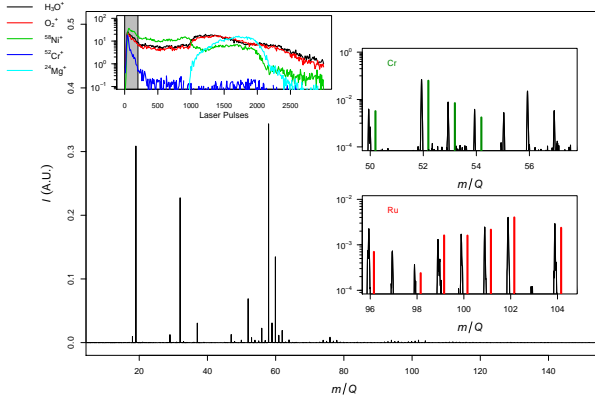
FIGURE 5.3: Mass spectra obtained by integrating for the first 200 laser pulses as indicated by the grey shaded area in the top left insert. The right panels show the mass spectra acquired (in black) and the isotopic pattern (artificially shifted to the right for a better visualization) for the elements identified.
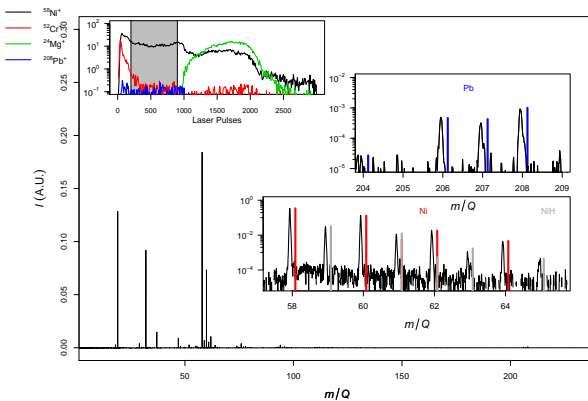
FIGURE 5.4: Mass spectra obtained by integrating from 200 to 960 laser pulses as indicated by the grey shaded area in the top left insert. The right panels show the mass spectra acquired (in black) and the isotopic pattern (artificially shifted to the right for a better visualization) for the elements identified.
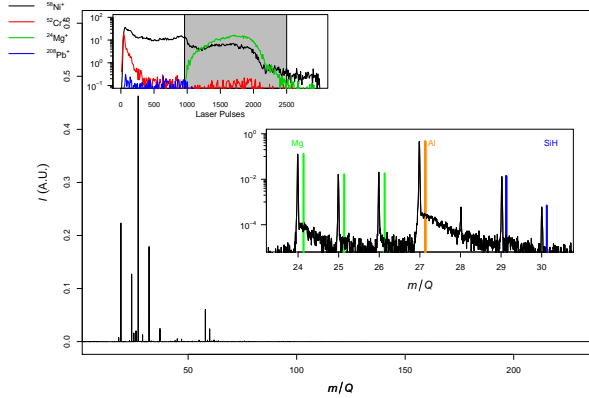
FIGURE 5.5: Mass spectra obtained by integrating from 960 to 2500 laser pulses as indicated by the gray shaded area in the top left insert. The right panels show the mass spectra acquired (in black) and the isotopic pattern (artificially shifted to the right for a better visualization) for the elements identified.

One can furthermore observe the occurrence of Ni in the mass spectra of all the layers. This might be an artifact caused by the gaussian beam profile. At the onset of ablation, the laser may already penetrated the Cr-Ru top layer and remove underlying Ni, while the outer part of the beam continues to remove Ni after reaching the Mg-Al layer.

5.2.1.1   *Energy dependence*

The dependence of ablation rate and ionization efficiency on laser fluence is shown in figure 5.6. Each data point corresponds to an experiment as outlined above, but for varying the laser pulse energy. The ion signal of ^{58}Ni$^+$ was integrated over the course of the entire experiment. Since the thickness of this layer is assumed to be constant across the disk, it can be used to evaluate the change in ion yield with laser pulse energy. The change in ablation rate per pulse, was evaluated by counting the number of pulses needed to reach 10% of the Mg$^+$ signal maximum. An increase in the integrated signal of ^{58}Ni$^+$ with increasing energy can be seen, which seems to follows a sigmoid relationship. On the other hand, less laser pulses are required to ablate the entire Ni layer , following an approximately exponential decay. The ratio between signal and number of pulses (Fig. 5.6 top panel) ultimately represents the ionization/detection efficiency. This ratio

appears to reach a plateau at highest laser energies used. Such a plateau represent the situation where the total number of ions does not increase anymore with higher laser fluence. Because the Ni layer is of a constant depth, it follows that the detection efficiency can also not be enhanced by the laser fluence alone.
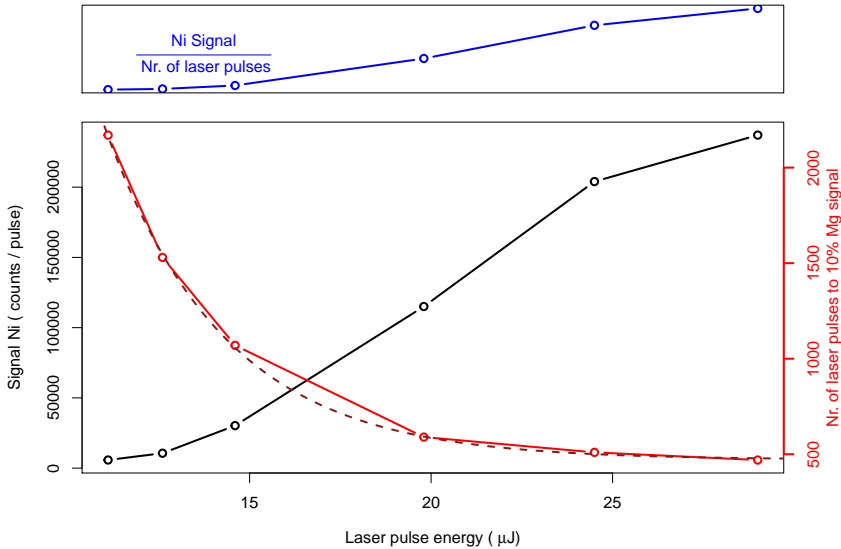
FIGURE 5.6: *Bottom:* Energy dependence of signal and ablation rate. Nickel signal was integrated for the entire drilling. Ablation rate was determined as the number of pulses needed to reach 10 % of the Mg signal. The dotted red line is a fit to an exponential decay. *Top:* the ratio between Ni signal and number of pulses.

5.2.2   *Metal-multilayer standard*

Depth profile measurements of the NIST SRM 2135c, a sandwich structure, were carried out and the results are shown in figure 40. The set up was operated using a RF frequency of 5 MHz, a the RF amplitude: 20 V_{pp}, a funnel pressure: 3.5 mbar and pressure ablation of 23 mbar. The laser energy used was 12 μJ ($\approx$ 0.3 J/cm^2), which represents the lowest fluence yielding ion signal intensities with sufficient signal/noise ratio (> 100).
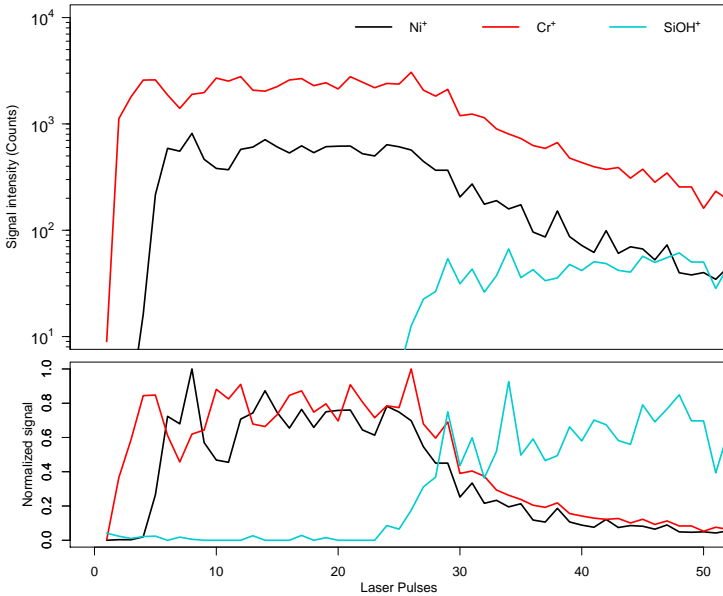
FIGURE 5.7: Measured signal intensity obtained ablating SRM NIST 2135c sample.

In figure 5.7 the abundance corrected signals of Ni$^+$ and Cr$^+$ as well as Si(OH)$^+$, can be seen. During the first pulses only a signal of Cr$^+$ appears, with the Ni$^+$ signal appearing only afterwards. After circa 25 laser pulses, the signal of SiOH$^+$ appears and increases with pulse accumulation. In the upper part of the graph, a 5-fold stronger signal for Cr than for Ni is obtained, indicating difference in ion yield under these conditions. When the signal is normalized to their respective maximum, it becomes easier to identify a recurring pattern. When the ion signals are normalized to the sum of the signal of both, Ni and Cr (Fig. 5.8), the sandwich structure becomes apparent. The top 57 nm Cr layer, was ablated with 4 pulses before penetration, corresponding to an average depth ablation rate of about 15 nm per pulse in the center of the beam. The sharpness of the layer transitions decreased as the crater developed because of the Gaussian beam profile, whereby material from the sloping crater wall is continuously removed.
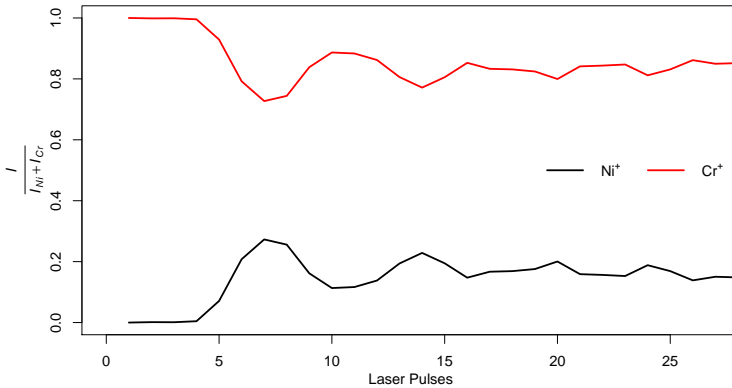
FIGURE 5.8: Signal normalized to the sum of the signal for both Ni and Cr.

This experiments showed depth resolution capabilities similar to the one obtained using fs laser pulses in combination with LA-ICPMS [176], however still one order of magnitude higher then reported for LAMS by Grimaudo et al. [54].

Working with a sample with a defined thickness allow to calculate the detection efficiency obtained with the setup with higher precision compared to CM measurements. For this reason, a the sandwich SRM was ablated using a laser energy of 120μ J, an ion funnel pressure of 2 mbar, a pressure in ablation region of 23 mbar, and employing 5MHz and 20 V_{pp}. The pressure in the ion funnel was reduced aiming at higher ion transmission. Integrating the ion counts for the top layer yielded a detection efficiency (number of ions detected per number of atoms removed) of 3×10^{-8} for Cr. When integrating across the entire depth of the layers, detection efficiencies of 4×10^{-8} for Cr and 0.9×10^{-8} for Ni were obtained, indicating that the overall ion yield does not dramatically change over the crater depth. However, using higher laser fluence, it was not possible to distinguish the individual layers. The detection efficiency thus appears to be up to two orders of magnitude higher than previously obtained for the steel reference material for example (see chapter 4). This, together with the fact that again a significant difference is observed for the detection efficiency of Cr vs. Ni, indicates again that ion yields in LAMS are highly matrix and element dependent also for fs laser ablation.

6

ANALYTICAL CAPABILITIES: fs-LAMS OF GLASSES

6.1 EXPERIMENTAL

The experimental setup remained mostly unchanged from the previous chapters.

In order to increase the laser fluence on the sample surface however, the pinhole (Fig 3.1), was removed and the iris adjusted to an aperture of 1.2 mm. The laser pulse energy at the sample surface was 125 μJ (78 % loss) with an ablation spot of diameter 45 μm, corresponding to a fluence of 8 J/cm^2. The ion optic parameters and TOFMS settings used were kept constant as in the previous studies. Helium was employed as buffer gas. The crater size was measured using confocal microscopy (CM) (PluNeox, Sensofar, Spain) and the obtained data evaluated using the software Gwyddion [171]. For the experiments, two standard reference materials provided by the National Institute of Standards and Technology (NIST 610 and NIST 612) were used. The nominal mass fraction present can be found in table 6.1. The sample holder used was the same as in chapter 5. The SRM used for this studies are soda-lime glasses with nominal composition of 72% m/m SiO$_2$, 12% m/m CaO, 14% m/m Na$_2$O, and 2% m/m Al$_2$O$_3$, which are widely used as standard for LA-ICPMS [177] .

TABLE 6.1: Mass fraction of standard reference material used, NIST 610 and NIST 612. Data from reference [177]

Element	Na$_2$O	Mg	Al$_2$O$_3$	SiO$_2$	K	CaO	V	Cr
	wt %	µg/g	wt %	wt %	µg/g	wt %	µg/g	µg/g
NIST610	13.4	432	1.95	69.7	464	11.4	450	408
NIST612	13.7	68	2.03	72.1	62.3	11.9	38.8	36.4
Element	Mn	Co	Ni	Cu	Zn	Ga	Ge	As
	µg/g	µg/g	µg/g	µg/g	µg/g	µg/g	µg/g	µg/g
NIST610	444	410	458.7	441	460	433	447	325
NIST612	38.7	35.5	38.8	37.8	39.1	36.9	36.1	35.7
Element	Rb	Sr	Y	Nb	Mo	Ag	Cd	In
	µg/g	µg/g	µg/g	µg/g	µg/g	µg/g	µg/g	µg/g
NIST610	425.7	515.5	462	465	417	251	270	434
NIST612	31.4	78.4	38.3	38.9	37.4	22	28.1	38.9
Element	Sn	Sb	Cs	Ba	La	Ce	Pr	Nd
	µg/g	µg/g	µg/g	µg/g	µg/g	µg/g	µg/g	µg/g
NIST610	430	396	366	452	440	453	448	430
NIST612	38.6	34.7	42.7	39.3	36	38.4	37.9	35.5
Element	Sm	Eu	Tb	Dy	Ho	Tm	Yb	Lu
	µg/g	µg/g	µg/g	µg/g	µg/g	µg/g	µg/g	µg/g
NIST610	453	447	437	437	449	435	450	439
NIST612	37.7	35.6	37.6	35.5	38.3	36.8	39.2	37
Element	Re	W	Tl	Pb	Bi	Th	U	
	µg/g	µg/g	µg/g	µg/g	µg/g	µg/g	µg/g	
NIST610	49.9	444	59.6	426	384	457.2	461.5	
NIST612	6.63	38	14.9	38.57	30.2	37.79	37.38	

6.2   RESULTS AND DISCUSSION

The ablation of the NIST glasses was investigated to estimate the setup capabilities when higher laser fluence are employed. Figure 6.1 shows ablation craters produced in a polished NIST 610 (left) and unpolished NIST 612 (right) after 800 laser pulses. The craters exhibit an approximately circular shape of (d $\approx$ 45 µm) and signs of material re-deposition are in par-

ticular visible for NIST SRM 610 and similar to what has been observed in LA-ICPMS using He as carrier gas [178] . The depth of the crater inside was unfortunately not accessible by confocal microscopy.
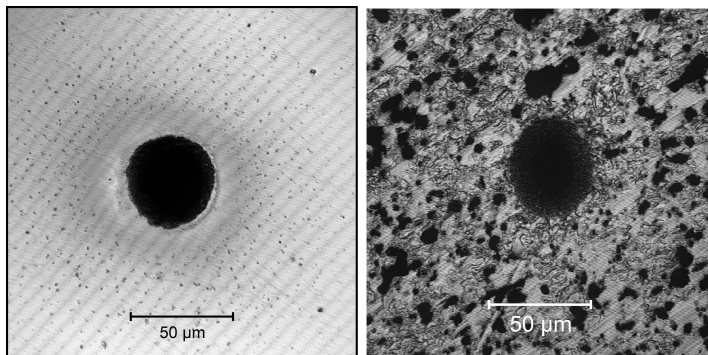
FIGURE 6.1: Picture of the crater formed by the ablation of NIST 610 (*left*) and NIST 612 (*right*)

6.2.1 *Transient structure and composition of the different time regimes*

NIST 610 and 612 were ablated with 800 laser pulses and with standard operating setting (RF frequency: 5 MHz and the RF amplitude: 20 V_{pp}, funnel pressure: 4 mbar, pressure ablation: 23 mbar).

Two different regimes were found as crater formation takes places for both sample. In figure 6.2 the evolution of the transient signal with increasing number of pulses obtained during ablation of NIST 610 is shown. It can be seen that ion signals arising from the first 50 ablation events (insert A) were almost exclusively consisting of alkali metals (Na, Rb and Cs), whereas other species including the sample matrix were barely detected. The initial transient signals appeared to consist of two distributions, which peaked near 0.6 and 1.3 ms after the laser pulse. The second regime of ablation (from 50 to 200 pulses, insert B) showed different characteristics: the transient signal was dominated by slower ions (reaching the detector 0.8 ms after the ablation event) and other species beside alkali metals were detected. The signal of alkali metals was found to peak slightly earlier than other atomic ions. This would indicate that there is still different populations of ions but the temporal separation is small. The sensitivities obtained for the two regions are discussed in the next section.
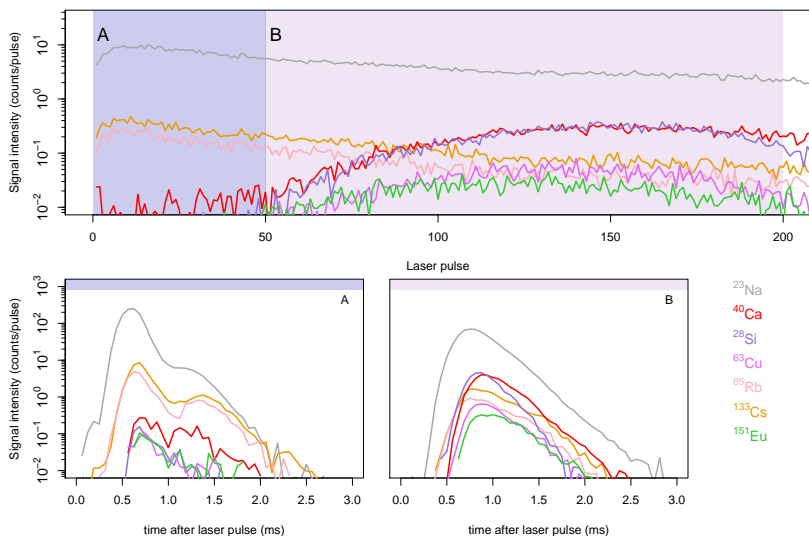
FIGURE 6.2: *Bottom:* Averaged transient signal obtained during different stage of ablation (averaged are 1-50 pulses *(left)* and 51-200 pulses *(right)*). *Top:* Signal evolution during continuous ablation. Average of 5 repetitions.

6.2.2 *Sensitivity*

In figure 6.3 isotope abundance corrected sensitivities for NIST 610 and NIST 612 are shown. The sensitivity was calculated using the formula:

$$S_x = \frac{(I_x - I_{BG})}{C_x \times Ab} \qquad (6.1)$$

where I_x is the integrated peak intensity (cps), I_{BG} is the integrated intensity of an m/Q channel where no ions were expected (cps), C is the concentration reference value (μg/g) and Ab is the natural abundance of the isotope. The intensity used as proxy for the background was an average of the mass channels at 1 m/Q, 2 m/Q, 13 m/Q,14 m/Q, 22 m/Q and 244 m/Q where no ion detection was expected. The signal present in these mass channels corresponds to the signal arising from stray ions and can be therefore used to estimate the instrumental baseline during the ablation process, since practically no ions occurred in instrumental background

without ablation. Knowing the instrumental background it is possible to differentiate between analyte signal and instrumental noise. To convert counts obtained from the experiments to cps, only the measurement time (5 ms) for each laser pulse was taken in account, since no data acquisition is present in the dead time periods between laser pulses (95 ms).

TABLE 6.2: Isotopes evaluated

^{23}Na	^{24}Mg	^{27}Al	^{29}Si	^{39}K	^{42}Ca
^{51}V	^{52}Cr	^{55}Mn	^{59}Co	^{60}Ni	^{66}Zn
^{63}Cu	^{69}Ga	^{72}Ge	^{75}As	^{85}Rb	^{88}Sr
^{89}Y	^{93}Nb	^{97}Mo	^{107}Ag	^{111}Cd	^{115}In
^{118}Sn	^{121}Sb	^{133}Cs	^{137}Ba	^{139}La	^{140}Ce
^{141}Pr	^{146}Nd	^{147}Sm	^{151}Eu	^{159}Tb	^{163}Dy
^{165}Ho	^{169}Tm	^{172}Yb	^{175}Lu	^{183}W	^{185}Re
^{205}Tl	^{208}Pb	^{209}Bi	^{232}Th	^{238}U	

The isotope selection presented in table 6.2 was made after carefully checking the isotopic pattern for potential spectral interferences, apart from the mono-isotopic elements or those with one highly abundant isotope (V, Lu).

Sensitivity was calculated separately for regimes A and B as shown in figure 6.2. Figure 6.3 summarizes the elemental sensitivities obtained for both SRMs and within regions A and B in figure 6.3, top panel. Common in both regimes is that highest sensitivities obtained for alkali metals. Within the first pulses (top Fig. 6.2, A) many of the elements presents NIST 612 were not detected, and the majority of analytes showed only low ion signals resulting in lower sensitivity for both samples. After the first 50 pulses the signal of most of the elements was found to be present and the sensitivity between the two samples did not vary substantially. Exceptions are, however, the more refractory elements like La, Ce, Th or U, who exhibit about an order of magnitude higher sensitivities for SRM NIST 612. High inter-elemental variation (e.g. up to 3 orders of magnitude between Si and K) was found for the sensitivity obtained in both glasses.
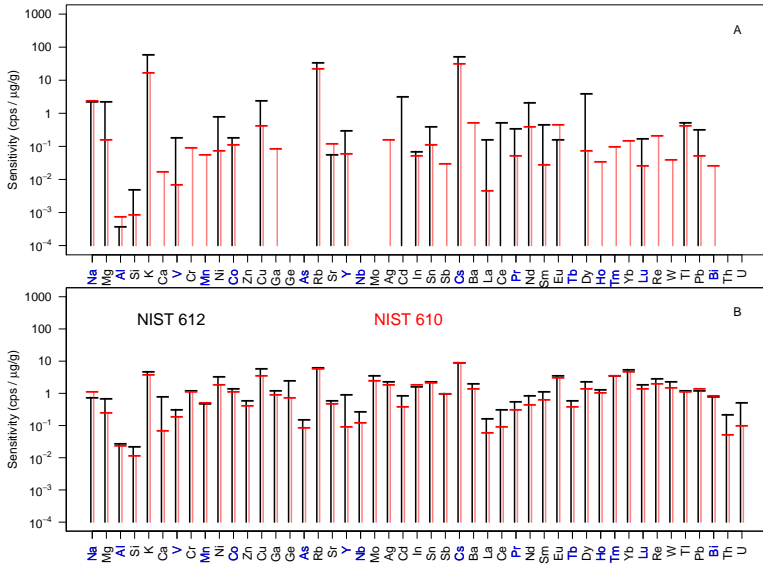
FIGURE 6.3: Sensitivity obtained ablating NIST 610 and NIST 612 for the two different region. The monoisotopic species are highlighted in blue. *Top:* averaged are 1-50 pulses *Bottom:* averaged are 51-200 pulses). Average of 5 repetitions.

The dependence between the sensitivity obtained and the physical properties (boiling point, ionization potential) of the investigated elements can be found in fig. 6.4. The physical properties investigated were chosen to find relationship to charge transfer process (ionization potential), gas phase and plasma process (boiling point) and atomic properties (ionization potential). The highest sensitivities were obtained for elements with low first ionization energy. The dependence is however not unique and other factors like vaporization and dissociation energies must be considered to play an important role as well.
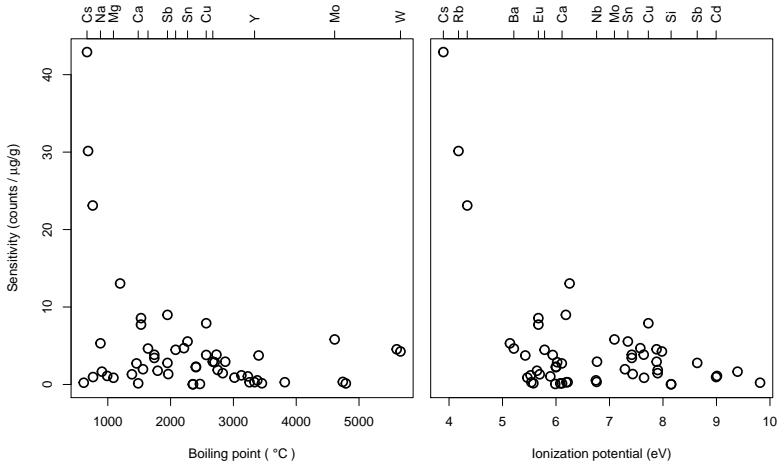
FIGURE 6.4: Sensitivity (for Fig. 6.2, Regime B) in dependence on boiling point and ionization potential of the element plotted, for NIST 610

6.2.2.1   *Relative sensitivity coefficients*

The difference in sensitivity found between the two samples analyzed, was further investigated and in figure 6.5 the ratio of the sensitivities, Relative Sensitivity Coefficient (RSC) and relative sensitivity to total ion current (TIC) are shown. As an example, the RSCs were calculated using Na as internal standard, while TIC-normalization was made relative to the sum of all ion signals in the evaluated mass spectra (baseline and clusters included). For quantitative analyses an RSC of one would allow for accurate determination of the element mass fraction. As can be seen, however, the RSCs relative to Na span over a range between 0.1 for the more oxophilic elements or elements with high ionization energies to 1.5 for Mo. Many elements show still RSC values between 0.75 and 1.25, which might allow for semiquantitative assessment of glasses and minerals. Normalization to the TIC generally leads to ratios lower than for the RSCs, which results from the fact that the higher abundance of trace elements leads to an increase in ions detected in the spectra.
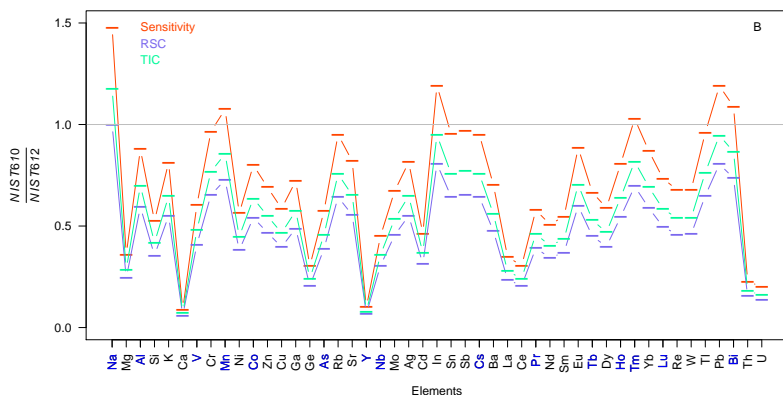
FIGURE 6.5: Ratio between sensitivity, RSC and TIC normalized sensitivity for NIST 610 and NIST 612 for the signal obtained in the second regime (Fig. 6.2, Regime B)

6.2.3 *Limit of detection*

Limits of detection (LOD) are the smallest quantity of analyte that is significantly higher from the blank signal, it was here estimated using the formula:

$$LOD = \frac{3 \times \sigma_{BG}}{S_x} \tag{6.2}$$

where S_x is the average sensitivity of the analyte and σ is the standard deviation of the background obtained during the different replicate of the experiments [173]. LODs obtained from the ablation of NIST 610 and NIST 612 can be found in Fig 6.6. It can be seen that the ablation of NIST 612 frequently resulted in lower limit of detection with exception of Na, Mn, Mo, In, Sb, Tm, Pb and Bi. For reasons outlined before, the highest variability between the samples was found for Mg, Ca, Y, Th and U. For both samples the lowest LODs reachable were found for alkali metals (K, Rb and Cs) reaching tens of ppb.

Having used NIST 610 and NIST 612 as sample, allows for comparison with state of the art LA-ICPTOFMS. Comparable LODs were found only in the case of alkali metals, otherwise it was found that fs-LAMS yielded two orders of magnitude higher LODs. [172]
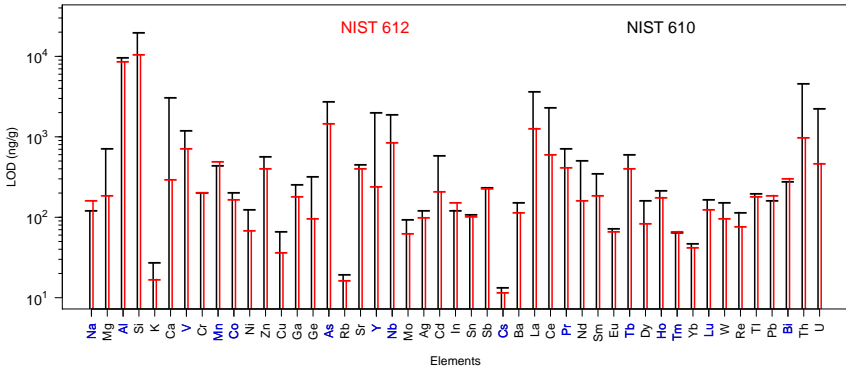
FIGURE 6.6: Limit of Detection (LOD) calculated for the two SRM using data obtained from the second regime of ablation

6.2.4   *Quantification of NIST 612 using NIST 610 as standard*

To assess how much the difference in sensitive would affect the quantification capability of the set up, NIST 612 was quantified using NIST 610 as reference material and either Na, Al, Si or Ca as internal standard. The elements' mass fractions were calculated using the formula:

$$C_x^{sample} = (I_x^{sample} - I_{BG}) \times \frac{C_x^{cal}}{(I_x^{cal} - I_{BG})} \times \left(\frac{C_{IS}^{sample}}{(I_{IS}^{sample} - I_{BG})} \times \frac{(I_{IS}^{cal} - I_{BG})}{C_{IS}^{cal}} \right)$$

where C, I and S are the mass fraction, the signal intensity and sensitivity for the isotope of interest (x) or the internal standard (IS), obtained in the ablation of either a calibration standard (*cal*) or the sample (*sample*) and I_{BG} is the average intensity of the background (defined as in section 6.2.2). A nominal mass fraction of 13.7 % for Na_2, of 1.95 % for Al_2O_3, of 72.1 % for SiO_2 and of 11.9 % for CaO were assumed.

In Figure 6.7 calculated mass fractions for different elements in NIST 612 can be seen. Using Ca as internal standard resulted in the smallest variance between the samples. Still deviation ranging from 5 % to 120 % between nominal value and calculated value were found (Tab. 6.3).
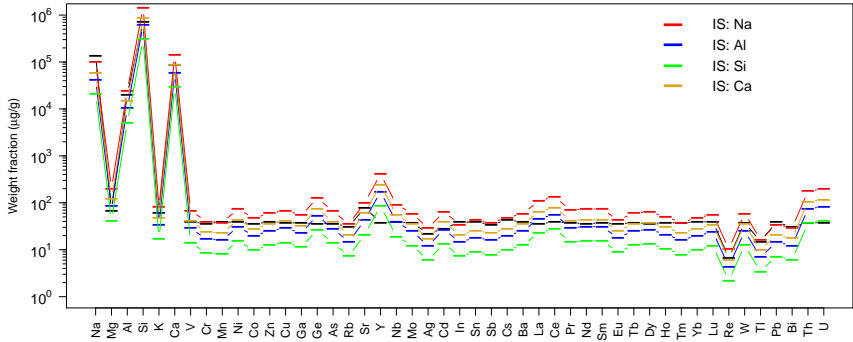
FIGURE 6.7: Calculated mass fraction for NIST 612 (red) using NIST 610 as standard and either Na (red), Al (blue), Si (green) or Ca (darkyellow) as internal standard. In black the nominal mass fraction in NIST 612.

The highest deviation was found for Y,, where a more than 5 times higher mass fraction was obtained. It is most likely caused by a spectral interference, which could, however, not be identified.

TABLE 6.3: Calculated mass fraction and deviation from nominal value for the calculated mass fraction in NIST 612 using Ca as internal standard

Element	Na	Mg	Al	Si	K	Ca	V
Mass (μg/g)	5.86×10^4	120	1.46×10^4	8.67×10^5	48	8.50×10^4	4.1
Deviation	-57 %	76 %	-28 %	20 %	-22 %	0 %	4.8 %
Element	Cr	Mn	Ni	Co	Zn	Cu	Ga
Mass (μg/g)	24	23	44	28	36	41	32
Deviation	-35 %	-41 %	12 %	-21 %	-8.5 %	7.9 %	-12 %
Element	Ge	As	Rb	Sr	Y	Nb	Mo
Mass (μg/g)	75	39	21	60	243	55	35
Deviation	110 %	10 %	-33 %	-23 %	530 %	40 %	-5.9 %
Element	Ag	Cd	In	Sn	Sb	Cs	Ba
Mass (μg/g)	17	38	21	26	23	28	35
Deviation	-22 %	37 %	-47 %	-34 %	-35 %	-34 %	-9.9 %
Element	La	Ce	Pr	Nd	Sm	Eu	Tb
Mass (μg/g)	65	80	41	44	44	25	36
Deviation	81 %	110 %	9.3 %	24 %	16 %	-29 %	-5.1 %
Element	Dy	Ho	Tm	Yb	Lu	Re	W
Mass (μg/g)	38	30	23	29	34	6	35
Deviation	7.2 %	-21 %	-39 %	-27 %	-14 %	-6.8 %	-6.9 %
Element	Tl	Pb	Bi	Th	U		
Mass (μg/g)	10	21	18	105	1		
Deviation	-34 %	-47 %	-42 %	180 %	210 %		

7

ANALYTICAL CAPABILITIES: CONCLUSION

Employing different laser fluences it was possible to ablate and analyze the element content of different materials (metals and glass). Brass, steel and zinc samples were ablated using laser fluences between 1 and 2.5 J/cm^2 and an approximately linear dependence of ablated volume on laser energy was observed for these metals. The corresponding sensitivities increased in concert with the laser energy, but the absolute sensitivities (proportional to the detection efficiencies) did not show substantial variations in these experiments. When ablating thin films from a computer hard disk for example, the ion yield from one specific layer, which was assumed to be homogeneously thick, was found to increase with laser energy applied. This indicates that the detection efficiencies of the new LAMS setup still follow the expected trend of increasing ion yield with higher laser fluence as was reported before [52]. In absolute terms however, detection efficiencies were unexpectedly low in all the studies for the metal samples. Values ranged from 10^{-12} for Si for example to 10^{-8} for the most sensitive elements Bi and Pb. When ablating a well-defined multi-layer sandwich structure the detection efficiencies for Cr and Ni were found to show the same dependence and were increased by more than an order of magnitude when changing from low fluence for depth profiling to high fluence laser ablation. Still detection efficiencies need to be improved by at least two orders of magnitude to become competitive to established highly sensitive techniques as LA-ICPMS or SIMS for example.

In all cases studied, higher ion signals could be obtained when increasing the laser fluence, while element- and matrix dependencies were found in terms of sensitivity and detection efficiency. Even relative sensitivity coefficients appeared to vary substantially between different materials and even within the same matrix. Comparing quantification results for brass samples using the same reference material to calibrate fs-LAMS and state-of-the-art LA-ICPTOFMS yielded differences in the resulting mass fractions of up to ten times, depending on the fluence used for the fs-LAMS experiments. The highest differences occurred when using the lowest fluence and for mono-isotopic elements (As and Bi), which may be a result of not-identified spectral interferences in combination with low analyte sensitivities. Nonetheless most elements could be analyzed with an agree-

ment of less than a factor of two between both methods when the highest laser fluence was used. Quantification of trace and ultra-trace elements using the LAFU source was always affected by substantial abundances of cluster ions from the major components in the sample and also water adducts. They can be partly resolved by the mass resolving power of the time-of-flight instrument used but lead to increased baseline signals and thus impair the specificity of the signals measured. Generally these clusters were found to be attenuated by using higher pressure in the ion funnel but the abundance of the water adducts appears to be to great extent resulting from water vapor adsorbed on the surfaces of the sample holder and the samples themselves. Additionally leakage of ambient air through imperfectly sealed hardware junctions seemed to increase the abundance of these spectral interferences substantially. Overnight evacuation of the sample chamber and heat-assisted evaporation of the water from the surface did reduce the abundance of water clusters notably. A better isolation from ambient air would be required to minimize its contribution.

The evolution of the ion signals for single spot ablation experiments showed that, depending on the sample material and even amongst different brass samples, there was a significant change of the ion yields of different elements as the laser crater forms. In brass a strong depletion of for example Fe, Zn and Pb was observed (the latter may be related to heterogeneous distribution too) which could partly be mitigated at higher laser fluence. In the steel sample on the other hand this variation was much smaller.

The evaluation of the ion signal for such an experiment revealed that the crater depth does not have a significant influence the isotope ratios measured. Intensity ratios for matrix- and trace-element isotopes were found to converge to a relatively stable mass discrimination of between 6 and 6.5 permil per amu. The precision of the within-run ratios, as estimated from counting statistics was however always smaller than the reproducibility of the isotope ratio measurements, indicating that not only the ion currents registered are relevant for the precision of the measurements. In general however, the mass discrimination observed in these experiments was substantially smaller than commonly observed in ICPMS.

The rapid acquisition and comprehensive description of the mass spectra for individual laser pulses using the TOFMS makes the LAFU source very well suited to study depth profiles of unknown materials. As an example it could unambiguously be proven that the active medium of a conventional computer hard disk tested consisted of a thin top layer of a Ru/Cr mixture (eventually in a multi-layer arrangement, which could however not

be resolved) that was not expected. Deeper layers were then identified as mostly Ni on a substrate of a Mg/Al alloy. Forensic applications where no prior knowledge about the composition of a given material is available will thus benefit from such analyses. The actual depth profiling capabilities were finally evaluated using a defined multi-layer Cr-Ni sandwich, where up to nine individual layers of < 100 nm thickness could be identified. The depth resolution decreases with depth however due to the Gaussian energy profile of the fs-laser used. Finally also glass reference samples, which were difficult to analyze using the LAFU source with ns-LA could be ablated with the new fs-LAFU setup. The two NIST SRM 610 and 612 could successfully be ablated and the corresponding ion signals registered. In contrast to the metals analyzed before however, the glasses showed a highly particular signal evolution during single spot ablation experiments. During the very first laser pulses practically only alkali metal ions could be registered, while other elements, including matrix components were only of minor abundance in the spectra. Only after sufficient pulses were applied, the remaining elements could be identified in the mass spectra with a steadily increasing signal intensity. At the same time the transient profiles observed in the ion signals for each laser pulse changed from a situation exhibiting what appears to be two distinct ion energy populations to a more common peak profile that corresponds to an intermediate ion energy. The origin of this particular behavior is not clear however. The initial absence of isotopes with higher ionization energies would indicate that the laser pulse energy is only poorly coupling into the material and desorption/ionization is the dominating process for the first pulses. After a certain incubation time ablation sets in and the entire sample material appears in the spectra. It would thus be interesting to see if such a behavior persists in even a shorter laser wavelength, which should more efficiently be absorbed by the material shows a similar trend. Quantification experiments using the glasses were thus not straightforward. Yet the analyte sensitivities were found to be relatively comparable for the second part of the ablation experiment. Exceptions were found mainly for highly oxophilic elements (e.g. Th), whose sensitivities obtained for the glass with higher mass fraction (NIST SRM 610) were found to be substantially lower. This directly translated to greater deviations in the RSCs and quantification results when using NIST 610 for calibration and NIST 612 as unknown. Nonetheless it could be shown that the majority of trace elements studied could be quantified with a deviation from the reference value of less than 50% using Ca as internal standard.

The experiments presented here certainly indicate that the LAFU source as it has been established during the project has a true potential to serve as a sampling and detection tool for element- and isotope specific analyses. The figures of merit are currently limited by its low detection efficiency and abundant molecular ions which both affect the quantification possibilities to some extent. There is, however, light with respect to the minimal material consumption and promising depth profile resolution together the comprehensive description of the mass spectra. The current limitations are to a great extent considered to be caused by the hardware currently available and the following chapter will describe the concept for an improved source.

8

INSTRUMENT IMPROVEMENT

During this first characterization of the prototype major limitations where encountered. Firstly, the physical dimensions required the use of a focusing lens with a focal length of 250 mm, to pass the beam through the quadrupole deflector and the ion funnel (see Fig.2.1 chapter 2). Using this configuration, it was not possible to produce ablation spots with a diameter $< 40 \ \mu m$. This limited not only the attainable spatial resolution, but also only allowed for comparably small laser fluences to be employed. A smaller beam diameter should allow for higher fluence to be achieved, which was found increase the detection efficiency (chapter 5.2), while lowering the total mass ablated. A second limitation resulted from the substantial abundances of molecular ions (in particular water adducts) present in the mass spectrum. Based on experiments described in chapter 2,3 and 4, and experience from earlier projects in the group, the origin of the water is considered to be the inner surfaces of the ablation region. Aluminum was previously found to increase the abundance of water in LA-GDTOFMS experiments [179]. Additionally, the used sample holder may cause additional gas leaking into the ablation region (Chapter 4). Finally, the positioning of the sample relative to the incoming laser beam was identified a major source of non-reproducible results. The manually operated rotating feedthrough used to select the position of the sample holder relative to the CD-nozzle aperture only allowed ablation experiments along a curved line, making sequential experiments time consuming and error prone (e.g. by accidentally changing the distance between sample and CD nozzle too). The distance to the CD nozzle could furthermore only be set using a screw, which made a precise adjustment of the sample position challenging. To mitigate the above mentioned limitations and at the same time enabling controlled rastering a sample surface for image generation a remodeling of the setup was done and a new sample introduction was designed. It was decided to use a translation stage, where the sample can be positioned accurately and moved within a user defined region. Furthermore, the sample orientation was changed to a horizontal arrangement, to avoid complicate sample fixation strategies. A sealed chamber holding a compact, computer controlled 3-D translation stage was developed where the focal and lateral positions can be adjusted at sub-μm accuracy. This allows for a more re-

producible targeting of larger areas of a given sample. A schematic view is shown in figure 8.1. The sample holder and 3D stage are placed on a tray inside the vacuum housing that can be completely removed from the LAMS unit for sample change. In order to reduce the abundance of residual water on the sample chamber walls, all interior aluminum surfaces are anodized with gold.

3 axis transalitional stage
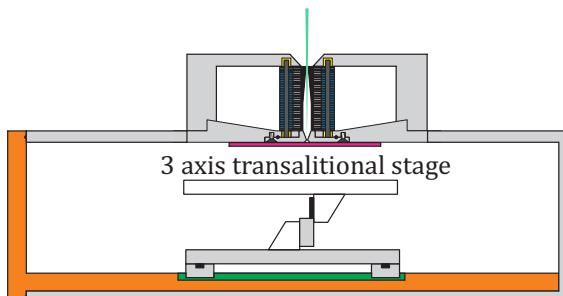
FIGURE 8.1: Schematic view of the new ablation chamber, CD-nozzle and ion optics arrangement for the LAMS instrument. The orange part indicates the removable tray carrying the 3D sample stage. Before removal of the stage, the CD-nozzle is blocked by a slide valve shown in pink.

To obtain smaller ablation spots a lens with shorter focal distance had to be implemented. To do so, the ion optics arrangement had to be modified in order to reduce the distance between the sample and the optical lens.

The new setup consists of a ring electrode (divided into 4 segments), 2 extraction cones and corner electrode (Fig. 8.2). This arrangement was inspired by the ReflexION "ion mirror" used in the PlasmaQuant® ICPMS (Analytic Jena) firstly developed by Kalinitchenko for the former Varian ICPMS [180]. This electrode arrangement produces a parabolic electrostatic field capable of reflecting ions by 90° and focusing them to the entrance aperture of the TOFMS. By controlling the applied voltage, it is possible to shape a parabolic electric field for deflection and focusing ions with minimum chromatic abberation, while the 4 segments can be used to steer the ion beam along x, y and z-axis (Fig. 8.2). The open structure of the lens system also allows photons (from the laser) and neutrals (from the buffer gas) to pass straight through it. A further advantage of this configuration is that the ion path can be made very short [180].
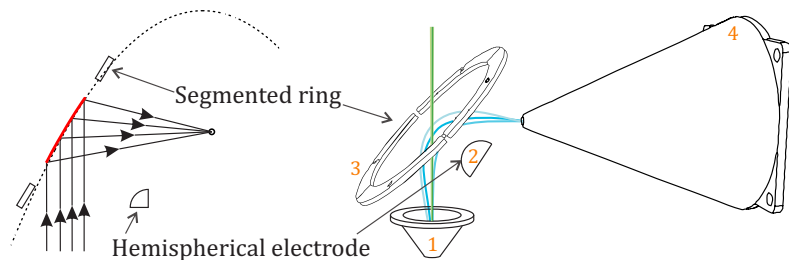
FIGURE 8.2: *Right:* Ion optics concept currently built. The ions (represented in blue) are exiting the ion funnel from the bottom and are extracted through a conical lens (1). The potentials applied to a segmented ring (3) and a hemispherical electrode (2) create a parabolic repulsive field (left, dotted line) to focus and steer ions to a unique spot at the entrance to the mass spectrometer (4).

Ion trajectories for different ion optic configurations were simulated using the commercial software package SIMION 8.0 ® (Scientific Instrument Services, Inc. Ringoes, NJ, USA) [181]. Through an iterative process, the geometry resulting in the highest transmission was chosen.
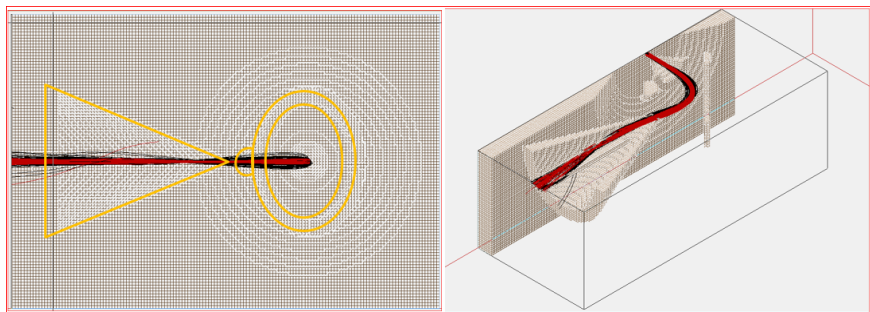
FIGURE 8.3: Simulations of ion trajectories using Simion 8 ® for a suite of ions of different m/Q, initial angle and kinetic energy represented by red and black lines. Left: Top view, right: cutaway showing the geometries of the optical components.

Figure 8.3 displays simulated trajectories of singly charged ions with varying starting angles in black (30° cone direction distribution, mass: 60

amu, kinetic energy: 0.5 eV) and kinetic energies and m/Q in red (single vector direction, mass: 1 to 300 amu, kinetic energy: 0.01 to 5 eV).

The entire new instrument layout, based on the descriptions above is shown in figure 4. The distance between the upper window and the sample could thereby be reduced to 11 cm. Assuming a Gaussian laser profile it is possible to calculate the theoretical spot size reachable using the formula:

$$w_0' \approx f \frac{\lambda}{\pi w_0} \tag{8.1}$$

where f is the focal length of the lens used, w_0' is the beam waist in the beam focus, w_0 is the initial beam waist and λ is the laser wavelength. The original laser beam waist (w_0) is circa 2 mm, its wavelength of 400 nm, which with a focal length of 12 cm, should theoretically allow for an ablation spot of 7,6 μm. Sample positioning is performed using a 3D translation stage, which is placed on an internal tray. A custom made stage was obtained from SmarAct (Germany), with a sample holder of 120 mm x 120 mm. The stage provides 83 mm travel direction in x and y and 16 mm in the z direction. The stage is capable of handling a normal load of 30 N, with a position repeatability of 120 nm. The stage is computer controlled, and translation patterns can be programmed. The tray on which the stage is placed, can be then inserted in the ablation chamber in a "drawer fashion" gliding on 2 bars. Due to the specification of the stage and the stage holder it is possible to use externally recorded microscope images to navigate the sample. A direct observation in the setup could be achieved with laser illumination and camera observation arranged co-axially with the ablation laser. During sample change the CD nozzle can be covered using a rotating gate valve. The bottom of the ablation chamber holds an additional window for beam adjustment purposes, when the stage in not present in the ablation chamber.
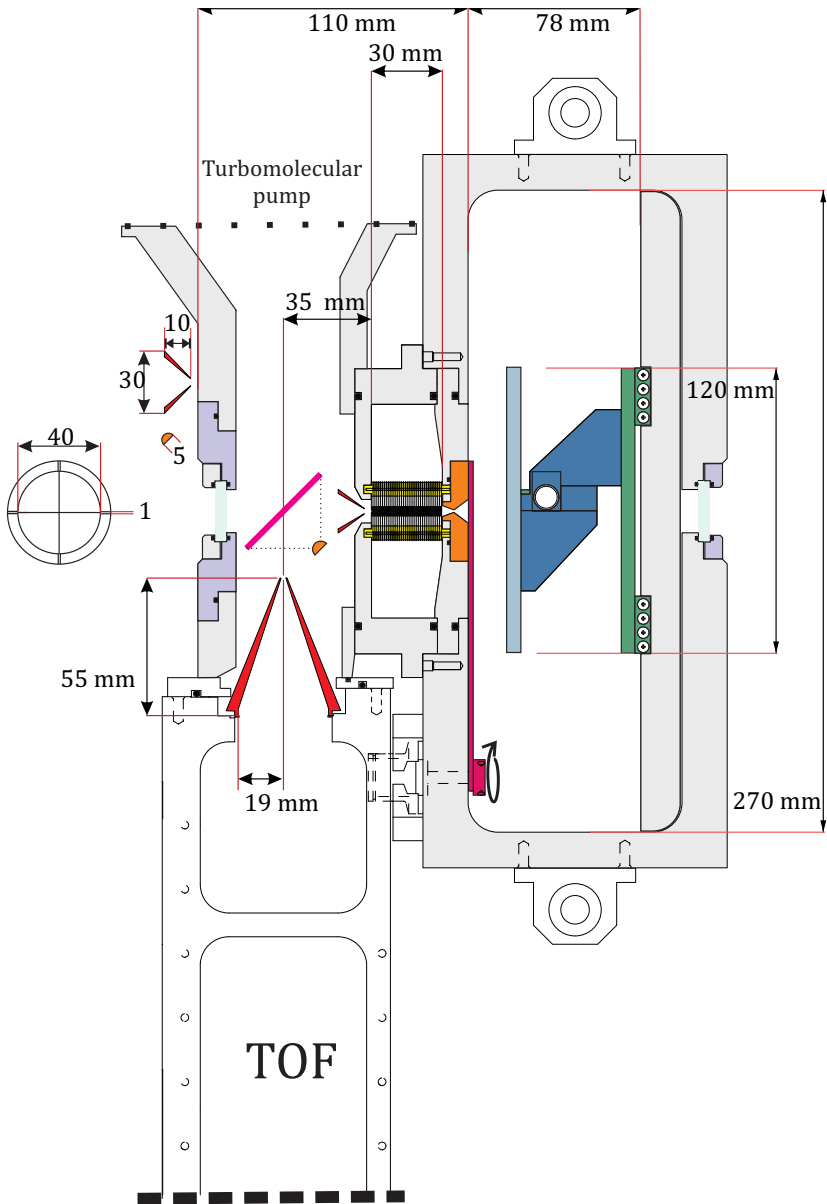
FIGURE 8.4: Schematic and dimension of the second prototype developed.

SUMMARY

Everything is impossible until someone does it.

— 🦇

In this work the characterization and the development a novel LAMS setup were presented. The Laser Ablation ion FUnnel (LAFU) source makes use of an original strategy for the efficient transfer of ions generated by laser ablation and ionization into a time-of-flight mass spectrometer. The LAFU source has been conceived in order to mitigate two main problems arising in conventional laser ablation ion sources for element analyses, namely the broad energy and spatial distributions of the ions generated in high vacuum. It employs a buffer gas for a two-stage thermalization and focusing of laser generated ions. Laser ionization is carried out at elevated pressure inside the buffer gas to instantaneously confine the expansion of the laser-generated ions. The ion-gas mixture is then extracted via a convergent-divergent nozzle into an ion funnel, where the majority of the buffer gas can be removed before the ion optics and mass spectrometer. The ion funnel is realized as an RF-only variant, where axial ion transmission is achieved exclusively using gas dynamics. Thereby the use of a DC-field, otherwise commonly employed in their construction can be omitted. This allows creating the ion funnel's effective potential by simply feeding a mirrored RF-potential to the pairwise alternating electrodes, which makes the assembly of the ion funnel easier. The LAFU source thus achieves confinement of the laser generated ions already at the ablation spot and thermalization and focusing inside the ion funnel. This combination has never before been used in practice for element- and isotope specific analyses. Initial experiments in this work were carried out using a frequency doubled Nd:YAG ns laser (532 nm, 3 ns pulse duration) and it was shown for the first time that the use of the CD nozzle-ion funnel combination successfully improved the ion detection compared to ablation in high vacuum. Ion signals were higher by up to a factor of 200. Furthermore the effective cooling of the ions resulted in substantially longer transient profiles of ions generated from a single laser pulse. The ion signals from were stretched from circa 100 μs for ablation in vacuum to a period of

about 1 ms or longer. Despite potentially higher signal/noise ratios attainable with a shorter signal duration, this effect is deemed beneficial for the use with time-of-flight MS. Commonly TOFMS provides a linear dynamic detection range of maybe 6 orders of magnitude. A longer signal duration will thus help to avoid detector saturation while still enabling ion detection over a wide linear range. Ion signals were found to increase for all species detected when the pressure in the ablation region was higher, which is attributed to the initial compression of the ion cloud. Furthermore, the ions' arrival times at the TOFMS were strongly influenced by the gas dynamics in the setup. A pressure increase from 10 to 55 mbar in the ablation region reduced the delay between ion generation and detection from 2.5 to below 0.5 ms. At the same time it was established how the mass dependence of ion transmission depended on operating conditions of the ion funnel. The RF amplitude and frequencies for optimal transmission were generally in accordance to predictions for an ion funnel configuration: Higher frequency or lower amplitude yielded better transmission for lower m/Q and vice versa. The changes in transmission were not directly proportional to the applied field but exhibited an m/Q-dependent slope. The initial configuration allowed for operation with RF-frequencies up to about 5 MHz and amplitudes up to 40 V_{pp} but the optimized conditions were found to be near 3 MHz and 20 V_{pp}. After hardware modifications and employing a new RF-amplifier higher transmission was obtained for a frequency of 5 MHz, probably because of a better quality of the amplified waveform. The ion transmission was found proportional to the ratio between RF-amplitude and the square root of the frequency. Using the ns laser, the LAFU source produced very high ion currents, which were found to be detrimental to the performance of the ion funnel and could saturate the detector of the TOFMS. Inside the ion funnel space charge effects could be noticed, in particular when high currents of the heavier isotopes (Pb and Bi) were present. These lead to suppression of the lighter isotopes (e.g Cu and Zn) and caused their transient profiles to exhibit a bimodal shape. Using the fs-laser in the later stage of the project alleviated this problem because ablation could be carried out with lower energy densities, yet higher power densities, which reduced the primary ion currents. Molecular ions and clusters were observed at varying abundances, while multiply charged ions never became truly obvious in the mass spectra. The latter may be because their initial kinetic energies are still too high and they can't be efficiently cooled or because they recombined electrons from the buffer gas or impurities in it. The gas impurities or water adsorbed on the

interior surfaces of the sample chamber on the other hand were found to be a main limitation of the present setup. They led to the formation of mostly water adducts with ions of the major components of the sample material, which caused spectral interferences to occur across the mass spectrum. In various instances it is possible to distinguish them from atomic ions due to the mass resolving power of the TOFMS but baseline separation is mostly difficult. Their abundances relative to the corresponding parent ions was found to be affected strongly by the gas dynamics. Higher pressure within the ablation region caused their relative abundances to increase because of the higher density of the laser generated plasma plume and eventually a higher total amount of the reactants. A higher pressure inside the ion funnel on the other hand led to a decrease in relative abundances of the larger ions due to more efficient cooling and, eventually, trapping inside the ion funnel. Additionally the water adducts were found to appear later in the transient laser profiles, making them distinguishable based on their arrival times in the MS.

Another major limitation of the initial setup was clearly the nanosecond laser used. Strong inter-element and matrix dependencies were found in terms of ion yield and ablation rates, because of the thermal effects occurring from the long pulse duration. The relative sensitivity coefficients of different elements in brass reference materials differed substantially from unity reaching values of several thousands for Pb and Bi for settings when promoting especially transmission of high m/Q in the ion funnel. But even when the ion funnel was operated in a way to balance high and low m/Q transmission the RSCs of different elements differed by up to 700 times and between samples of similar composition. Quantitative analyses even with matrix-matched calibrations standards would thus resulted in substantial deviations. It was thus assumed that near-UV femtosecond laser ablation was a viable way improve the quantification capabilities of the LAFU source over those using the ns laser. The source was thus was installed near a fs laser (400 nm, 250 fs pulse duration) available in the laboratory. At the same time it was noticed that a higher ion signal could be achieve when the distance of the sample to the CD nozzle's entrance was increased. For this new sample position a lower effective pressure in the ablation chamber found to to be optimal for ion detection. A broader m/Q transmission range was also found when an RF Frequency of 5 MHz and 20 V_{pp} were used with the new RF-amplifier. The direct comparison of the previously used ns laser and the fs laser under these conditions was made in order to elucidate if and how significant the use of a high-

irradiance laser can improve the capabilities of the LAFU source It could be shown that the signal evolution differed substantially as the crater developed for the two laser sources. Employing fs laser pulses for the ablation of a brass sample resulted in a slight increase in ion signals during the first 1500 laser pulses. This was followed by a steady decrease by nearly an order of magnitude for the subsequent 4500 pulses. In the case of ns pulses on the other hand, the first 1200 resulted in a steep decrease of circa one order of magnitude, followed by a comparably steady state signal across nearly 5000 pulses. Utilizing similar laser fluences, the sensitivities obtained when ablating a brass sample was generally higher for fs LAMS than for ns LAMS, with exception of Pb and Bi. Ions generated by both lasers exhibited a similar response to changes in gas dynamics and ion funnel operating conditions. Another major difference observed for the fs-laser was the occurrence of O_2^+ and H_3O^+ in the spectra, which indicates that high irradiance ablation can more efficiently also ionize species with higher ionization energies. The analytical capabilities fs-LAMS were then tested by ablating different metals using various laser energies. Element, matrix and energy dependence of signal intensities, signal ratios (RSC) and detection efficiencies were, however, still observed. RSCs in the brass samples however never exceeded values of 6 even for Pb and Bi, which constitutes a clear improvement over the ns laser. The ablation rates evaluated for different laser fluence indicated that as low as 2.5 nm per pulse material removal could be achieved in brass when using a fluence of 0.5 J/cm^2 and a 50 μm crater diameter. Analyses of isotope ratio data revealed that the mean mass discrimination was relatively uniform across the m/Q range with sub-% difference in isotope transmission per m/Q. The repeatability of the isotope ratio measurements was about 1% for experiments using 2000 laser pulses per analysis, which compares reasonably well with LA-ICPMS results for similar experimental conditions. Quantitative analysis of a brass sample using matrix matched calibration were performed; the deviation from the data obtained using LA-ICPMS were found to significantly depend on the laser fluence applied. Deviations by more than a factor of two were however only observed for Bi at the lowest fluence, i.e. sensitivity. At higher fluence the agreement was typically better than 50 % indicating that semiquantitative analyses are feasible under these conditions. The detection efficiencies were evaluated by comparing ions detected with atoms removed in an experiment and were varying from 10^{-12} to 10^{-8}, which constitutes probably the most substantial weakness of the current setup. Inspecting the ion lens at the entrance to the TOFMS during maintenance,

revealed that a significant fraction of ions must be lost at this transition. The dark halo that was visible around the entrance aperture is a clear sign of ion deposition and thus must mean that a significant fraction of the ions generated in the LAFU source could not be transmitted to the TOFMS. This can at least partly serve as an explanation for the relatively poor detection efficiencies obtained. The depth profiling capability of the fs-LAFU source were investigated by analyzing a commercial computer hard disk as test case and a Cr-Ni multi-layer SRM as depth profiling reference. Analyses of the hard disk revealed substantial differences in composition of the different layers and even the topmost thin Cr-Ru layer could be clearly identified. It was further possible to resolve all individual 57 nm Cr and 56 nm Ni layers in the SRM. The top 57 nm Cr layer was ablated within the first four pulses resulting in a depth resolution of approximately 15 nm close to the surface. Due to the Gaussian beam profile of the laser used however the depth resolution decreases substantially with pulses applied. The analysis of glasses was not possible at all using the 532 nm ns laser source. Using the 400 nm fs laser on the other hand also the NIST SRM 610 and even the more transparent SRM 612 could be successfully ablated. The ablation required however a substantially higher fluence of 36 J/cm^2, more than ten times that used for the metals analyzed before. Despite the high fluence however the glasses showed a highly particular temporal evolution of the transient signals. Two distinguishable ablation regimes were present: During the initial approximately 50 pulses the spectra were dominated by alkali metals ions whereas other species including the sample matrix were barely detected. It was furthermore yielding two distinguishable ion populations, arriving at the TOFMS at different times. After this "conditioning period" also ion signals of other matrix and trace elements appeared at clearly detectable levels. This seems to indicate that even ablation of the glasses did not immediately occur when using high irradiance laser pulses. The analyte sensitivities were evaluated only for the second regime for both samples. In most cases the sensitivities were relatively similar but still about 100 times lower than usually seen with LA-ICPMS. Significant differences were however observed for more oxophilic elements, where the more transparent sample with lower mass fractions of the trace elements (SRM NIST 612) had higher sensitivities. Therefore, RSCs relative to Na as internal standard were found to vary by up to a factor of 10 between the two samples. Limits of detection were estimated to be in a range between tens of ppb (for Cs and Rb) to ppm (Ca, As, Y, Nb, La, Ce, Th U) or even tens of ppm (Al, Si). Ultimately, this work could show that LAMS exper-

iments using the new LAFU source are possible for all materials tested, when using the 400 nm fs laser source. Operating parameters could be optimized and figures of merit could be established for a range of relevant solid sample materials using standard reference materials and laboratory test samples. The figures of merit however currently cannot compete with established analytical methods but this was also not expected when considering the early stage of the development. The overall performance however is promising. The per-pulse ion signal duration is short enough to allow for baseline-resolved detection of ions generated by individual laser pulses up to the kHz regime, which makes it appealing for high throughput element specific imaging applications. The per-pulse duration on the other hand is sufficiently long to extend the linear dynamic range of the TOFMS detector above 6 orders of magnitude and thereby may allow for major, trace and ultra-trace analyses in solid samples of any kind. Detection efficiency would need to be improved to become attractive in such applications but the initial design of the ion optics was identified as a limiting factor in this respect, which can relatively easily be improved.

10

OUTLOOK

To overcome the limitations experienced with the current setup (low ion transmission, spectral interferences and sample positioning in particular), a remodeling of the setup was initiated which included the design of a new sample positioning system and ion optical setup. The modifications have been described in the final part of this thesis and are currently underway with the help of the mechanical workshop. Upon completion the components will have to be thoroughly tested and characterized. To optimize ion transmission from the ablation region to the mass spectrometer the pressure and flow conditions of the new chamber in combination with the CD-nozzle and ion funnel operating conditions need to be re-evaluated in detail. The efficiency of the modified ion optical system will have to be subject of investigation in order to improve the detection efficiency, mass dependency of ion transmission. In the authors opinion it would be worthwhile to further investigate the fundamental aspects behind the ion formation properties of the setup in particular the behavior of glasses. Another step could be to evaluate the used of the frequency-quadrupled fs laser. By operating at 200 nm the ablation and ionization of glass in particular may be expected to be improved due to stronger absorption of the laser radiation. Additionally, it would allow for better understanding of the influence of laser wavelength on ablation rates, sample dissociation and ionization of the different elements in more detail. The new setup was also conceived to minimize the amount of residual water on the interior surfaces by electroplating them with gold. Still, the larger total surface area poses the risk of total contaminations being present in the buffer gas and leading to spectral interferences. The new optics layout should allow for tighter focusing the laser beam thus reaching higher fluences with lower laser beam energies. This can help reducing the ablation spot size and improve the spatial resolution without compromising analytical performance substantially. The positioning system will furthermore allow for better control of laser focus and allow for controlled rastering of the laser beam across the surface of a sample to create element maps or images. This feature may be particularly interesting in various applications. In combination with the comparably short signal duration for a single laser pulse it might become a viable alternative for high-resolution, high throughput element imaging applications.

ACRONYMS

AAR	Average Ablation Rate
ABS	Acrylonitrile Butadiene Styrene
ADC	Analog to Digital Converter
BP	Boiling Point
CD	Convergent-Divergent
cw	continuous wave
CPA	Chirped Pulse Amplification
DE	Detection Efficiency
DC	Direct Current
fs	femtosecond
HD	Hard Disk
KE	Kinetic Energy
LOD	Limit of Detection
MBC	Maxwell–Boltzmann–Coulomb
MCP	Multichannel Plate
m/Q	mass to charge
ns	nanosecond
NIST	National Institute of Standards and Technology
PHD	Pulse-Height Distribution
RF	Radio Frequency
RSC	Relative Sensitivity Coefficient
RSF	Relative Sensitivity Factor

SRM	Standard Reference Material
SIS	Single-Ion Signal
TIC	Total Ion Current

Instrumental

CM	Confocal Microscopy
ESI-MS	Electrospray Ionization Mass-Spectroscopy
ESI	Electrospray Ionization
LA-ICPMS	Laser Ablation Inductively Coupled Plasma Mass-Spectroscopy
LAMMA	Laser Microprobe Mass Analyzer
LAMS	Laser Ablation Mass Spectrometry
LIBS	Laser Induced Breakdown Spectroscopy
MALDI	Matrix Assisted Laser Desorption ionization
OALAMS	Open Air Laser Ablation Mass Spectrometry
SIMS	Secondary Ion Mass Spectrometry
TOFMS	Time of Flight Mass-Spectrometer
TOF	Time of Flight
XRF	X-ray fluorescence

1. Honig, R. E. & Woolston, J. R. Laser-induced emission of electrons, ions, and neutral atoms from solid surfaces. *Applied Physics Letters* **2**, 138 (1963).

2. Ban, V. S. & Knox, B. E. Mass spectrometric studies of laser-produced vapor species. *International Journal of Mass Spectrometry and Ion Physics* **3**, 131 (1969).

3. Knox, B. E., Ban, V. S. & Schottmiller, J. Mass spectrometric studies of laser-induced vaporization. II. The bismuth-selenium system. *Materials Research Bulletin* **3**, 337 (1968).

4. Knox, B. E. Mass spectrometric studies of laser-induced vaporization. I. Selenium. *Materials Research Bulletin* **3**, 329 (1968).

5. Knox, B. E. & Ban, V. S. Mass spectrometric studies of laser-induced vaporization. III. The arsenic-selenium system. *Materials Research Bulletin* **3**, 885 (1968).

6. Zahn, H. & Dietze, H.-J. Die bestimmung der anzahl der ionen, elektronen und atome in lasermikroplasmen von feststoffen. *International Journal of Mass Spectrometry and Ion Physics* **22**, 111 (1976).

7. Zavitsanos, P. Mass spectrometric analysis of carbon species generated by laser evaporation. *Carbon* **6**, 731 (1968).

8. Hillenkamp, F., Unsöld, E., Kaufmann, R. & Nitsche, R. A high-sensitivity laser microprobe mass analyzer. *Applied Physics* **8**, 341 (1975).

9. Hillenkamp, F. & Karas, M. in *MALDI MS* 1 (Wiley-VCH Verlag GmbH & Co. KGaA, Weinheim, Germany, 2007).

10. Griffiths, J. A Brief History of Mass Spectrometry. *Analytical Chemistry* **80**, 5678 (2008).

11. Karas, M., Bachmann, D. & Hillenkamp, F. Influence of the wavelength in high-irradiance ultraviolet laser desorption mass spectrometry of organic molecules. *Analytical Chemistry* **57**, 2935 (1985).

12. Caprioli, R. M., Farmer, T. B. & Gile, J. Molecular Imaging of Biological Samples: Localization of Peptides and Proteins Using MALDI-TOF MS. *Analytical Chemistry* **69**, 4751 (1997).

13. Clark, A. E., Kaleta, E. J., Arora, A. & Wolk, D. M. Matrix-Assisted laser desorption ionization-time of flight mass spectrometry: A fundamental shift in the routine practice of clinical microbiology. *Clinical Microbiology Reviews* **26**, 547 (2013).

14. Denoyer, E., Grieken, R. V., Adams, F. & Natusch, D. F. S. Laser Microprobe Mass Spectrometry 1: Basic Principles and Performance Characteristics. *Analytical Chemistry* **54**, 26A (1982).

15. Denoyer, E., Natusch, D. F. S., Surkyn, P. & Adams, F. C. Laser microprobe mass analysis (LAMMA) as a tool for particle characterization: a study of coal fly ash. *Environmental Science & Technology* **17**, 457 (1983).

16. Hattendorf, B. & Günther, D. in *Handbook of Spectroscopy* 647 (Wiley-VCH Verlag GmbH & Co. KGaA, Weinheim, Germany, 2014).

17. Eggins, S. M., Woodhead, J. D., Kinsley, L. P. J., Mortimer, G. E., Sylvester, P. J., McCulloch, M. T., Hergt, J. M. & Handler, M. R. A simple method for the precise determination of > 40 trace elements in geological samples by ICPMS using enriched isotope internal standardisation. *Chemical Geology* **1**, 311 (1997).

18. Fleitmann, D. Holocene Forcing of the Indian Monsoon Recorded in a Stalagmite from Southern Oman. *Science* **300**, 1737 (2003).

19. Heinrich, C., Pettke, T., Halter, W., Aigner-Torres, M., Audétat, A., Günther, D., Hattendorf, B., Bleiner, D., Guillong, M. & Horn, I. Quantitative multi-element analysis of minerals, fluid and melt inclusions by laser-ablation inductively-coupled-plasma mass-spectrometry. *Geochimica et Cosmochimica Acta* **67**, 3473 (2003).

20. Rubatto, D. Zircon trace element geochemistry: Partitioning with garnet and the link between U-Pb ages and metamorphism. *Chemical Geology* **184**, 123 (2002).

21. Pröfrock, D. & Prange, A. Inductively Coupled Plasma–Mass Spectrometry (ICP-MS) for Quantitative Analysis in Environmental and Life Sciences: A Review of Challenges, Solutions, and Trends. *Applied Spectroscopy* **66**, 843 (2012).

22. Becker, J. S., Zoriy, M., Matusch, A., Wu, B., Salber, D., Palm, C. & Becker, J. S. Bioimaging of metals by laser ablation inductively coupled plasma mass spectrometry (LA-ICP-MS). *Mass Spectrometry Reviews* **29**, 156 (2010).

23. Chang, Q., Ornatsky, O. I., Siddiqui, I., Loboda, A., Baranov, V. I. & Hedley, D. W. Imaging Mass Cytometry. *Cytometry Part A* **91**, 160 (2017).

24. Giesen, C., Wang, H. A. O., Schapiro, D., Zivanovic, N., Jacobs, A., Hattendorf, B., Schüffler, P. J., Grolimund, D., Buhmann, J. M., Brandt, S., Varga, Z., Wild, P. J., Günther, D. & Bodenmiller, B. Highly multiplexed imaging of tumor tissues with subcellular resolution by mass cytometry. *Nature Methods* **11**, 417 (2014).

25. Irrgeher, J. & Prohaska, T. *Application of non-traditional stable isotopes in analytical ecogeochemistry assessed by MC ICP-MS - A critical review* 2016.

26. Resano, M., García-Ruiz, E. & Vanhaecke, F. Laser ablation-inductively coupled plasma mass spectrometry in archaeometric research. *Mass Spectrometry Reviews* **29**, 55 (2010).

27. Speakman, R. & Neff, H. *Laser ablation ICP-MS in archaeological research* (UNM Press, 2005).

28. Batista, B. L., Rodrigues, J. L., de Oliveira Souza, V. C. & Barbosa, F. A fast ultrasound-assisted extraction procedure for trace elements determination in hair samples by ICP-MS for forensic analysis. *Forensic Science International* **192**, 88 (2009).

29. Suzuki, Y., Sugita, R., Suzuki, S. & Marumo, Y. Forensic Discrimination of Bottle Glass by Refractive Index Measurement and Analysis of Trace Elements with ICP-MS. *Analytical Sciences* **16**, 1195 (2000).

30. Ulrich, A., Moor, C., Vonmont, H., Jordi, H. R. & Lory, M. ICP-MS trace-element analysis as a forensic tool. *Analytical and Bioanalytical Chemistry* **378**, 1059 (2004).

31. Massonnet, P. & Heeren, R. M. A concise tutorial review of TOF-SIMS based molecular and cellular imaging. *Journal of Analytical Atomic Spectrometry* **34**, 2217 (2019).

32. De Samber, B., De Schamphelaere, K. A., Janssen, C. R., Vekemans, B., De Rycke, R., Martinez-Criado, G., Tucoulou, R., Cloetens, P. & Vincze, L. *Hard X-ray nanoprobe investigations of the subtissue metal distributions within Daphnia magna* in *Analytical and Bioanalytical Chemistry* **405** (2013), 6061.

33. De Samber, B., Silversmit, G., De Schamphelaere, K., Evens, R., Schoonjans, T., Vekemans, B., Janssen, C., Masschaele, B., Van Hoorebeke, L., Szalóki, I., Vanhaecke, F., Rickers, K., Falkenberg, G. & Vincze, L. Element-to-tissue correlation in biological samples determined by three-dimensional X-ray imaging methods. *Journal of Analytical Atomic Spectrometry* **25**, 544 (2010).

34. Modlitbová, P., Pořízka, P. & Kaiser, J. *Laser-induced breakdown spectroscopy as a promising tool in the elemental bioimaging of plant tissues* 2020.

35. Yu, Q., Chen, L., Huang, R., Hang, W., Huang, B., Hang, W. & He, J. *Laser ionization time-of-flight mass spectrometry for direct elemental analysis* 2009.

36. Wang, X., Zhang, S., Cheng, X., Zhu, E., Hang, W. & Huang, B. Ion kinetic energy distributions in laser-induced plasma. *Spectrochimica Acta - Part B Atomic Spectroscopy* **99**, 101 (2014).

37. Hang, W. Laser ionization time-of-flight mass spectrometer with an ion guide collision cell for elemental analysis of solids. *Journal of Analytical Atomic Spectrometry* **20**, 301 (2005).

38. Johnson, P. V., Hodyss, R., Tang, K., Brinckerhoff, W. B. & Smith, R. D. The laser ablation ion funnel: Sampling for in situ mass spectrometry on Mars. *Planetary and Space Science* **59**, 387 (2011).

39. Riedo, A., Bieler, A., Neuland, M., Tulej, M. & Wurz, P. Performance evaluation of a miniature laser ablation time-of-flight mass spectrometer designed for in situ investigations in planetary space research. *Journal of mass spectrometry : JMS* **48**, 1 (2013).

40. Rohner, U., Whitby, J. A. & Wurz, P. A miniature laser ablation time-of-flight mass spectrometer for in situ planetary exploration. *Meeasurement Science and Technology* **14**, 2159 (2003).

41. Riedo, A., Meyer, S., Heredia, B., Neuland, M., Bieler, A., Tulej, M., Leya, I., Iakovleva, M., Mezger, K. & Wurz, P. Highly accurate isotope composition measurements by a miniature laser ablation mass spectrometer designed for in situ investigations on planetary surfaces. *Planetary and Space Science* **87**, 1 (2013).

42. Douglas, D. J. Applications of collision dynamics in quadrupole mass spectrometry. *Journal of the American Society for Mass Spectrometry* **9**, 101 (1998).

43. Douglas, D. J. & French, J. B. Collisional focusing effects in radio frequency quadrupoles. *Journal of the American Society for Mass Spectrometry* **3**, 398 (1992).

44. He, J., Zhong, W., Mahan, C. & Hang, W. Laser ablation and ionization time-of-flight mass spectrometer with orthogonal sample introduction and axial field rf-only quadrupole cooling. *Spectrochimica Acta - Part B Atomic Spectroscopy* **61**, 220 (2006).

45. He, J., Huang, R., Yu, Q., Lin, Y., Hang, W. & Huang, B. A small high-irradiance laser ionization time-of-flight mass spectrometer. *Journal of Mass Spectrometry* **44**, 780 (2009).

46. Yu, Q., Huang, R., Li, L., Lin, L., Hang, W., He, J. & Huang, B. Applicability of standardless semiquantitative analysis of solids by high-irradiance laser ionization orthogonal time-of-fight mass spectrometry. *Analytical Chemistry* **81**, 4343 (2009).

47. Cui, Y., Moore, J. F. J., Milasinovic, S., Liu, Y., Gordon, R. J. R. & Hanley, L. Depth profiling and imaging capabilities of an ultrashort pulse laser ablation time of flight mass spectrometer. *Review of Scientific Instruments* **83**, 093702 (2012).

48. Karpov, A. V., Spakhov, A. V. & Sysoev, A. A. Compact analyzer for a laser time-of-flight mass spectrometer. *European Journal of Mass Spectrometry* **21**, 823 (2015).

49. Sysoev, A. A., Karpov, A. V., Milyaeva, V. V. & Sysoev, A. A. Novel approach to constructing laser ionization elemental time-of-flight mass spectrometer. *European Journal of Mass Spectrometry* **24**, 96 (2018).

50. Sysoeva, E. & Sysoev, A. Letter: A method for the chromatic aberration correction of a laser time of-flight mass analyzer. *European Journal of Mass Spectrometry* **22**, 141 (2016).

51. Riedo, A., Neuland, M., Meyer, S., Tulej, M. & Wurz, P. Coupling of LMS with a fs-laser ablation ion source: elemental and isotope composition measurements. *Journal of Analytical Atomic Spectrometry* **28**, 1256 (2013).

52. Zhang, B., He, M., Hang, W. & Huang, B. Minimizing matrix effect by femtosecond laser ablation and ionization in elemental determination. *Analytical Chemistry* **85**, 4507 (2013).

53. He, M., Li, B., Yu, S., Zhang, B., Liu, Z., Hang, W. & Huang, B. Buffer-gas assisted high irradiance femtosecond laser ionization orthogonal time-of-flight mass spectrometry for rapid depth profiling. *Journal of Analytical Atomic Spectrometry* **28**, 499 (2013).

54. Grimaudo, V., Moreno-García, P., Riedo, A., Neuland, M. B., Tulej, M., Broekmann, P. & Wurz, P. High-resolution chemical depth profiling of solid material using a miniature laser ablation/ionization mass spectrometer. *Analytical Chemistry* **87**, 2037 (2015).

55. Grimaudo, V., Moreno-García, P., Riedo, A., Neuland, M. B., Tulej, M., Broekmann, P. & Wurz, P. High-Resolution Chemical Depth Profiling of Solid Material Using a Miniature Laser Ablation/Ionization Mass Spectrometer. *Analytical Chemistry* **87**, 2037 (2015).

56. Grimaudo, V., Moreno-García, P., Cedeño López, A., Riedo, A., Wiesendanger, R., Tulej, M., Gruber, C., Lörtscher, E., Wurz, P. & Broekmann, P. Depth Profiling and Cross-Sectional Laser Ablation Ionization Mass Spectrometry Studies of Through-Silicon-Vias. *Analytical Chemistry*, acs.analchem.7b05313 (2018).

57. Yin, Z., Cheng, X., Liu, R., Hang, W., Huang, B., Benninghoven, A., Christman, L., Sanz-Medel, A. & Shyue, J.-J. Depth profiling of nanometer thin layers by laser desorption and laser postionization time-of-flight mass spectrometry. *J. Anal. At. Spectrom.* **16**, 1317 (2017).

58. Huang, R., Zhang, B., Zou, D., Hang, W., He, J. & Huang, B. Elemental imaging via laser ionization orthogonal time-of-flight mass spectrometry. *Analytical chemistry* **83**, 1102 (2011).

59. He, M., Meng, Y., Yan, S., Hang, W., Zhou, W. & Huang, B. Three-dimensional elemental imaging of Nantan meteorite via femtosecond laser ionization time-of-flight mass spectrometry. *Analytical Chemistry* **89**, 565 (2017).

60. Grimaudo, V., Moreno-García, P., Riedo, A., Meyer, S., Tulej, M., Neuland, M. B., Mohos, M., Gütz, C., Waldvogel, S. R. R., Wurz, P., Broekmann, P., Moreno-Garcia, P., Riedo, A., Meyer, S., Tulej, M., Neuland, M. B., Mohos, M., Gütz, C., Waldvogel, S. R. R., Wurz, P. & Broekmann, P. Towards 3D Chemical Imaging of Ternary Cu-Sn-Pb Alloys using Femtosecond Laser Ablation/Ionization Mass Spectrometry. *Analytical Chemistry* **89**, acs.analchem.6b03738 (2017).

61. Chen, L., Lin, L., Yu, Q., Yan, X., Hang, W., He, J. & Huang, B. Semiquantitative Multielemental Analysis of Biological Samples by a Laser Ionization Orthogonal Time-of-Flight Mass Spectrometer. *Journal of the American Society for Mass Spectrometry* **20**, 1355 (2009).

62. Huang, R., Yu, Q., Tong, Q., Hang, W., He, J. & Huang, B. Influence of wavelength, irradiance, and the buffer gas pressure on high irradiance laser ablation and ionization source coupled with an orthogonal Time of Flight Mass Spectrometer. *Spectrochimica Acta Part B: Atomic Spectroscopy* **64**, 255 (2009).

63. Alcántara, J. F., Vadillo, J. M. & Laserna, J. J. Experimental variables and matrix effects associated with the onset of ion generation in laser ionization of solid samples. *Journal of Analytical Atomic Spectrometry* **25**, 1424 (2010).

64. Choi, I., Song, K., Park, Y. J., Kim, J. Y. & Yoo, H. S. Isotopic analysis of metallic and coated microparticles by laser ablation time-of-flight mass spectrometry (LA-TOF-MS). *Microchemical Journal* **95**, 38 (2010).

65. Yan, B., Li, L., Yu, Q., Hang, W., He, J. & Huang, B. High irradiance laser ionization mass spectrometry for direct speciation of iron oxides. *Journal of the American Society for Mass Spectrometry* **21**, 1227 (2010).

66. Yu, Q., Li, L., Zhu, E., Hang, W., He, J. & Huang, B. Analysis of solids with different matrices by buffer-gas-assisted laser ionization orthogonal time-of-flight mass spectrometry. *J. Anal. At. Spectrom.* **25**, 1155 (2010).

67. Li, N., Zhang, B., Huango, R., Hang, W., He, J. & Huang, B. Laser ionization orthogonal time-of-flight mass spectrometry for simultaneous determination of nonmetallic elements in solids. *Analytical Chemistry* **82**, 1949 (2010).

68. Tulej, M., Iakovleva, M., Leya, I. & Wurz, P. A miniature mass analyser for in-situ elemental analysis of planetary material–performance studies. *Analytical and Bioanalytical Chemistry* **399**, 2185 (2011).

69. Zhang, B., Zou, D., Huang, R., Liu, G., Gong, Z., Hang, W. & Huang, B. Study on distribution of elements in deep-sea Pacific polymetallic nodules via two-dimensional mapping laser ionization orthogonal time-of-flight mass spectrometry. *Spectrochimica Acta - Part B Atomic Spectroscopy* **85**, 13 (2013).

70. He, M., Li, B., Zhang, B., Hang, W. & Huang, B. Buffer-Gas Assisted High Irradiance Femtosecond Laser Ionization Orthogonal Time-of-Flight Mass Spectrometry for Rapid Depth Profiling. *J. Anal. At. Spectrom.* 2 (2012).

71. Gao, Y., Lin, Y., Zhang, B., Zou, D., He, M., Dong, B., Hang, W. & Huang, B. Single-cell elemental analysis via high irradiance femtosecond laser ionization time-of-flight mass spectrometry. *Analytical Chemistry* **85**, 4268 (2013).

72. Neuland, M., Meyer, S., Mezger, K., Riedo, A., Tulej, M. & Wurz, P. Probing the Allende meteorite with a miniature laser-ablation mass analyser for space application. *Planetary and Space Science* **101**, 196 (2014).

73. Yin, Z., Sun, B., Wang, X., Cheng, X., Hang, W. & Huang, B. Comprehensive analysis of metalloporphyrins via high irradiance laser ionization time-of- fl ight mass spectrometry. *Journal of Analytical Atomic Spectrometry* **29**, 1714 (2014).

74. Lu, Y., Zhou, Y. S., Qiu, W., Huang, X., Liu, L., Jiang, L., Silvain, J. F. & Lu, Y. F. Magnetic field enhancement for femtosecond-laser-ablation mass spectrometry in ambient environments. *Journal of Analytical Atomic Spectrometry* **30**, 2303 (2015).

75. Kuznetsov, I., Burian, T., Juha, L., Soufli, R., Filevich, J., Woolston, M., Bernstein, E. R., Crick, D. C., Carlton, D., Chao, W., Anderson, E. H., Rocca, J. J. & Menoni, C. S. *Soft x-ray laser ablation mass spectrometry for materials study and nanoscale chemical imaging* in *X-Ray Lasers and Coherent X-Ray Sources: Development and Applications XI* (eds Klisnick, A. & Menoni, C. S.) **9589** (International Society for Optics and Photonics, 2015), 958905.

76. Green, T., Kuznetsov, I., Willingham, D., Naes, B. E., Eiden, G. C., Zhu, Z., Chao, W., Rocca, J. J., Menoni, C. S. & Duffin, A. M. Characterization of extreme ultraviolet laser ablation mass spectrometry for actinide trace analysis and nanoscale isotopic imaging. *Journal of Analytical Atomic Spectrometry* **32**, 1092 (2017).

77. Zhou, Y. S., Lu, Y., Wang, M. M., Liu, L., Huang, X., Jiang, L. J., Jiang, L., Silvain, J.-F. & Lu, Y. F. Isotope signature characterization of Pb and U in open air by laser-ablation mass spectrometry. *Journal of Analytical Atomic Spectrometry* **32**, 1932 (2017).

78. Müller, R., Kuznetsov, I., Arbelo, Y., Trottmann, M., Menoni, C. S., Rocca, J. J., Patzke, G. R. & Bleiner, D. Depth-Profiling Microanalysis of CoNCN Water-Oxidation Catalyst Using a λ = 46.9 nm Plasma Laser for Nano-Ionization Mass Spectrometry. *Analytical Chemistry* **90**, 9234 (2018).

79. Cedeño López, A., Grimaudo, V., Moreno-García, P., Riedo, A., Tulej, M., Wiesendanger, R., Wurz, P. & Broekmann, P. Towards femtosecond laser ablation ionization mass spectrometric approaches for chemical depth-profiling analysis of lead-free Sn solder bumps with minimized side-wall contributions. *Journal of Analytical Atomic Spectrometry* **33**, 283 (2018).

80. Wang, F., Zhang, Y., Zhao, Y. G., Guo, D. F., Xie, S. K., Tan, J., Li, J. Y. & Lu, J. Application of laser ionization mass spectrometry for measurement of uranium isotope ratio in nuclear forensics and nuclear safeguards. *Measurement Science and Technology* **29**, 095903 (2018).

81. Page, J. S., Tolmachev, A. V., Tang, K. & Smith, R. D. Theoretical and experimental evaluation of the low m/z transmission of an electrodynamic ion funnel. *Journal of the American Society for Mass Spectrometry* **17**, 586 (2006).

82. Einstein, A. Zur Quantentheorie der Strahlung. *Physikalische Zeitschrift* **18**, 121 (1917).

83. Renk, K. F. *Basics of Laser Physics Graduate Texts in Physics* **5**, 419 (Springer International Publishing, Cham, 2012).

84. Svelto, O. *Principles of Lasers* 1 (Springer US, Boston, MA, 2010).

85. Penzkofer, A. Passive Q-switching and mode-locking for the generation of nanosecond to femtosecond pulses. *Applied Physics B Photophysics and Laser Chemistry* **46**, 43 (1988).

86. Spühler, G. J., Paschotta, R., Fluck, R., Braun, B., Moser, M., Zhang, G., Gini, E. & Keller, U. Experimentally confirmed design guidelines for passively Q-switched microchip lasers using semiconductor saturable absorbers. *Journal of the Optical Society of America B* **16**, 376 (1999).

87. Chen, F., Yu, X., Yan, R. P., Li, X. D., Li, D. J., Yang, G. L., Xie, J. J. & Guo, J. Experimental investigation of a diode-pumped powerful continuous-wave dual-wavelength Nd:YAG laser at 946 and 938.6 nm. *Laser Physics* **23**, 055002 (2013).

88. Kushida, T., Marcos, H. M. & Geusic, J. E. Laser Transition Cross Section and Fluorescence Branching Ratio for Nd^{3+} in Yttrium Aluminum Garnet. *Physical Review* **167**, 289 (1968).

89. Hargrove, L. E., Fork, R. L. & Pollack, M. A. Locking of he-ne laser modes induced by synchronous intracavity modulation. *Applied Physics Letters* **5**, 4 (1964).

90. Herrmann, J. Theory of Kerr-lens mode locking: role of self-focusing and radially varying gain. *Journal of the Optical Society of America B* **11**, 498 (1994).

91. Bäuerle, D. *Laser Processing and Chemistry* (Springer Berlin Heidelberg, Berlin, Heidelberg, 2011).

92. Gamaly, E. G. & Rode, A. V. Physics of ultra-short laser interaction with matter: From phonon excitation to ultimate transformations. *Progress in Quantum Electronics* **37**, 215 (2013).

93. Von der Linde, D., Sokolowski-Tinten, K. & Bialkowski, J. Laser-solid interaction in the femtosecond time regime. *Applied Surface Science* **109-110**, 1 (1997).

94. Liu, X., Du, D. & Mourou, G. Laser ablation and micromachining with ultrashort laser pulses. *IEEE Journal of Quantum Electronics* **33**, 1706 (1997).

95. Sugioka, K., Meunier, M. & Piqué, A. *Laser Precision Microfabrication* (eds Sugioka, K., Meunier, M. & Piqué, A.) (Springer Berlin Heidelberg, Berlin, Heidelberg, 2010).

96. Tillack, M. S., Blair, D. W. & Harilal, S. S. The effect of ionization on cluster formation in laser ablation plumes. *Nanotechnology* **15**, 390 (2004).

97. Bekefi, G. Principles of Laser Plasmas. *Journal of The Electrochemical Society* **124**, 435C (1977).

98. Takahashi, a. & Nishijima, K. Kinetic Model of Gas Heating of Laser-Produced Plasmas by CO_{2} Laser in Atmospheric Air. *Japanese Journal of Applied Physics* **37**, 313 (1998).

99. Anisimov, S. I., Luk'yanchuk, B. S. & Luches, A. An analytical model for three-dimensional laser plume expansion into vacuum in hydrodynamic regime. *Applied Surface Science* **96-98**, 24 (1996).

100. Amoruso, S., Bruzzese, R., Spinelli, N. & Velotta, R. Characterization of laser-ablation plasmas. *Journal of Physics B: Atomic, Molecular and Optical Physics* **32** (1999).

101. Kelly, R. & Miotello, A. Comments on explosive mechanisms of laser sputtering. *Applied Surface Science* **96-98**, 205 (1996).

102. Sokolowski-Tinten, K., Bialkowski, J., Cavalleri, A., von der Linde, D., Oparin, A., Meyer-ter-Vehn, J. & Anisimov, S. Transient States of Matter during Short Pulse Laser Ablation. *Physical Review Letters* **81**, 224 (1998).

103. Zhigilei, L. V. & Garrison, B. J. Microscopic mechanisms of laser ablation of organic solids in the thermal and stress confinement irradiation regimes. *Journal of Applied Physics* **88**, 1281 (2000).

104. Vidal, F., Johnston, T. W., Laville, S., Barthélemy, O., Chaker, M., Le Drogoff, B., Margot, J. & Sabsabi, M. Critical-point phase separation in laser ablation of conductors. *Physical Review Letters* **86**, 2573 (2001).

105. Apiñániz, J. I., Sierra, B., Martínez, R., Longarte, A., Redondo, C. & Castaño, F. Ion kinetic energy distributions and mechanisms of pulsed laser ablation on Al+. *Journal of Physical Chemistry C* **112**, 16556 (2008).

106. Caridi, F., Torrisi, L., Margarone, D. & Borrielli, A. Investigations on low temperature laser-generated plasmas. *Laser and Particle Beams* **26**, 265 (2008).

107. Écija, P., Sánchez Rayo, M. N., Martínez, R., Sierra, B., Redondo, C., Basterretxea, F. J. & Castaño, F. Fundamental processes in nanosecond pulsed laser ablation of metals in vacuum. *Physical Review A* **77**, 032904 (2008).

108. Giuffrida, L., Torrisi, L., Gammino, S., Wolowski, J. & Ullschmied, J. Surface ion implantation induced by laser-generated plasmas. *Radiation Effects and Defects in Solids* **165**, 534 (2010).

109. Sage, R. S., Cappel, U. B., Ashfold, M. N. R. & Walker, N. R. Quadrupole mass spectrometry and time-of-flight analysis of ions resulting from 532nm pulsed laser ablation of Ni, Al, and ZnO targets. *Journal of Applied Physics* **103**, 093301 (2008).

110. Torrisi, L., Caridi, F., Margarone, D. & Borrielli, A. Plasma–laser characterization by electrostatic mass quadrupole analyzer. *Nuclear Instruments and Methods in Physics Research Section B: Beam Interactions with Materials and Atoms* **266**, 308 (2008).

111. Torrisi, L., Caridi, F., Margarone, D. & Borrielli, A. Characterization of laser-generated silicon plasma. *Applied Surface Science* **254**, 2090 (2008).

112. Torrisi, L., Gammino, S., Andò, L. & Làska, L. Tantalum ions produced by 1064 nm pulsed laser irradiation. *Journal of Applied Physics* **91**, 4685 (2002).

113. Torrisi, L., Caridi, F., Picciotto, A., Margarone, D. & Borrielli, A. Particle emission from tantalum plasma produced by 532 nm laser pulse ablation. *Journal of Applied Physics* **100**, 093306 (2006).

114. Torrisi, L., Cavallaro, S., Giuffrida, L., Gammino, S. & Andò, L. Ti post-ion acceleration from a laser ion source. *Radiation Effects and Defects in Solids* **165**, 509 (2010).

115. Thum-Jager, A. & Rohr, K. Angular emission distributions of neutrals and ions in laser ablated particle beams. *Journal of Physics D: Applied Physics* **32**, 2827 (1999).

116. Thum, A., Rupp, A. & Rohr, K. Two-component structure in the angular emission of a laser-produced Ta plasma. *Journal of Physics D: Applied Physics* **27**, 1791 (1994).

117. Qaisar, M. S. & Pert, G. J. Laser ablation of Mg, Cu, and Pb using infrared and ultraviolet low-fluence lasers. *Journal of Applied Physics* **94**, 1468 (2003).

118. Amoruso, S., Armenante, M., Berardi, V., Bruzzese, R., Velotta, R. & Wang, X. High fluence visible and ultraviolet laser ablation of metallic targets. *Applied Surface Science* **127-129**, 1017 (1998).

119. Amoruso, S., Armenante, M., Berardi, V., Bruzzese, R. & Spinelli, N. Absorption and saturation mechanisms in aluminium laser ablated plasmas. *Applied Physics A: Materials Science & Processing* **65**, 265 (1997).

120. Tyrrell, G. C., Coccia, L. G., York, T. H. & Boyd, I. W. Energy-dispersive mass spectrometry of high energy ions generated during KrF excimer and frequency-doubled Nd:YAG laser ablation of metals. *Applied Surface Science* **96-98**, 227 (1996).

121. Tanaka, H., Matsumoto, A., Akinaga, K., Takahashi, A. & Okada, T. Comparative study on emission characteristics of extreme ultraviolet radiation from CO_2 and Nd:YAG laser-produced tin plasmas. *Applied Physics Letters* **87**, 041503 (2005).

122. Torrisi, L., Gammino, S., Andò, L., Nassisi, V., Doria, D. & Pedone, A. Comparison of nanosecond laser ablation at 1064 and 308 nm wavelength. *Applied Surface Science* **210**, 262 (2003).

123. Harilal, S. S., Bindhu, C. V., Tillack, M. S., Najmabadi, F. & Gaeris, A. C. Internal structure and expansion dynamics of laser ablation plumes into ambient gases. *Journal of Applied Physics* **93**, 2380 (2003).

124. Bulgakova, N. M. & Bulgakov, A. V. Gas-dynamic effects of the interaction between a pulsed laser-ablation plume and the ambient gas : analogy with an underexpanded jet. *Journal of physics D: Applied physics* **31**, 693 (1998).

125. Bogaerts, A., Chen, Z. & Bleiner, D. Laser ablation of copper in different background gases: comparative study by numerical modeling and experiments. *Journal of Analytical Atomic Spectrometry* **21**, 384 (2006).

126. Bogaerts, A. & Chen, Z. Nanosecond laser ablation of Cu: modeling of the expansion in He background gas, and comparison with expansion in vacuum. *J. Anal. At. Spectrom.* **19**, 1169 (2004).

127. Bogaerts, A., Chen, Z., Gijbels, R. & Vertes, A. Laser ablation for analytical sampling: what can we learn from modeling? *Spectrochimica Acta Part B: Atomic Spectroscopy* **58**, 1867 (2003).

128. Gusarov, A., Gnedovets, A. & Smurov, I. Two-dimensional gas-dynamic model of laser ablation in an ambient gas. *Applied Surface Science* **154-155**, 66 (2000).

129. Gusarov, A. V., Gnedovets, A. G. & Smurov, I. Gas dynamics of laser ablation: Influence of ambient atmosphere. *Journal of Applied Physics* **88**, 4352 (2000).

130. Harilal, S. S. Influence of spot size on propagation dynamics of laser-produced tin plasma. *Journal of Applied Physics* **102**, 123306 (2007).

131. Huang, R., Yu, Q., Li, L., Lin, Y., Hang, W., He, J. & Huang, B. High irradiance laser ionization orthogonal time-of-flight mass spectrometry: A versatile tool for solid analysis. *Mass Spectrometry Reviews* **30**, 1256 (2011).

132. Anoop, K. K., Ni, X., Bianco, M., Paparo, D., Wang, X., Bruzzese, R. & Amoruso, S. Two-dimensional imaging of atomic and nanoparticle components in copper plasma plume produced by ultrafast laser ablation. *Applied Physics A* **117**, 313 (2014).

133. Donnelly, T., Lunney, J. G., Amoruso, S., Bruzzese, R., Wang, X. & Ni, X. Dynamics of the plumes produced by ultrafast laser ablation of metals. *Journal of Applied Physics* **108** (2010).

134. Elsied, A. M., Termini, N. C., Diwakar, P. K. & Hassanein, A. Characteristics of Ions Emission from Ultrashort Laser Produced Plasma. *Scientific Reports* **6**, 38256 (2016).

135. Albert, O., Roger, S., Glinec, Y., Loulergue, J. C., Etchepare, J., Boulmer-Leborgne, C., Perrière, J. & Millon, E. Time-resolved spectroscopy measurements of a titanium plasma induced by nanosecond and femtosecond lasers. *Applied Physics A: Materials Science and Processing* **76**, 319 (2003).

136. Mannion, P. T., Favre, S., Mullan, C., Ivanov, D. S., O'Connor, G. M., Glynn, T. J., Doggett, B. & Lunney, J. G. Langmuir probe investigation of plasma expansion in femto-and picosecond laser ablation of selected metals. *Journal of Physics: Conference Series* **59**, 753 (2007).

137. Millon, E., Perrière, J., Défourneau, R. M., Défourneau, D., Albert, O. & Etchepare, J. Femtosecond pulsed-laser deposition of BaTiO3. *Applied Physics A: Materials Science and Processing* **77**, 73 (2003).

138. Perrière, J., Millon, E., Seiler, W., Boulmer-Leborgne, C., Craciun, V., Albert, O., Loulergue, J. C. & Etchepare, J. Comparison between ZnO films grown by femtosecond and nanosecond laser ablation. *Journal of Applied Physics* **91**, 690 (2002).

139. Toftmann, B., Doggett, B., Budtz-Jørgensen, C., Schou, J. & Lunney, J. G. Femtosecond ultraviolet laser ablation of silver and comparison with nanosecond ablation. *Journal of Applied Physics* **113**, 083304 (2013).

140. Verhoff, B., Harilal, S. S. & Hassanein, A. Angular emission of ions and mass deposition from femtosecond and nanosecond laser-produced plasmas. *Journal of Applied Physics* **111**, 123304 (2012).

141. Tanner, S. D., Baranov, V. I. & Bandura, D. R. *Reaction cells and collision cells for ICP-MS: A tutorial review* 2002.

142. Cordero, B., Gómez, V., Platero-Prats, A. E., Revés, M., Echeverría, J., Cremades, E., Barragán, F. & Alvarez, S. Covalent radii revisited. *Journal of the Chemical Society. Dalton Transactions* **0**, 2832 (2008).

143. Shaffer, S. a., Tang, K. Q., Anderson, G. a., Prior, D. C., Udseth, H. R. & Smith, R. D. A novel ion funnel for focusing ions at elevated pressure using electrospray ionization mass spectrometry. *Rapid Communications in Mass Spectrometry* **11**, 1813 (1997).

144. Gerlich, D. Inhomogeneous RF-Fields—A Versatile Tool for the Study of Processes with Slow Ions. *Advances in Chemical Physics, Volume 82* **1**, 1 (1992).

145. Kelly, R. T., Tolmachev, A. V., Page, J. S., Tang, K. & Smith, R. D. The ion funnel: Theory, implementations, and applications. *Mass Spectrometry Reviews* **29**, 294 (2010).

146. Shaffer, S. A., Prior, D. C., Anderson, G. A., Udseth, H. R. & Smith, R. D. An ion funnel interface for improved ion focusing and sensitivity using electrospray ionization mass spectrometry. *Analytical chemistry* **70**, 4111 (1998).

147. Tolmachev, A. V., Kim, T., Udseth, H. R., Smith, R. D., Bailey, T. H. & Futrell, J. H. Simulation-based optimization of the electrodynamic ion funnel for high sensitivity electrospray ionization mass spectrometry. *International Journal of Mass Spectrometry* **203**, 31 (2000).

148. Tolmachev, a. V., Chernushevich, I. V., Dodonov, a. F. & Standing, K. G. A collisional focusing ion guide for coupling an atmospheric pressure ion source to a mass spectrometer. *Nuclear Instruments and Methods in Physics Research Section B: Beam Interactions with Materials and Atoms* **124**, 112 (1997).

149. Tang, K., Shvartsburg, A. a., Lee, H.-N., Prior, D. C., Buschbach, M. a., Li, F., Tolmachev, A. V., Anderson, G. a. & Smith, R. D. High-sensitivity ion mobility spectrometry/mass spectrometry using electrodynamic ion funnel interfaces. *Analytical chemistry* **77**, 3330 (2005).

150. Xu, H., Zhang, X., Wang, Y., Ling, X. & Tian, D. Design and performance evaluation of a novel ion funnel driven by a phase-modulated rectangular wave. *Rapid communications in mass spectrometry : RCM* **30**, 1079 (2016).

151. Varentsov, V. *A New Approach to the Extraction System Design* (SHIP-TRAP Collaboration Meeting, LMU, Muenchen, 2001).

152. Pritchard, P. J. *Fox and McDonald's Introduction to Fluid Mechanics* 8th (John Wiley and Sons, New York, Chichester, 2011).

153. Briukhanov, A. S., Boriskin, A. I., Bykovskii, Y. A., Eriomenko, V. M. & Yariomenko, V. M. EMAL-2 laser ion source mass spectrograph and its analytical capabilities. *International Journal of Mass Spectrometry and Ion Physics* **47**, 35 (1983).

154. Wolff, M. M. & Stephens, W. E. A Pulsed Mass Spectrometer with Time Dispersion. *Review of Scientific Instruments* **24**, 616 (1953).

155. Dawson, J. H. J. & Guilhaus, M. Orthogonal-acceleration time-of-flight mass spectrometer. *Rapid Communications in Mass Spectrometry* **3**, 155 (1989).

156. Wiley, W. C. & McLaren, I. H. Time-of-flight mass spectrometer with improved resolution. *Review of Scientific Instruments* **26**, 1150 (1955).

157. Mamyrin, B. A., Karataev, V. I., Shmikk, D. V. & Zagulin, V. A. The mass-reflectron, a new nonmagnetic time-of-flight mass spectrometer with high resolution. *Sov Phys JETP* **37**, 45 (1973).

158. Boesl, U. Time-of-flight mass spectrometry: Introduction to the basics. *Mass Spectrometry Reviews* **36**, 86 (2017).

159. Cotter, R. J. Peer Reviewed: The New Time-of-Flight Mass Spectrometry. *Analytical Chemistry* **71**, 445A (2008).

160. Dennis, E. A., Gundlach-Graham, A. W., Enke, C. G., Ray, S. J., Carado, A. J., Barinaga, C. J., Koppenaal, D. W. & Hieftje, G. M. How constant momentum acceleration decouples energy and space focusing in distance-of-flight and time-of-flight mass spectrometries. *Journal of the American Society for Mass Spectrometry* **24**, 690 (2013).

161. Guilhaus, M., Selby, D. & Mlynski, V. Orthogonal acceleration time-of-flight mass spectrometry. *Mass Spectrometry Reviews* **19**, 65 (2000).

162. Gundlach-Graham, A., Hendriks, L., Mehrabi, K. & Günther, D. Monte Carlo Simulation of Low-Count Signals in Time-of-Flight Mass Spectrometry and Its Application to Single-Particle Detection. *Analytical Chemistry* **90**, 11847 (2018).

163. Tanner, M. & Günther, D. A new ICP–TOFMS. Measurement and readout of mass spectra with 30 μs time resolution, applied to in-torch LA–ICP–MS. *Analytical and Bioanalytical Chemistry* **391**, 1211 (2008).

164. Tarik, M., Lotito, G., Whitby, J. A., Koch, J., Fuhrer, K., Gonin, M., Michler, J., Bolli, J.-L. & Günther, D. Development and fundamental investigation of Laser Ablation Glow Discharge Time-Of-Flight Mass Spectrometry (LA-GD-TOFMS). *Spectrochimica Acta Part B: Atomic Spectroscopy* **64**, 262 (2009).

165. Günther, D., Hattendorf, B., Dietiker, R., Egorova, T. & Varentsov, V. *Laser-ablation ion source with ion funnel* 2010.

166. Becker, J. S. & Dietze, H. J. Laser ionization mass spectrometry in inorganic trace analysis. *Fresenius' Journal of Analytical Chemistry* **344**, 69 (1992).

167. Moreno-García, P., Grimaudo, V., Riedo, A., Tulej, M., Wurz, P. & Broekmann, P. Towards matrix-free femtosecond-laser desorption mass spectrometry for in situ space research. *Rapid Communications in Mass Spectrometry* **30**, 1031 (2016).

168. Kuhn, H.-R. & Günther, D. Elemental Fractionation Studies in Laser Ablation Inductively Coupled Plasma Mass Spectrometry on Laser-Induced Brass Aerosols. *Analytical Chemistry* **75**, 747 (2003).

169. Koch, J., von Bohlen, A., Hergenröder, R. & Niemax, K. Particle size distributions and compositions of aerosols produced by near-IR femto- and nanosecond laser ablation of brass. *J. Anal. At. Spectrom.* **19**, 267 (2004).

170. Wälle, M., Koch, J. & Günther, D. Analysis of brass and silicate glass by femtosecond laser ablation inductively coupled plasma mass spectrometry using liquid standard calibration. *Journal of Analytical Atomic Spectrometry* **23**, 1285 (2008).

171. Nečas, D. & Klapetek, P. Gwyddion: an open-source software for SPM data analysis. *Open Physics* **10** (2012).

172. Burger, M., Schwarz, G., Gundlach-Graham, A., Käser, D., Hattendorf, B. & Günther, D. Capabilities of laser ablation inductively coupled plasma time-of-flight mass spectrometry. *Journal of Analytical Atomic Spectrometry* **32**, 1946 (2017).

173. Longerich, H. P., Jackson, S. E. & Günther, D. Inter-laboratory note. Laser ablation inductively coupled plasma mass spectrometric transient signal data acquisition and analyte concentration calculation. *J. Anal. At. Spectrom.* **11**, 899 (1996).

174. Weast, R. C. & Astle, M. J. *CRC Handbook of chemistry and physics: a ready-reference book of chemical and physical data.* (ed CRC-press) 2454 (1981).

175. Moreno-García, P., Grimaudo, V., Riedo, A., Cedeño López, A., Wiesendanger, R., Tulej, M., Gruber, C., Lörtscher, E., Wurz, P. & Broekmann, P. Insights into Laser Ablation Processes of Heterogeneous Samples: Toward Analysis of Through-Silicon-Vias. *Analytical Chemistry* **90**, 6666 (2018).

176. Käser, D., Hendriks, L., Koch, J. & Günther, D. Depth profile analyses with sub 100-nm depth resolution of a metal thin film by femtosecond - laser ablation - inductively coupled plasma - time-of-flight mass spectrometry. *Spectrochimica Acta Part B: Atomic Spectroscopy* **149**, 176 (2018).

177. Jochum, K. P., Nohl, U., Herwig, K., Lammel, E., Stoll, B. & Hofmann, A. W. GeoReM: A New Geochemical Database for Reference Materials and Isotopic Standards. *Geostandards and Geoanalytical Research* **29**, 333 (2005).

178. Eggins, S. M., Kinsley, L. P. & Shelley, J. M. Deposition and element fractionation processes during atmospheric pressure laser sampling for analysis by ICP-MS. *Applied Surface Science* **127-129**, 278 (1998).

179. Lotito, G. *Coupling of laser ablation and a pulsed glow discharge time-of-flight mass spectrometer for the analysis of inorganic and organic samples* PhD thesis (ETH Zürich, 2012).

180. Kalinitchenko, I. *Ion optical system for a mass spectrometer* 2003.

181. Dahl, D. A. SIMION for the personal computer in reflection. *International Journal of Mass Spectrometry* **200**, 3 (2000).

Querci Lorenzo

Curriculum Vitae

Nationality	*Italian, Swiss*
Date of birth	*27. November 1989*
Place of birth	*Firenze, Italy*

Education

2016–2019	**ETH Zürich**, *PhD Student,* defense on 21/08/2019. Switzerland
2013–2015	**ETH Zürich**, *Master of Science ETH in Chemistry.* Switzerland
2009–2013	**ETH Zürich**, *Bachelor of Science ETH in Chemistry.* Switzerland

Working experiences

2015	**Swiss national museum**, *Civil service in the Conservation Research Laboratory of the Swiss National Museum* , Affoltern am Albis . Switzerland

Languages

Italian	**Mother tongue**
English	**Full professional proficiency**
German	**Full professional proficiency (Goethe-Zertifikat C1, 2009)**
French	**Basic conversation skills**

Articles in peer-reviewed journals:

1. Paunescu, D., Mora, C. A., Querci, L., Heckel, R., Puddu, M., Hattendorf, B., Günther, D. & Grass, R. N. Detecting and Number Counting of Single Engineered Nanoparticles by Digital Particle Polymerase Chain Reaction. *ACS nano* **9**, 9564 (2015).

2. Querci, L., Varentsov, V., Günther, D. & Hattendorf, B. An Rf-only ion funnel interface for ion cooling in laser ablation time of flight mass spectrometry. *Spectrochimica Acta Part B: Atomic Spectroscopy* **146**, 57 (2018).

3. Lima, M. G., Vogler, D., Querci, L., Madonna, C., Hattendorf, B., Saar, M. O. & Kong, X.-Z. Thermally driven fracture aperture variation in naturally fractured granites. *Geothermal Energy* **7**, 23 (2019).

4. Ma, J., Querci, L., Hattendorf, B., Saar, M. O. & Kong, X.-Z. Toward a Spatiotemporal Understanding of Dolomite Dissolution in Sandstone by CO2-Enriched Brine Circulation. *Environmental Science & Technology* **53**. PMID: 31588741, 12458 (2019).

Conference contributions:

5. Hattendorf, B., Querci, L., Varentsov, V. & Günther, D. *Taming Laser Generated Ions for Their Use in Mass Spectrometry* in *European Winter Conference on Plasma Spectrochemistry (EWCPS), Sankt Anton AT* (2017).

6. Querci, L., Hattendorf, B., Varentsov, V. & Günther, D. *Laser Ablation Time of Flight Mass Spectrometry using an Ion Funnel for Trace Element Analysis in Solids* in *Swiss chemical society fall meeting, Bern CH* (2017).

7. Hattendorf, B., Querci, L. & Günther, D. *Laser ablation under pressure for mass spectrometry-based element imaging without an ICP* in *CH analysis, Beatenberg CH* (2018).

8. Querci, L., Becker, P., Käser, D., Koch, J., Hattendorf, B. & Günther, D. *Element analysis with thermalized laser ablation ions from solid samples* in *International Mass Spectrometry Conference IMSC , Florence IT* (2018).

9. Querci, L., Eggel, E., Varentsov, V., Günther, D. & Hattendorf, B. *Investigation of the kinetic energy distribution generated with a laser ablation-ion funnel (lafu) source* in *European Winter Conference on Plasma Spectrochemistry (EWCPS), Sankt Anton AT* (2017).

10. Querci, L. & Hattendorf, B. *Investigation of ion transmission in laser ablation time of flight mass spectrometry using ion funnel* in *Swiss chemical society fall meeting, Zurich CH* (2016).

11. Querci, L., Hattendorf, B., Varentsov, V. & Günther, D. *Laser ablation time of flight mass spectrometry using ion funnel for trace element analysis in solids* in *CH analysis, Beatenberg CH* (2016).